

2006

# Using X-ray computed tomography to measure local gas holdup in a stirred tank reactor

Jason J. Ford  
Iowa State University

Follow this and additional works at: <https://lib.dr.iastate.edu/rtd>

 Part of the [Chemical Engineering Commons](#), and the [Mechanical Engineering Commons](#)

## Recommended Citation

Ford, Jason J., "Using X-ray computed tomography to measure local gas holdup in a stirred tank reactor " (2006). *Retrospective Theses and Dissertations*. 1378.  
<https://lib.dr.iastate.edu/rtd/1378>

This Thesis is brought to you for free and open access by the Iowa State University Capstones, Theses and Dissertations at Iowa State University Digital Repository. It has been accepted for inclusion in Retrospective Theses and Dissertations by an authorized administrator of Iowa State University Digital Repository. For more information, please contact [digirep@iastate.edu](mailto:digirep@iastate.edu).

**Using X-ray computed tomography  
to measure local gas holdup in a stirred tank reactor**

by

**Jason J. Ford**

A thesis submitted to the graduate faculty  
in partial fulfillment of the requirements for the degree of  
**MASTER OF SCIENCE**

Major: Mechanical Engineering

Program of Study Committee:  
Theodore John Heindel, Major Professor  
Francine Battaglia  
Alan A. Dispirito

Iowa State University

Ames, Iowa

2006

© Copyright by Jason J. Ford, 2006. All rights reserved.

UMI Number: 1439841



---

UMI Microform 1439841

Copyright 2007 by ProQuest Information and Learning Company.  
All rights reserved. This microform edition is protected against  
unauthorized copying under Title 17, United States Code.

---

ProQuest Information and Learning Company  
300 North Zeeb Road  
P.O. Box 1346  
Ann Arbor, MI 48106-1346

## TABLE OF CONTENTS

LIST OF TABLES .....	iv
LIST OF FIGURES .....	v
LIST OF NOMENCLATURE .....	viii
ACKNOWLEDGEMENTS .....	xi
ABSTRACT .....	xii
CHAPTER 1: INTRODUCTION .....	1
1.1 Motivation .....	1
1.2 Goals .....	2
CHAPTER 2: LITERATURE REVIEW .....	3
2.1 Stirred Tank Reactor Basics .....	3
2.1.1 Geometry, Components, and Assumptions .....	3
2.1.2 Dimensionless Numbers .....	5
2.2 Hydrodynamics .....	6
2.2.1 Flow Around Impeller .....	7
2.2.2 Constant $Q_g$ .....	9
2.2.3 Constant $N$ .....	10
2.3 Invasive Measurements .....	12
2.3.1 Heat Transfer Probe .....	12
2.3.2 Needle Probe .....	13
2.3.3 Suction Method .....	15
2.4 Noninvasive Measurements .....	16
2.4.1 Non-Tomographic Techniques .....	16
2.4.1.1 Visually .....	16
2.4.1.2 Pressure Drop .....	17
2.4.2 Non-Nuclear Based Tomographic Techniques .....	18
2.4.2.1 Ultrasound .....	18
2.4.2.2 Electrical Tomography Techniques .....	18
2.4.3 Nuclear Based Tomography .....	20
2.4.3.1 $\gamma$ -Ray .....	20

2.4.3.2 X-ray .....	21
2.5 Literature Review Summary .....	22
CHAPTER 3: EQUIPMENT AND EXPERIMENTAL METHODS .....	29
3.1 Stirred Tank Reactor Description .....	29
3.2 Power Measurements .....	30
3.3 X-Ray System Description .....	32
3.4 X-ray Data Acquisition and Reduction .....	33
3.4.1 CT Scan Procedure .....	34
3.4.2 Pixel Normalization Correction .....	36
3.4.3 Beam Hardening Correction .....	37
3.4.4 Determining Local Gas Holdup .....	39
3.4.4.1 Gas Holdup Equation .....	39
3.4.4.2 Determination of Gray Scale Values .....	41
CHAPTER 4: RESULTS AND DISCUSSION .....	48
4.1 Power Measurement .....	48
4.1.1 Constant Gas Flow Rate .....	49
4.1.2 Constant Impeller Speed .....	51
4.2 Gas Holdup Measurements .....	52
4.2.1 Qualitative Gas Holdup Results .....	53
4.2.1.1 z-Slice .....	53
4.2.1.2 x- and y-Slice .....	56
4.2.2 Quantitative Gas Holdup Results .....	58
4.2.3 Error Quantification .....	61
CHAPTER 5: CONCLUSIONS AND RECOMMENDATIONS .....	87
5.1 Conclusions .....	87
5.2 Recommendations for Further Study .....	88
5.2.1 Software Improvements .....	88
5.2.2 Future Work .....	89
REFERENCES .....	90

**LIST OF TABLES**

Table 4.1: Conditions for CT scans. .... 86

Table 4.2: Table for overall gas holdup of imaging region (CT) and tank (Global). .... 86

## LIST OF FIGURES

Figure 2.1:	Stirred tank reactor standard geometry (Adopted from Tatterson, 1991). .....	23
Figure 2.2:	Standard six blade Rushton turbine used by Ungerman (2006). .....	24
Figure 2.3:	Progression of cavities with increasing $Q_g$ and constant $N$ (Smith and Warmoeskerken, 1985). .....	24
Figure 2.4:	Cavity structure with increasing $Q_g$ at constant $N$ (Smith and Warmoeskerken, 1985; Nienow et al., 1985). .....	25
Figure 2.5:	Radial flow pattern of a Rushton impeller (Barona, 1979). .....	25
Figure 2.6:	Bulk flow patterns at constant gas flow rate $Q_g$ while increasing impeller speed $N$ from left to right (Nienow et al. 1977). .....	26
Figure 2.7:	Generic plot of gassed power number as a function of flow number with $Q_g = \text{constant}$ (Kapic, 2005). .....	26
Figure 2.8:	The three gas loading transitions for a Rushton turbine; (a) flooding, (b) loading, (c) and completely dispersed (Nienow et al., 1985). .....	27
Figure 2.9:	Gassed power ratio at constant $N$ (Nienow et al., 1985). .....	27
Figure 2.10:	Cavity formation of a gassed power curve (Kapic, 2005). .....	28
Figure 2.11:	General flow map for a STR with $T = 1.2\text{m}$ and $D = 0.48\text{ m}$ (Smith and Warmoeskerken, 1985). .....	28
Figure 3.1:	Stirred tank reactor used in this study .....	43
Figure 3.2:	Impeller. ....	44
Figure 3.3:	Power measurement setup.....	44

Figure 3.4:	X-ray system setup.....	45
Figure 3.5:	X-ray image of empty STR.....	45
Figure 3.6:	Plot of $\ln(I_0/I)$ vs. $L$ .....	46
Figure 3.7:	Plot of difference vs. $\ln(I_0/I)$ .....	46
Figure 3.8:	Plot showing line with and without beam hardening correction.....	47
Figure 4.1:	Mechanical power as a function of impeller speed.....	62
Figure 4.2:	Ungassed power number vs. Reynolds number.....	63
Figure 4.3:	Gassed power number vs. flow number at constant $Q_g$ .....	64
Figure 4.4:	Flooding/loading progression for $Q_g = 9$ LPM; (a) $N = 0$ , $Q_g = 0$ , (b) $N = 200$ rpm, (c) $N = 225$ rpm, and (d) $N = 250$ rpm.....	65
Figure 4.5:	Loading/complete dispersion progression for $Q_g = 3$ LPM; (a) $N = 275$ rpm, (b) $N = 300$ rpm, and (c) $N = 325$ rpm.....	66
Figure 4.6:	Bubble size decreasing at constant $Q_g = 7$ LPM; (a) $N = 400$ rpm, (b) $N = 600$ rpm, and (c) $N = 800$ rpm.....	67
Figure 4.7:	Gassed to ungassed power vs. $Q_g$ at constant $N$ .....	68
Figure 4.8:	Gassed to ungassed power vs. flow number at constant $N$ .....	69
Figure 4.9:	Gassed power number vs. flow number at constant $Q_g$ with CT scan conditions labeled.....	70
Figure 4.10:	STR bottom and ring sparger.....	71
Figure 4.11:	A sample z-slice with gas holdup mapping diagram ( $z = 0.8$ cm).....	72
Figure 4.12:	Slices taken at 3 different heights for $Q_g = 6$ LPM.....	73
Figure 4.13:	Slices taken at 3 different heights for various impeller speeds with $Q_g$ $= 9$ LPM.....	74

Figure 4.14:	Slices taken at 3 different heights for $Q_g = 12$ LPM.....	75
Figure 4.15:	CT x-slices for (a) loaded ( $N = 350$ rpm) and (b) completely dispersed ( $N = 700$ rpm) for $Q_g = 6$ LPM.....	76
Figure 4.16:	Flooded at $Q_g = 9$ LPM and $N = 200$ rpm for (a) x- and (b) y-slice.....	77
Figure 4.17:	CT x-slices for (a) loaded ( $N = 350$ rpm) and (b) completely dispersed ( $N = 700$ rpm) for $Q_g = 9$ LPM.....	78
Figure 4.18:	Completely dispersed at $Q_g = 9$ LPM and $N = 700$ rpm for (a) x- and (b) y-slice. ....	79
Figure 4.19:	CT x-slices for (a) loaded ( $N = 325$ rpm) and (b) completely dispersed ( $N = 700$ rpm) for $Q_g = 12$ LPM.....	80
Figure 4.20:	Local gas holdup values along x-slice at height $z = 0.8$ cm for $Q_g = 9$ LPM. ....	81
Figure 4.21:	Local gas holdup values along x-slice at height $z = 3.0$ cm for $Q_g = 9$ LPM. ....	82
Figure 4.22:	Local gas holdup values along x-slice at height $z = 5.3$ cm for $Q_g = 9$ LPM. ....	83
Figure 4.23:	Average slice holdup for $Q_g = 9$ LPM.....	84
Figure 4.24:	Average slice holdup for $N = 700$ rpm. ....	85

## LIST OF NOMENCLATURE

B	Baffle width	(m)
C	Impeller clearance	(m)
D	Impeller diameter	(m)
$Fl_g$	Gas flow number	(-)
Fr	Froude number	(-)
g	Acceleration due to gravity	(m s <sup>-2</sup> )
GS	Gray scale CT value of mixture	(-)
$GS_g$	Gray scale CT value for air	(-)
$GS_l$	Gray scale CT value for water	(-)
h	Distance between manometers	(m)
H	Height of liquid with no gas	(m)
$H_D$	Height of liquid with dispersion	(m)
I	X-ray intensity	(-)
$I_0$	Initial X-ray intensity	(-)
L	Thickness of material X-ray passes through	(cm)
N	Impeller speed	(rpm)
$N_{cd}$	Impeller speed at complete dispersion	(rpm)
$N_f$	Impeller speed at flooding	(rpm)
$N_{pg}$	Gassed power number	(-)
$N_{po}$	Ungassed power number	(-)
$N_r$	Impeller speed at recirculation	(rpm)

p	Pressure	(N m <sup>-2</sup> )
P <sub>e</sub>	Measured power in empty tank	(W)
P <sub>g</sub>	Gassed power	(W)
P <sub>l</sub>	Measured mechanical power	(W)
P <sub>mech</sub>	Mechanical power	(W)
P <sub>o</sub>	Ungassed power	(W)
Q <sub>g</sub>	Gas flow rate	(LPM)
Re	Reynolds number	(-)
T	Tank diameter	(m)
V <sub>g</sub>	Volume gas fraction	(m <sup>3</sup> )
V <sub>L</sub>	Volume liquid fraction	(m <sup>3</sup> )
V <sub>T</sub>	Total volume	(m <sup>3</sup> )
W	Impeller blade width	(m)
z	Height from bottom of impeller	(cm)

#### Abbreviations

CFD	Computational fluid dynamics
CT	Computed tomography
CTA	Constant temperature anemometry
ECT	Electrical capacitance tomography
ERT	Electrical resistance tomography
ISU	Iowa State University
STR	Stirred tank reactor

Greek Symbols

$\varepsilon_g$	Gas holdup	(-)
$\rho_{\text{eff}}$	Mixture density	(kg m <sup>-3</sup> )
$\rho_g$	Gas density	(kg m <sup>-3</sup> )
$\rho_L$	Fluid density	(kg m <sup>-3</sup> )
$\mu$	Linear attenuation coefficient of mixture	(cm <sup>-1</sup> )
$\mu_f$	Fluid dynamic viscosity	(Ns m <sup>-2</sup> )
$\tau$	Impeller torque	(N m)

## **ACKNOWLEDGEMENTS**

First, I would like to thank Dr. Heindel for providing me with the opportunity to work in his lab. His guidance and instruction has helped me realize and reach my potential.

Second, I would like to thank Dr. Terry Jensen for all the times he stopped by before or after lunch. His willingness to help with installing the new detector and answering all my questions is greatly appreciated.

Thanks are also expressed for Dr. Dispirito and Dr. Battaglia for taking the time to serve on my committee.

I would also like to thank my family and friends for their love, support, and encouragement. My parents have always been supportive of me in everything that I have done. Thanks to Josie for being understanding and interested in my research.

Lastly, but most importantly, I want to give credit to the Lord who has blessed me with the abilities to get me through graduate school.

## ABSTRACT

Gas holdup is one of the most important hydrodynamic parameters needed for reliable design, performance estimation, and scale-up of stirred tank reactors (STRs). In the present work, local gas holdup is measured in an acrylic stirred tank reactor equipped with a Rushton impeller using X-ray computed tomography (CT) for many different operating conditions. Power consumption for different operating conditions is determined to identify various STR flow regimes. The gas holdup results obtained by X-ray CT imaging are presented as: (i) profiles along all 3 axes, (ii) plots of local gas holdup along the x-axis, (iii) average gas holdup for z-slice, and (iv) overall gas holdup for the imaging region. The high resolution of the X-ray CT system allows for the visualization of minor details such as recirculation zones behind the baffles. The results show that there are dramatic differences in gas dispersion depending on the flow regime. Completely dispersed conditions have a relatively constant holdup profile while flooded conditions have a parabolic shape with an increase in gas holdup towards the center of the tank. The CT slices show that there is very little visual difference between scans taken in the same operating regime, even though there are differences in impeller speed and gas flow rate. Average z-slice holdup values increase with increasing height from the impeller for the flooded condition, while the opposite occurs for the loaded and completely dispersed conditions. Local gas holdup conditions are sensitive to tank design, which are shown by differences in the x- and y-slices. Overall holdup values for the image region are determined and shown to increase as the impeller speed increases while holding  $Q_g$  constant.

## CHAPTER 1: INTRODUCTION

### 1.1 Motivation

In the chemical and processing industries, stirred tank reactors (STRs) are often used to carry out reactions between liquids and gases. Gas holdup, which is defined as the volumetric gas fraction (also called void fraction), is one of the most important hydrodynamic parameters needed for reliable design, performance estimation, and scale-up of these reactors. Gas holdup depends on the gas and liquid properties, superficial velocity, presence of solids, sparger design, reactor internals, and power consumption. In order to better design STRs, it is highly desirable for engineers to know the local gas holdup and how it changes with different operating conditions. The knowledge of local gas holdup can also be used for validating computational fluid dynamic (CFD) codes and for advancing the understanding of mixing fundamentals.

The measurement of local gas holdup in STRs has not been reported by many authors, while overall average gas holdup has been reported by many. Measuring local gas holdup is extremely difficult because invasive probes are just that, invasive, and they only provide a point source measurement. Tomographic measurement methods provide an alternative approach to measuring local gas holdup. They have the advantage of being nonintrusive, and they can provide a wide measurement area during a single measurement process.

To date, no local gas holdup measurements in a stirred tank reactor are available in the open literature using X-ray computed tomography. These data are the focus of this thesis.

## 1.2 Goals

The following work will focus on measuring local gas holdup in a stirred tank reactor under different operating conditions using X-ray computed tomography. This will be accomplished through the following goals:

1. Review previous methods for measuring gas holdup.
2. Measure power consumption by the STR under different operating conditions to identify various flow regimes.
3. Qualitatively analyze local gas holdup in the STR.
4. Quantitatively analyze local and global gas holdup.

The rest of this thesis will expand upon the above ideas. Chapter 2 will review STR hydrodynamics and both invasive and noninvasive techniques for measuring gas holdup. Chapter 3 will summarize the equipment and experimental methods for measuring power consumption and local gas holdup. Chapter 4 will present and discuss the results from power consumption and local gas holdup measurements. Finally, chapter 5 will provide a short summary of the conclusions of this study and outline recommendations for further study.

## CHAPTER 2: LITERATURE REVIEW

This chapter is divided into 5 sections. The first section outlines the basic components of a stirred tank reactor and common STR dimensionless numbers. The second section describes the hydrodynamics of a stirred tank reactor. The third section reviews invasive techniques previously used to measure gas holdup. The fourth section describes noninvasive techniques that are used to determine gas holdup. The last section provides a summary of the literature review.

### 2.1 Stirred Tank Reactor Basics

This section is separated into two subsections. The first section describes the geometry and components of a stirred tank reactor along with some common assumptions. The second section provides definitions for dimensionless numbers commonly used in modeling and correlating data for stirred tank reactors.

#### 2.1.1 Geometry, Components, and Assumptions

Stirred tank reactors come in many different sizes with various geometric characteristics, but between the late 1940s and early 1960s, a standard geometry shown in Fig. 2.1 (Figures are found at the end of the respective chapter.) was established for single-phase mixing (Tatterson, 1991). The standard geometric configuration evolved from power studies and is not the optimum geometry for all processes. All dimensions are scaled to the tank diameter ( $T$ ). The main components of the tank include the impeller, baffles, and sparger, each of which are described in the following paragraphs.

**Impeller**

An impeller is used to bring fluid motion to the entire tank and breakup bubbles (if gas is also injected into the tank). The standard impeller used in STRs is a Rushton turbine (Fig. 2.2) named in recognition of JH Rushton and his co-workers who did a lot of research on mixing and agitators in the 1950s (Nienow, 1998). The disk located in the middle of the impeller forces air into the high shear region of the blades. Recently, there have been more impellers designed that alter performance; these include radial flow impeller variations and many types of downward or upward pumping axial flow impellers. Some STRs utilize two or more impellers with different combinations depending on the desired flow pattern and operating conditions. Additional impellers are discussed in detail by Ungerman (2006).

**Baffles**

Four vertical wall baffles are typically located in the STR and equally spaced with a width of  $0.1T$ . Wall baffles maximize power input to the fluid and cause the vortex to break up, which minimizes solid body rotation and promotes mixing (Tatterson, 1991). Barona (1979) stated that in a non-baffled tank, the energy transmitted to the liquid is 4 to 6 times less than that transmitted in a baffled tank using the same impeller and equal speeds.

**Sparger**

There are two main types of spargers (ring or point) used in STRs, both of which are positioned below the impeller. Warmoeskerken and Smith (1985) used a ring sparger and a point sparger in their studies. While varying the impeller to sparger clearance, the flooding to loading transition occurred at conditions within  $\pm 10\%$  with the different spargers. If the ring sparger diameter is greater than the impeller disc, then considerable differences are noted

(Nienow et al., 1985). From these studies, it can be concluded that as long as the sparger diameter is smaller than the disc, variations in sparger design have little effect.

### **STR Assumptions**

The STR is usually run at steady state and operated at conditions to ensure good mixing. Therefore, the following assumptions are made in modeling STRs: no spatial variations in concentration, temperature, or reaction rate throughout the tank (Fogler, 1999).

#### **2.1.2 Dimensionless Numbers**

##### **Froude Number**

The Froude number (Fr) represents the ratio between inertial and gravitational forces and is defined by:

$$Fr = \frac{ND^2}{g} \quad (2.1)$$

where N is the impeller speed, D is the impeller diameter, and g is the acceleration due to gravity.

##### **Gas Flow Number**

The gas flow number ( $Fl_g$ ) represents the ratio of the gas flow rate to the impeller pumping rate and is defined by:

$$Fl_g = \frac{Q_g}{ND^3} \quad (2.2)$$

where  $Q_g$  is the gas flow rate.

##### **Power Number**

There are two types of power numbers, gassed and ungassed. The power number represents the ratio of the pressure differences producing the flow to the inertial forces of the

dispersion. The power number is analogous to the friction factor for pipes or drag coefficient for particles (Nienow, 1998). The gassed power number is defined as:

$$N_{pg} = \frac{P_g}{\rho_L N^3 D^5} \quad (2.3)$$

where  $\rho_L$  is the density of the fluid and  $P_g$  is the impeller power input into the liquid with sparged gas. The ungassed power number is defined as:

$$N_{po} = \frac{P_o}{\rho_L N^3 D^5} \quad (2.4)$$

where  $P_o$  is the impeller power input into the liquid without gas being sparged into the tank.

### **Reynolds Number**

The Reynolds number (Re) represents the ratio of inertial to viscous forces and is defined by:

$$Re = \frac{\rho_L ND^2}{\mu_f} \quad (2.5)$$

where the density ( $\rho_L$ ) and dynamic viscosity ( $\mu_f$ ) are properties of the fluid. The Reynolds number is typically used to distinguish between laminar and turbulent flow.

## **2.2 Hydrodynamics**

This section is divided into three subsections. The first section describes the flow local to the impeller. The second section describes the hydrodynamics and power curves of a STR while holding the gas flow rate constant. The last section describes the hydrodynamics and power curves when the impeller speed is held constant while varying the gas flow rate.

### 2.2.1 Flow Around Impeller

The flow around the impeller has been studied intensively with and without aeration. In a stirred tank, the flow around the impeller controls power consumption, coalescence, and dispersion in gas-liquid mixtures to a large degree. Van't Reit and Smith (1975) showed that a pair of roll vortices develop behind the upper and lower edge of the blade in an ungasged system. The rotation of the roll vortices cause a relative under pressure along the axis. When the system is gassed, the under pressure along the axis draws more gas in towards the vortex core, which leads to the formation of ventilated cavities. The cavities have a streamlining action which lowers the drag coefficient causing the power demand of the impeller to drop. Van't Riet (1975) studied the cavity formation around impeller blades and defined three distinct types of cavities which form in low viscosity liquids and they depend on stirrer speed and gas flow rate: (1) vortex cavities, (2) clinging cavities, and (3) large cavities.

At low gas flow rates, the rotational structure is present with the dominant action being the roll vortices drawing in the gas. The large centrifugal force field associated with vortex cavities allows for highly efficient gas capture (Ranade and Deshpande, 1999). The vortex cavities (Fig. 2.3a) attract gas near the impeller, while dispersing gas from the downstream tip of the cavity. While holding the stirrer speed constant and increasing the gas flow rate, the cavity grows in diameter until it starts to interfere with the rotation of the liquid in the region between the impeller blade and cavity (Smith and Warmoeskerken, 1985). With the reduction in rotation, there is a distinct change in the cavity from a roll vortex to a clinging cavity (Fig 2.3b). Now, the cavity is attached to the horizontal edge of the blade. The flow is still directed outwards with dispersion occurring at the turbulent outer surface. With a further increase in gas flow rate, large cavities begin to develop (Fig 2.3c); they are

characterized by clear smooth surfaces from which the gas breaks away gently from the rear surfaces. When large cavities have formed, there is hardly any of the original vortex motion left. A major difference between large cavities and vortex and clinging cavities is that large cavities block part of the radial outflow from the impeller causing lower radial fluid velocities outside the impeller region when compared to the other two cavity shapes (Van't Riet, 1975).

The two phase flow around a six-blade Rushton impeller can be looked at as a collective whole. At low gas flow rates, 6 vortex cavities can be seen (Fig 2.4a). At higher gas flow rates and the same impeller speed, 6 clinging cavities form (Fig 2.4b). When the gas flow rate is further increased, a symmetric 3-3 structure forms where large cavities alternate with clinging cavities. At an even higher gas flow rate, 6 large cavities form but are of different size, while still maintaining the alternating pattern between big and small (Fig 2.4c). Smith and Warmoeskerken (1985) found that the 3-3 structures were stable with the cavities not changing blades during operation and the blade with the original large cavity was random. Up to the appearance of the 3-3 structures, the impeller region is not flooded (i.e.,  $N > N_f$ ), where flooding is defined by Warmoeskerken and Smith (1985) as the axial flush of gas through the impeller plane up to the free liquid surface. Further gas flow rate increases cause the impeller to become flooded and operate in the regime  $N < N_f$ . In this region, six ragged cavities (Fig 2.4d) form that oscillate violently and usually only cover the upper half of the blade (Nienow et al., 1985). The power draw ( $P_g/P_o$ ) increases due to the pressure at the front of the blade being greater than at the back. The ragged cavities appear like clinging cavities except for the fact that they are shortened, and the gas breaks away at the rear end rather than at the edge of the cavity.

### 2.2.2 Constant $Q_g$

The hydrodynamics of a STR are complicated and depend on many factors including the tank geometry, impeller speed, gas flow rate, and liquid viscosity. Gas enters the tank from the sparger located below the impeller. Through impeller induced shear and mixing, the bubbles are reduced in size and distributed throughout the tank. Increasing the impeller speed increases the gas-liquid interfacial area and mass transfer. The flow is considered laminar when  $Re \lesssim 10$  and turbulent when  $Re > 20,000$ , thereby giving a large transition region defined by  $10 < Re < 20,000$ . A Rushton impeller operating in the turbulent regime has a radial flow pattern as shown in Fig. 2.5.

A common way to describe the hydrodynamics of a STR is to hold the gas flow rate  $Q_g$  constant and vary the impeller speed  $N$ . Nienow et al. (1977) showed through visual observation that at a particular gas rate, the tank goes through different bulk mixing stages as the impeller speed is increased (Fig. 2.6). In Fig. 2.6, the impeller speed is increased from left to right while the gas flow rate is held constant. Nienow et al. (1977) summarized these bulk flow regimes as follows: (a) negligible dispersion, (b) enough dispersion to cause the upper part of the tank to behave as a bubble column, (c) gas circulation occurring mainly in the upper part of the tank, (d) gas circulation throughout tank, and (e) formation of secondary circulation loops.

When  $Q_g$  is constant,  $N_{pg}$  or  $P_g/P_o$  is usually plotted as a function of flow number  $Fl_g$ . The power curve generally follows the trend shown in Fig. 2.7, which is useful for determining the bulk flow regimes. The local minimum labeled  $N_{cd}$  corresponds to the impeller speed associated with complete gas dispersion. Once  $N_{cd}$  is reached, gas is distributed throughout the tank. The local maximum labeled  $N_r$  corresponds to the impeller

speed associated with gas recirculation. When the impeller speed is greater than or equal to  $N_r$ , the flow pattern in the tank looks like Fig. 2.6e. The other local maximum in Fig. 2.7 labeled  $N_f$ , corresponds to the impeller speed during the flooding/loading transition.

The bulk flows produced with Rushton impellers go through three well defined regimes as shown in Fig. 2.8 (Nienow et al., 1985). From  $N = 0$  to  $N = N_f$  (Fig 2.8a), the impeller is said to be flooded and dominated by a two-phase gas-liquid flow up the middle and a liquid flow down at the walls. The impeller stops pumping and the gas rises axially to the surface. Between  $N_f < N < N_{cd}$  (Fig 2.8b), the impeller is able to better distribute the gas horizontally. Still, there is poor distribution of the gas throughout the vessel due to the buoyancy forces of the gas being larger than the impeller radial force. For  $N > N_f$ , the impeller is said to be loaded. Much work has been done to predict the flooding/loading transition as it is crucial in the design of stirred tank reactors. When  $N > N_{cd}$ , gas is dispersed throughout the vessel. In the region  $N \gg N_{cd}$ , large amounts of gas recirculate and secondary loops are formed as shown in Fig. 2.8c.

### 2.2.3 Constant N

Another common way to describe the hydrodynamics of a STR is to hold the impeller speed constant while varying the gas flow rate. The hydrodynamics of a STR and the power drawn are closely related and can be seen when  $P_g/P_o$  is plotted as a function of flow number  $Fl_g$  at constant impeller speed. Figure 2.9 shows the general shape of this plot. When  $Fr < 0.045$ , the 3-3 structure does not form as the gas flow rate is increased (Nienow et al., 1985). The change in bulk flow from loaded to flooded (Fig. 2.8b to 2.8a) is accompanied by a change from clinging to ragged cavities and a step decrease in power consumption. When  $Fr > 0.045$ , the 3-3 structure is observed and the transition from Fig. 2.8b-a is accompanied with

a change from the 3-3 structure to six ragged cavities at the flooding-loading point and an increase in power consumption.

The shape of the power curve shown in Fig. 2.9 has two very distinct parts: (1) a convex part at low gas rates, and (2) a concave part at high gas rates (Warmoeskerken and Smith, 1982). The inflection point corresponds to the transition from 6 clinging cavities to the 3-3 structure of clinging and large cavities (Warmoeskerken et al., 1981). Before the inflection point, the gas power curve tends to drop quickly. After the inflection point, there is a gradual drop in the power curve and this corresponds to the fact that the transition from 3 to 6 large cavities occurs slowly. At even higher gas rates, the power curve becomes more gradual due to the stability from the cavities reaching maximum size. The different types of cavities have a direct effect on power consumption which is explained by Smith and Warmoeskerken (1985) and visually presented by Kacic (2005) in Fig. 2.10. The regions identified in Fig. 2.10 correspond to:

- a. A stable regime with six vortex cavities in which the power demand differs slightly from an ungassed system.
- b. A stable regime with six clinging cavities in which the power demand is at most 10% lower than an ungassed system.
- c. A stable regime with a 3-3 system of large and clinging cavities. The power demand is approximately 40% lower than an ungassed system.
- d. A stable regime with a 3-3 system of large cavities of alternating size. The power demand stays low in this regime.
- e. A stable regime in which the cavities grow resulting in a very low power demand.

- f. An unstable regime in which the impeller is flooded. Six vibrating cavities occur which cause an increase of about 25% in the power demand compared to the minimum value.

Smith and Warmoeskerken (1985) produced a flow regime map for a tank with  $T = 1.2$  m and  $D = 0.48$  m that showed the transitions from different flow regimes (Fig. 2.11). The following regimes were identified in the map: (1) vortex or cling cavities, (2) 3-3 structure of large cavities or large and clinging, and (3) ragged cavities. The transition from (1) to (2) corresponded to the inflection point in Fig. 2.9. The dashed line represented  $N_r$  which accompanied a peak in power demand. When flooding occurred and ragged cavities were formed, the power usually increased due to the fact that the ragged cavities had less of a streamlining effect. In summary, the cavity type formed is very important because it has a direct effect on the power demand and hydrodynamics of the STR.

## **2.3 Invasive Measurements**

Invasive measurements techniques are often used to measure gas holdup. Many invasive methods were developed in the early 1960s before noninvasive techniques were common. The problem with invasive techniques is that the flow is affected by the presence of the probes. This section describes many of the invasive techniques used to measure gas holdup in a stirred tank reactor, which include a heat transfer probe, a needle probe, and a suction method.

### **2.3.1 Heat Transfer Probe**

Hot film anemometry is a cheap technique that leads to local gas holdup and liquid average velocity. Heat exchange between an electrically heated probe and surrounding liquid

medium forms the basis for hot film anemometry. When bubbles pass by the probe, a noticeable drop in heat exchange is observed which causes a discontinuity in the probe electrical output (Boyer et al., 2002). From the signal, time-averaged gas holdup can be evaluated at the probe location. Lu and Ju (1987) used a conical hot-film probe CTA (constant temperature anemometry) to determine the local gas holdup and liquid velocity in a flat-bottomed cylindrical vessel of 28.8 cm internal diameter equipped with a disk-type turbine of diameter 9.6 cm. When the sparging rate was low, some of the bubbles could not be detected because they were too small to influence the response of the probe; which lead to an underestimation of the local gas holdup. The maximum error for local gas holdup measurement was  $\pm 10\%$  for holdup higher than 10% and  $\pm 20\%$  for holdup lower than 5%.

### **2.3.2 Needle Probe**

Needle probes are thin, sharp ended, and positioned to face the flow direction so that as many bubbles as possible are pierced by the probe. The two main types of needle probes are optical fiber probes and a group known as impedance probes.

Optical probes are made from quartz. Optical probes utilize the differences in the index of refraction between the two phases. Optical probes work on the principle that a light beam is transmitted through a liquid medium and reflected back when surrounded by gas. A phototransistor gives an analog signal output proportional to the received light intensity. Kumar et al. (1997) report that optical probes should mainly be used in transparent systems, with low void fractions, and at moderate temperatures. The probe would have a hard time detecting changes in voids if the bubble size was too small. Wang et al. (2006) used a fiber optic probe to measure the local gas holdup over a wide range of stirring speeds in a stirred

tank of  $T = 380$  mm equipped with a Rushton turbine. The results were consistent and in accordance with others in the literature.

Resistive, conductive, and capacitance probes are normally referred to as impedance probes. Resistivity probes detect the variation in resistance between two electrodes when bubbles pass through the gap. Bombac et al. (1997) used a microresistivity probe to measure the local gas holdup in a vessel of diameter 450 mm. The differences between integrated values of the local gas holdup and measured gas holdup by liquid level change were smaller than 9% for all conditions. Also, the reproducibility error was smaller than 4%.

Conductivity probes utilize the difference in gas and liquid conductivity and work well in aqueous gas-liquid systems (Kumar et al., 1997). An electrical conductivity probe has a stainless steel needle exposed at the end and a large electrode mounted on the wall. When the liquid is in contact with the tip, the electric circuit between the wall and tip is closed. Bubbles hitting the tip cause the circuit to be broken. Therefore the probe acts like a switch giving a binary signal. By summing the time duration of pulses for gas bubbles passed through the pointed end, the gas holdup at each position can be determined. Problems arise from the fact that some solutions are not very conductive, which can be overcome by adding salt. Also, the conductivity probe is sensitive to how it is positioned with respect to the flow. Takenaka and Takahashi (1996) used an electrical conductivity probe to measure local gas holdup in a stirred tank reactor. The probe had a fine pointed end made of a 100  $\mu\text{m}$  diameter platinum cylinder. The results obtained were close to the results obtained by other investigators. Greaves and Barigou (1988) used a conductivity probe to determine the difference in height between the gassed and ungassed state, which lead to a global gas holdup value.

Capacitance probes utilize differences in the dielectric constant of each phase (Kumar et al., 1997). Favre et al. (1993) used an invasive plate and frame capacitance probe to determine local gas holdup in a stirred tank reactor with two Rushton turbines. Two square stainless steel plates of length 5 cm with a distance of 2 cm between each plate were installed 5 cm above the top impeller. A voltage of 0.5 V was applied between the two plates. Their results show that the derived holdup value using the capacitance probe was smaller than the global value determined by liquid level change. Capacitance probes will not work very well in ionic liquids because the conductivity of the medium will interfere with the permittivity measurement. Some errors could also occur from the probe frequency response.

### **2.3.3 Suction Method**

The suction method is simple and provides measurement of the local gas holdup and equivalent bubble size. Nagase and Yasui (1983) used this technique to measure local gas holdup and described the technique in detail. The technique uses two electrodes, one to measure holdup and the other to measure bubble velocity. A vacuum pump is used to draw the local gas-liquid mixture into a tube. One error in this method is determining the correct suction velocity. Low suction velocity gave lower than expected gas holdup values, while high suction velocities gave a constant gas holdup. In all their experiments, the suction velocity was greater than 2.5 m/s. For their experiment, gas holdup measurements using the suction method and a needle-type electrode agreed with each other within an experimental error of 20%. Nienow et al. (1977) also used the suction method to determine the local gas holdup at 20 different locations in a stirred tank reactor. Nienow et al. (1977) report that although the sampling should be isokinetic, there are many difficulties in achieving this due to the complex flow of a stirred tank.

## 2.4 Noninvasive Measurements

This section is divided into 3 subsections and provides a review of the different techniques available to noninvasively measure gas holdup. The first section describes non-tomography based techniques which include pressure drop and visual measurement. The second section reviews non-nuclear based tomography techniques which include ultrasound tomography, electrical resistance tomography, and electrical capacitance tomography. The last section reviews the nuclear based tomography techniques which utilize X-rays and  $\gamma$ -rays.

### 2.4.1 Non-Tomographic Techniques

#### 2.4.1.1 Visually

In many experiments, gas holdup ( $\varepsilon_g$ ) is measured visually by the following formula:

$$\varepsilon_g = \frac{H_D - H}{H_D} \quad (2.6)$$

where  $H$  is the height of the liquid when no gas is being dispersed and  $H_D$  is the height of the liquid with gas dispersion. When the tank is mechanically agitated, liquid surface fluctuations lead to subjectivity in determining the height. In an attempt to reduce the subjectivity in the measurement,  $H_D$  may be measured at two locations diametrically opposite to each other and between two adjacent baffles (Saravanan and Joshi, 1996). Saravanan and Joshi (1996) determined global gas holdup visually and report that when  $\varepsilon_g$  was less than 0.03, the reproducibility was within 15%. At higher values of holdup, the reproducibility improved to within 10%. Yalwalkar et al. (2001) measured gas holdup the same way as Saravanan and Joshi, but they report slightly different results. When  $\varepsilon_g$  was less than 0.03, the reproducibility

of measurement was within 10%. At higher values of holdup, the reproducibility was the same as what Saravanan and Joshi reported. From the above example, it can be shown that there is some error in measuring gas holdup by visual means. To take some of the error out of measuring the dispersion height, Rushton and Bimbinet (1968) used a level measurement device. The benefits of this procedure are that it is relatively inexpensive and easy to do.

#### 2.4.1.2 Pressure Drop

By measuring the pressure drop along the height of a column, the gas holdup in a two phase system can be determined (Kumar et al., 1997). When the liquid flow rate is small in a gas-liquid system, the pressure drop can be attributed to hydrostatic head:

$$\Delta p = \rho_{\text{eff}} g \Delta h \quad (2.7)$$

where  $\rho_{\text{eff}}$  is the mixture density and  $\Delta h$  is the height between two adjacent pressure probes whose difference is  $\Delta p$ . Substituting for  $\rho_{\text{eff}}$  gives:

$$\Delta p = \left( \frac{V_g}{V_T} \rho_g + \frac{V_L}{V_T} \rho_L \right) g \Delta h \quad (2.8)$$

where V represents volume and the subscript L represents the liquid phase volume, g the gas phase volume, and T the total volume. With the assumption that  $\rho_g \ll \rho_L$ , the above expression simplifies to:

$$\Delta p = \frac{V_L}{V_T} \rho_L g \Delta h \quad (2.9)$$

where  $\frac{V_L}{V_T} = 1 - \varepsilon_g$ . Solving for  $\varepsilon_g$  gives:

$$\varepsilon_g = 1 - \frac{\Delta p}{\rho_L g \Delta h} \quad (2.10)$$

Yung et al. (1979) used a 30 degree inclined manometer to measure the gas holdup in a stirred tank reactor of diameter 0.4 m equipped with a standard six-blade impeller. There results were in agreement with the work of previous investigators.

## **2.4.2 Non-Nuclear Based Tomographic Techniques**

### **2.4.2.1 Ultrasound**

Ultrasound can be used to measure gas holdup, solids concentration, and bubble velocities. Ultrasound measurement is based on the transmission method which is similar to radiation absorption or the time of flight of an ultrasound beam (Kumar et al., 1997).

Ultrasound pulses can be emitted into the liquid with a piezoceramic transducer probe. The transducer can also be used as the receiver to monitor the ultrasound reflections. Chaouki et al. (1997) report that ultrasonic tomography has good spatial resolution of approximately 1 mm with long temporal resolution. Fischer et al. (1992) used ultrasound in a stirred tank reactor to come up with local gas holdup values. The accuracy of the gas holdup was estimated to be around 15%. Compared to X-rays or  $\gamma$ -rays, ultrasound does not have as high of penetration capability. Also, the ultrasound technique has a complicated data analysis procedure which caused Supardan et al. (2004) and Utomo et al. (2001) to use a neural network in analyzing the data obtained using ultrasound in a bubble column.

### **2.4.2.2 Electrical Tomography Techniques**

Electrical tomography techniques are a noninvasive method for imaging the distribution of an electrical property in a medium by using electrodes flush mounted with the medium surface. Electrical capacitance tomography (ECT) is suited for electrically insulating systems while electrical resistance tomography (ERT) is useful for detecting electrically conductive materials (Chaouki et al., 1997). The differences in electrical conductivity or

permittivity are used to map the phase distribution. The electric field is called soft because measurements made are not only a function of the voidage but also a function of the electrical properties and temperature of the medium, and the flow distribution (Kumar et al., 1997). The above effects cause the spatial resolution to be lower than that for X-rays or  $\gamma$ -rays. While having poor spatial resolution, the techniques have great temporal resolution.

Electrical resistance tomography has been used to determine the variation in gas holdup in a stirred tank reactor. Wang et al. (2000) used a 1.5 m stirred vessel equipped with 8-planes of 16-sensor rings and fitted with a Rushton turbine impeller to obtain qualitative results about local gas holdup. Holden et al. (1998) used a similar tank as Wang and were able to distinguish the mixing patterns produced by different impellers. They reported that the accuracy of the imaging data was limited due to the 3-D distribution of the electric fields and reconstruction algorithm. A timewise resolution on the order of  $10^{-1}$  s was reported which allowed for the dynamics of the system to be observed upon the injection of brine. The spatial resolution was reported to be on the order of 4.2% of the vessel diameter.

In the literature, ECT was not found to be used to measure local gas holdup in a stirred tank reactor, but Warsito and Fan (2001) used electrical capacitance tomography to measure local gas holdup in a bubble column of 10 cm I.D. and height 100 cm operating with paraffin as the liquid and air as the gas. Warsito and Fan (2001) report that a drawback of the technique is the low accuracy of the reconstructed image, with the image obtained being qualitative rather than quantitative. The technique is not limited to a maximum gas holdup that can be measured, but small gas holdup values are difficult to measure because the signal to noise ratio becomes small. ECT systems are generally high-speed, being capable of taking

100 frames per second. A group at Morgantown Technology Center has an ECT system with spatial resolution of  $1 \times 2.54 \text{ cm}^2$  (Halow, 1997).

### **2.4.3 Nuclear Based Tomography**

The basis of nuclear imaging techniques results from gases, liquids, and solids having different radiation absorption coefficients. When X-rays or  $\gamma$ -rays are transmitted through a heterogeneous medium, the measurement of the attenuation provides a measure of the local mass density along the path traversed by the beam (Chaouki et al., 1997). By taking measurements of different beam paths at different spatial and angular orientations, a density distribution of phases with high spatial resolution can be obtained after a reconstruction procedure. Because the data collection is automated and performed by a computer, the process is referred to as computed tomography (CT). Scanners are positioned on one side of the tank that include an X-ray tube or encapsulated  $\gamma$ -ray source, with collimated detectors on the other side. The local gas holdup for both techniques is time-averaged due to the length of data collection.

#### **2.4.3.1 $\gamma$ -Ray**

The attenuation of  $\gamma$ -rays has been used to measure the time-averaged local gas holdup in stirred tank reactors. Thatte et. al. (2004) used a  $^{137}\text{Cs}$  source of strength  $67 \mu\text{C}$  to measure gas holdup in a transparent, flat-bottom, cylindrical tank of 0.57 m diameter equipped with a pitched blade downflow turbine or a disk turbine. For both impellers, the average gas holdup was obtained by integrating the local gas holdup and matched well with the results obtained by visual observations. The reproducibility of the measurements was within  $\pm 10\%$ . The scan time for each chordal measurement was 1000 s. Thatte et al. (2004) stated that a higher strength source would reduce the scan time, but they used a  $^{137}\text{Cs}$  source

of strength 67  $\mu\text{C}$  due to safety considerations and other advantages such as lower noise and background scatter associated with a lower powered source. Khopkar et al. (2005) used a  $^{137}\text{Cs}$  source with seven NaI detectors to measure gas holdup in a flat bottomed cylindrical tank of diameter 0.2 m with a shaft that extends to the bottom. The total scan time was a little over 3 hours. Khopkar et al. (2005) noted that CT results were sensitive with respect to the convergence criterion used during processing the raw data. The technique, unlike X-rays, also works on larger tanks because the  $\gamma$ -rays are strong enough to pass through various metals overcoming the reactor wall thickness. Veera et al. (2001) used a  $^{137}\text{Cs}$  source to measure gas holdup in a three-phase industrial scale stirred tank reactor of 4.9 m diameter equipped with 2 impellers.

#### **2.4.3.2 X-ray**

The attenuation of X-rays has not been used to measure the local gas holdup in stirred tank reactors, but work has been done on measuring the time-averaged local gas holdup in bubble columns. Compared to the  $\gamma$ -ray technique, X-ray tomography allows a better spatial resolution due to the small size of the detectors and is safer. However, X-rays lack the penetrative power of  $\gamma$ -rays and are better suited for smaller test sections. Hubers et al. (2005) measured the local gas holdup in a bubble column of 32.1 cm internal diameter with an air-water or air-water-cellulose fiber mixture. Within 10 mm of the wall, the gas holdup values were unable to be obtained due to curvature effects of the column and the applied beam hardening correction (Heindel et al., 2005). Harvel et al. (1999) also used X-ray CT to measure the void fraction distribution in a bubble column. To increase the temporal resolution, the group used 18 X-ray sources and 122 detectors to obtain a cross-section sampling time of 4.0 ms and a spatial resolution of 2.0 mm.

## **2.5 Literature Review Summary**

Numerous studies have been conducted to determine gas holdup in a stirred tank reactor. Gas holdup is a very basic measure of gas-liquid contacting. The knowledge of local gas holdup can be used for process optimization and process intensification. The work of this thesis will be to determine local gas holdup profiles in a STR using X-ray CT.

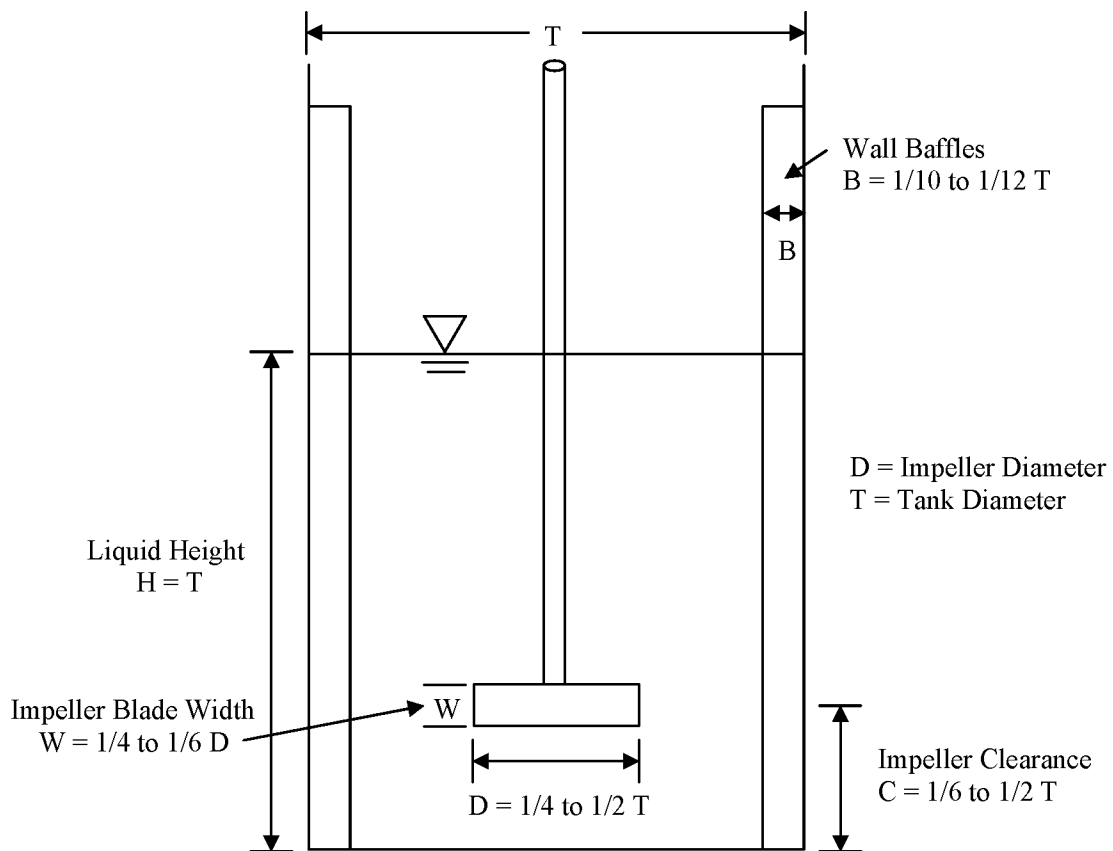


**Figure 2.1:** Stirred tank reactor standard geometry (Adopted from Tatterson, 1991).

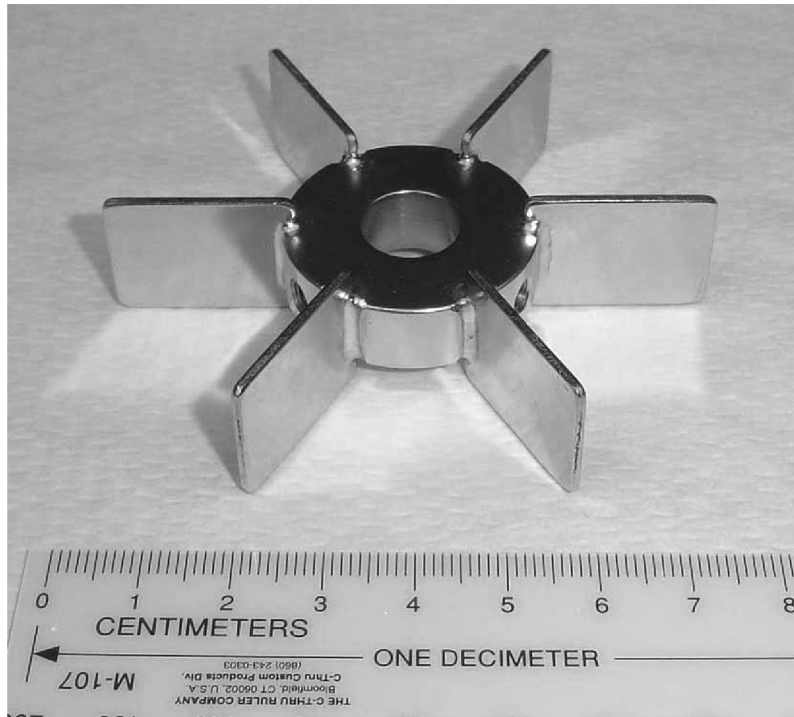


**Figure 2.2:** Standard six blade Rushton turbine used by Ungerman (2006).

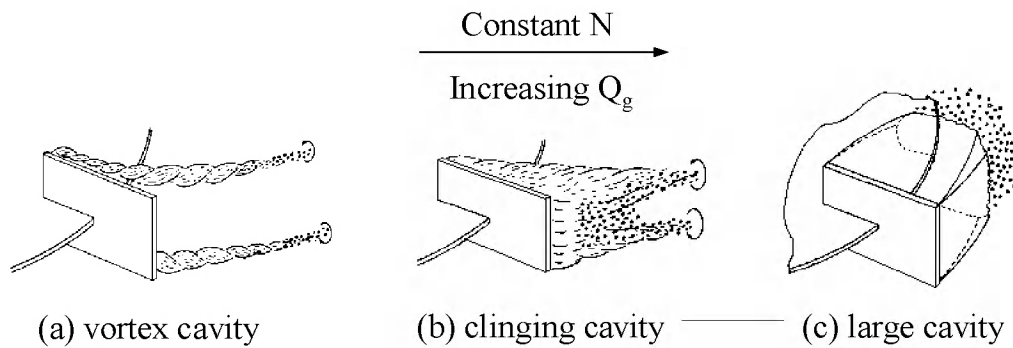


**Figure 2.3:** Progression of cavities with increasing  $Q_g$  and constant  $N$  (Smith and Warmoeskerken, 1985).

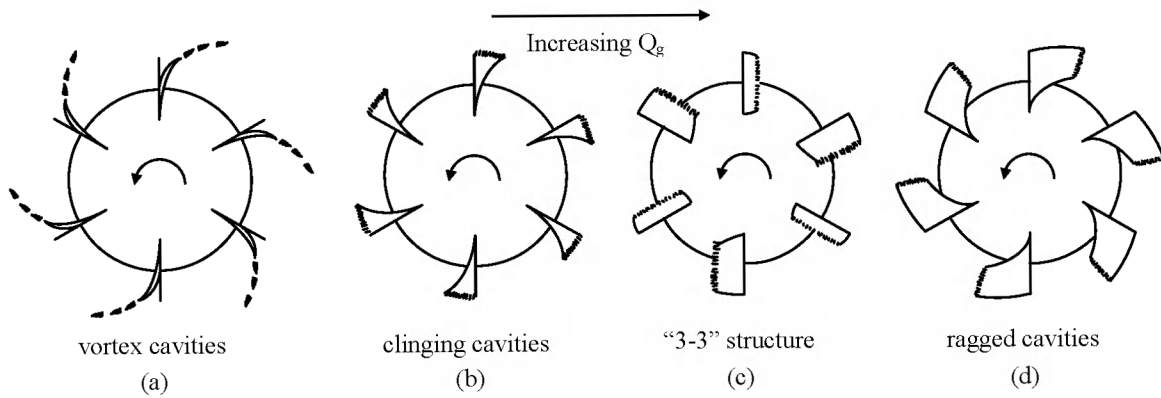


**Figure 2.4:** Cavity structure with increasing  $Q_g$  at constant  $N$  (Smith and Warmoeskerken, 1985; Nienow et al., 1985).

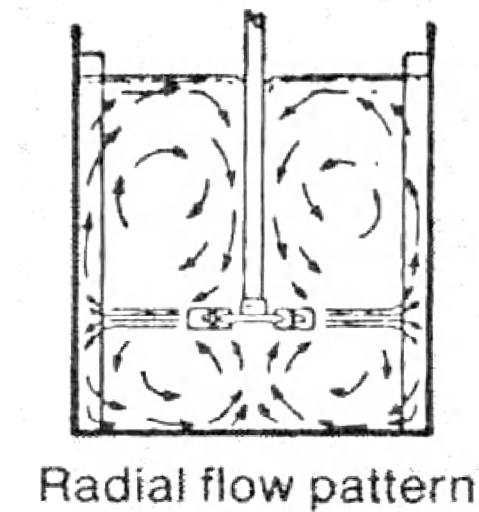


**Figure 2.5:** Radial flow pattern of a Rushton impeller (Barona, 1979).

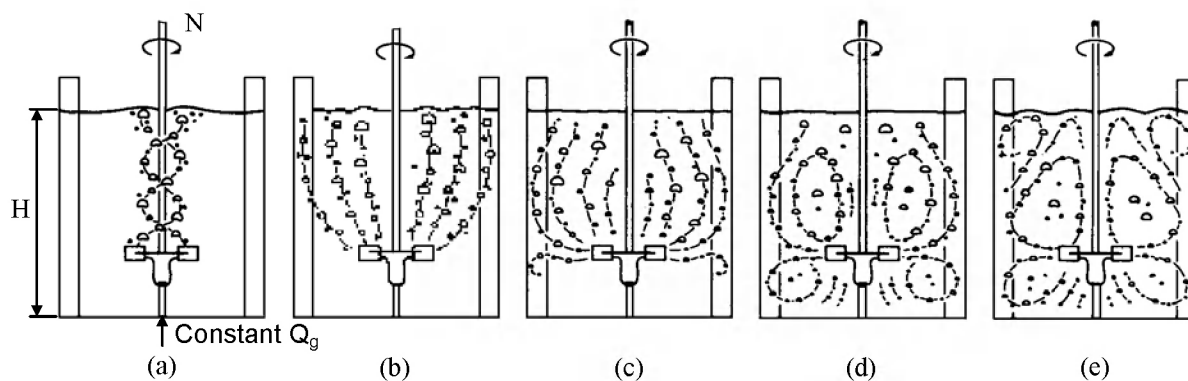


**Figure 2.6:** Bulk flow patterns at constant gas flow rate  $Q_g$  while increasing impeller speed  $N$  from left to right (Nienow et al. 1977).

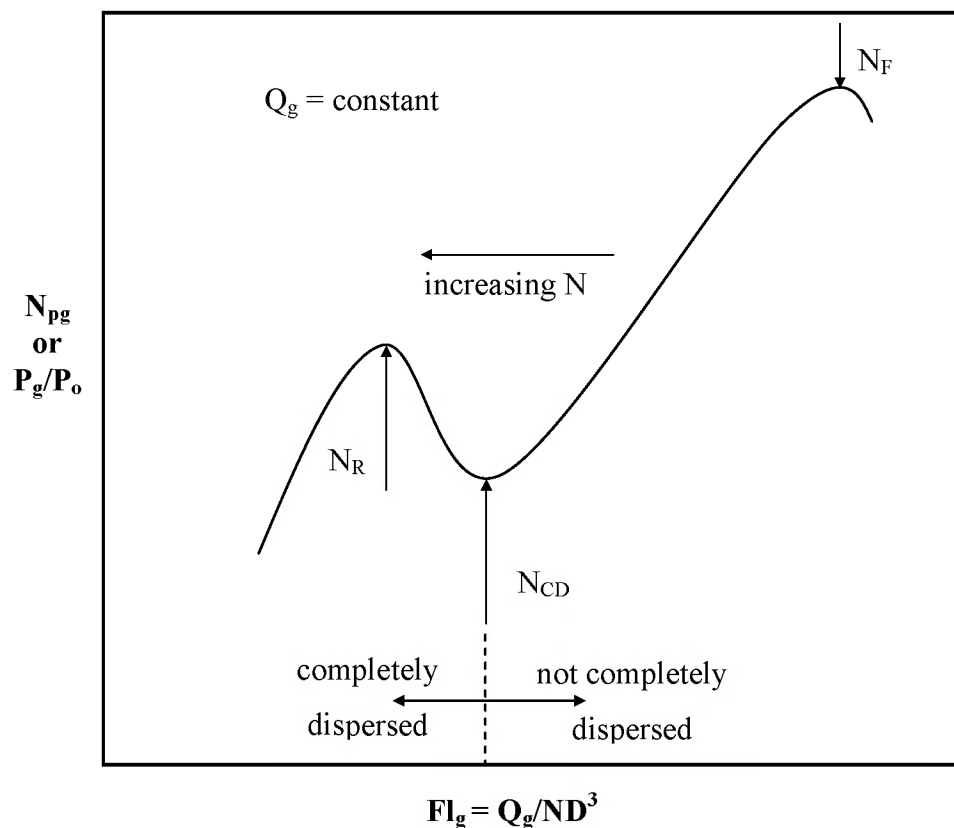


**Figure 2.7:** Generic plot of gassed power number as a function of flow number with  $Q_g =$  constant (Kapic, 2005).

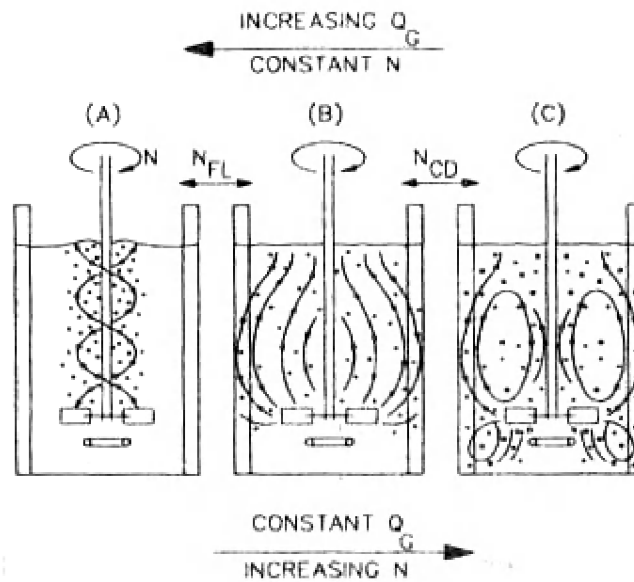


**Figure 2.8:** The three gas loading transitions for a Rushton turbine; (a) flooding, (b) loading, (c) and completely dispersed (Nienow et al., 1985).

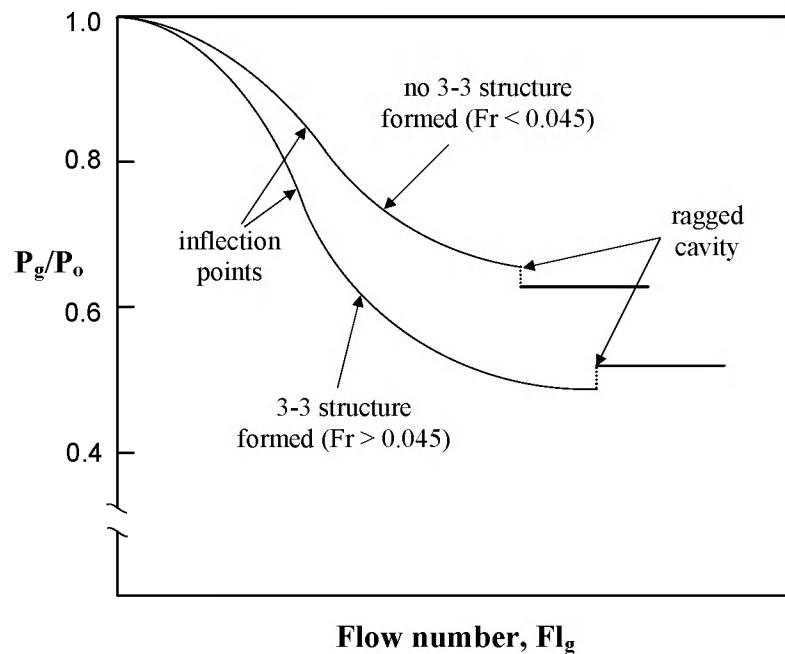


**Figure 2.9:** Gassed power ratio at constant  $N$  (Nienow et al., 1985).

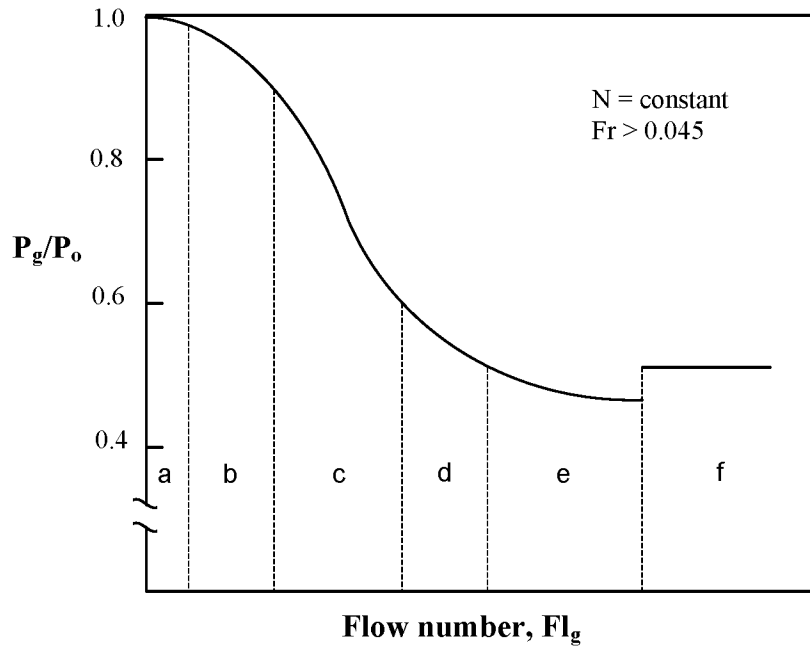


**Figure 2.10:** Cavity formation of a gassed power curve (Kapic, 2005).

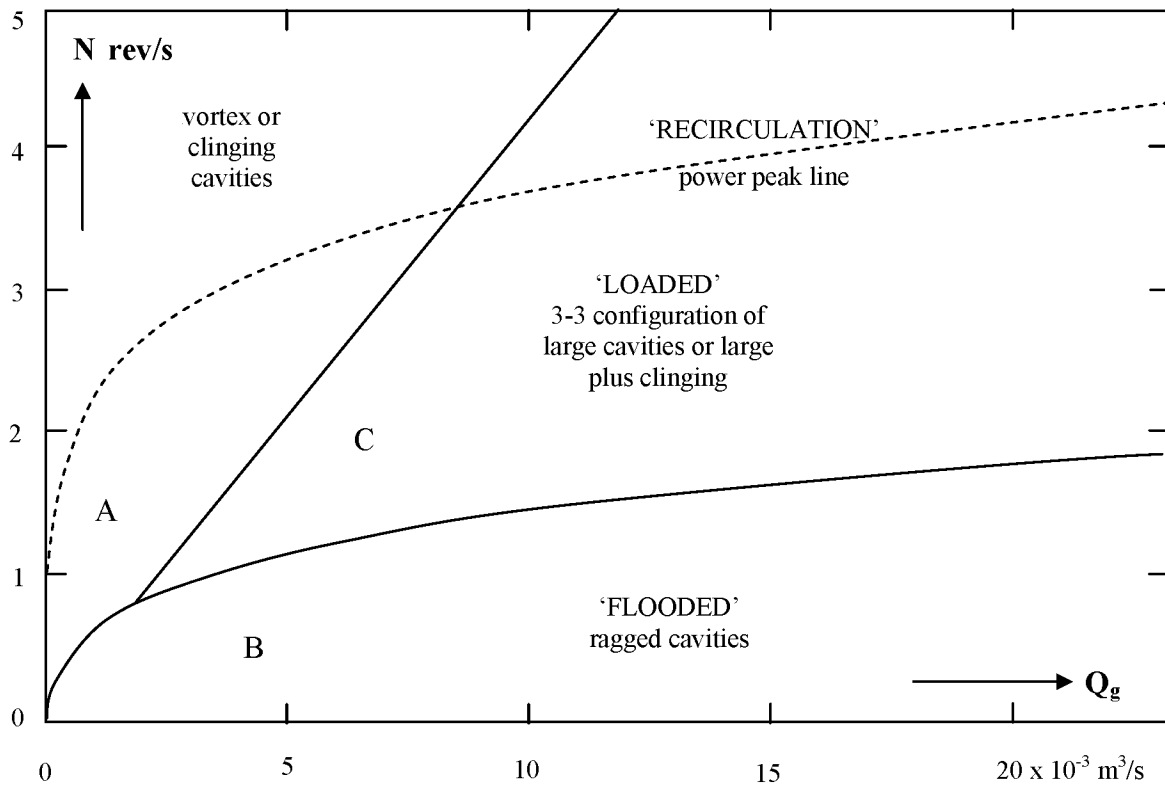


**Figure 2.11:** General flow map for a STR with  $T = 1.2\text{m}$  and  $D = 0.48\text{ m}$  (Smith and Warmoeskerken, 1985).

## CHAPTER 3: EQUIPMENT AND EXPERIMENTAL METHODS

This chapter is divided into 4 sections. The first section provides an in depth description of the stirred tank reactor (STR) used in this study. The second section describes the method used to measure power consumption in the STR. The third section gives a description of the X-ray system located in Black Engineering at Iowa State University (ISU). The last section describes the X-ray data acquisition and reduction to yield local gas holdup data.

### 3.1 Stirred Tank Reactor Description

Experiments are carried out in a STR fabricated from acrylic by Country Plastics in Ames, Iowa. The acrylic STR is comparable in size and shape to a BioFlo 110 Fermenter (New Brunswick Scientific Co.), which are off-the-shelf STRs used for fermentation and academic studies. The dished-bottomed tank (Fig 3.1) is made out of acrylic to prevent image artifacts during the CT scans (Ketcham and Carlson, 2001). The reactor has an internal diameter of  $T = 21$  cm. The tank walls are 0.64 cm thick. Tap water is used as the working fluid and filled to a height of  $T = H$  which corresponds to a volume of approximately 7 liters. The region bounded by slice 0 and slice 200 in Fig. 3.1 correspond to the approximate CT reconstruction region discussed in Chap. 4.

The impeller shaft and Rushton impeller are both made out of nylon because acrylic is too brittle. The 6-blade Rushton impeller has a diameter of 7.56 cm which corresponds to  $D = 0.36T$ . The impeller blades have a height of 1.9 cm and a thickness of 0.3 cm (Fig. 3.2). The impeller hub has a diameter of 3.1 cm. Unlike most STRs, the acrylic one in this study

has a shaft that penetrates the bottom of the tank to provide stability. The hole in the acrylic STR bottom into which the shaft is inserted acts as a bearing; if the shaft did not rest in this hole during operation, the flexible nylon shaft would wobble violently. The impeller is located 5.7 cm from the STR bottom, which corresponds to  $C = 0.27T$ . Gas is introduced into the tank through an acrylic ring sparger of diameter 5.1 cm, which is attached to the STR bottom and wrapped around the bottom disk instead of located off the bottom (typical of most STRs). The tank has 4 equally spaced baffles of length 1.8 cm and thickness 0.6 cm glued directly to the tank wall. The impeller is driven by a variable speed DC motor mounted on the top of the STR and connected to the BioFlo 110 Primary Control Unit (PCU) manufactured by New Brunswick Scientific Co. The motor and STR top are from the BioFlo 110 STR.

In summary, the dimensions of the tank correspond well with the dimensions noted in section 2.1 and given by Tatterson (1991) for a standard STR. Even though the acrylic STR used in this study corresponds to the standard geometry, it should be noted that there are two main differences from the standard design. The impeller shaft overall length and sparger location from the tank bottom do not conform to the standard geometry due to the materials needed to build the STR to provide the best CT images.

### **3.2 Power Measurements**

The motor used to drive the impeller is manufactured by Magmotor Corporation (model number C32-E-450X). For measuring power consumption (Fig. 3.3), an Electro model PS-5R rectifier is used to supply the motor with a constant DC voltage. The power draw is measured by connecting an EXTECH Instruments True RMS Power Analyzer in

parallel between the PCU and DC power supply. The desired impeller speed (N) is obtained by adjusting the power supply and is measured by an internal tachometer in the PCU.

The power draw of the impeller can be calculated by the following formula:

$$P_{\text{mech}} = 2\pi N\tau \quad (3.1)$$

where care must be taken to ensure that the true impeller torque  $\tau$  can be isolated from torque loads caused by friction. The mechanical torque losses can be determined by power measurements without a load on the impeller. Therefore, the mechanical power, which is the power transmitted to the gas-liquid dispersion, can be calculated by:

$$P_{\text{mech}} = P_1 - P_e \quad (3.2)$$

where  $P_1$  represents the power draw with a load and  $P_e$  represents the power draw without a load. Because of the tank design and the fact that the shaft goes down to the bottom of the tank, 3 cm of water remained in the bottom of the tank below the impeller when  $P_e$  was determined to protect the shaft from excessive wear. In this experiment, it should be noted that the mechanical torque losses are assumed to be the same regardless if the system is gassed or ungassed.

Before power measurements are taken, the motor is allowed to warm up for 1 hour. After the gas flow rate is set and the desired impeller speed is steady, the current, voltage, and the product of the two, which represents the electric power, are measured by the power analyzer that is connected to the computer through an RS-232 serial port. For each measurement, 200 data points are recorded at a frequency of 2 Hz, with the mean value being recorded. For each specific gas flow rate and impeller speed, 3 measurements are taken with the mean value being used as the accepted value.

The standard error values for the power measurements ranged from 0.04 W to 0.48 W. Percent standard error values ranged from 0.42% to 23.5%, with most values below 10%. The measurements made at the lower impeller speeds tended to have a higher percent standard error.

### **3.3 X-Ray System Description**

The X-ray source used in this study is a LORAD LPX200 (Fig. 3.4), which has a focal spot of 1.5 mm. The source emits a conical beam and allows for multiple CT slices to be acquired during a single scan. The unit is liquid cooled and has an adjustable voltage (10 – 200 kV) and current (0.1 – 10.0 mA) with a maximum power of 900 W.

A 44 × 44 cm cesium-iodide scintillator screen is used to convert the X-rays into light that can be read by a 50 mm Nikkor lens connected to a CCD camera. The detector is on a movable slide which enables the magnification factor to be adjusted. The CCD camera used to digitize the image is an Apogee Alta U9 system with a sensor array of 3072(H) × 2048(V) pixels, with a pixel size of 9 μm × 9 μm. The CCD camera is thermoelectrically cooled allowing longer exposures with low-noise, thereby making it suited for providing superior CT images. The camera has binning capabilities (resolution settings) of 1×1, 2×2, 3×3, 4×4, 5×5, 6×6, 7×7, 8×8, 1×2, 1×3, 2×3, and 2×4. The exposure time of the camera can range from 0.1-100 sec.

The source and camera are mounted on a slew ring with an ID of 101.4 cm, which allows the source and detector to rotate around the STR during a CT scan. The ring is rotated by a Parker stepper motor with a limit switch attached at the position assigned 0° to prevent

the cooling cords from being wrapped around the stand. When CT scans are taken, the system is automatically rotated to  $360^\circ$  and then rotates back to  $0^\circ$  at the chosen increment.

The X-ray system is enclosed by walls composed of 0.476 cm lead attached to 2.54 cm plywood to stop scattered X-rays. The X-ray system also has the safety feature that all the power runs through an interlock connected to the main X-ray door. If the door is opened, the X-rays and pumps automatically shut off. Before the X-rays are turned on, there is a 10 sec wait where a warning light flashes inside the X-ray vault. In the case that someone did not see the warning light, there is a stop button located inside the imaging room.

There is a standard operating procedure to prevent damage to the X-ray source. Before X-ray operation, the pump is turned on and the X-ray system goes through a warm-up procedure with time depending on when the system was last used. After the imaging for the day is done and the X-rays are turned off, the pump is left on for 5 min. to allow cooling of the X-ray source. More details regarding the X-ray system, controls, and operation may be found in Hubers (2005) and Striegel (2005).

### **3.4 X-ray Data Acquisition and Reduction**

This section is divided into 4 subsections and provides a review of the X-ray data acquisition and reduction. The first subsection describes the CT scan procedure. The next two subsections provide a description of the procedures used to correct the acquired images for two common problems in CT imaging. The last subsection provides a description of the procedure used to convert the CT data into local gas holdup data.

### 3.4.1 CT Scan Procedure

Computed tomography (CT) produces images of a cross-sectional plane (slice) through an object. A slice is a quantitative map of the linear X-ray attenuation coefficient  $\mu$ . Since the X-ray system in Black emits a conical beam, multiple slices can be acquired during a single scan thereby producing a volumetric rendering of the object. The slice is created by acquiring images at different angular orientations. For the data taken in this study, X-ray images were taken every  $1^\circ$  around a  $360^\circ$  path. Since it takes time to acquire the 360 images, the data in a reconstructed CT image is a time average of the events during the acquisition period. In this study, a typical scan lasts approximately 43 minutes with the camera binning options set to  $4 \times 4$ . Scan time can be reduced by increased camera binning and larger angular steps at a cost of lower spatial resolution.

The intensity values from the 360 images are stored in a sinogram file (.sin). The sinogram name comes from the fact that a single point in a scanned object corresponds to a sinusoidal curve. Each sinogram file contains the information for 10 slices.

CT data are reconstructed utilizing a filtered back projection algorithm to provide a volumetric rendering of the image (Barrett and Swindell, 1981; Hsieh, 2003). During reconstruction, the intensity data in the sinogram files are converted to gray scale CT values, which correspond to the linear attenuation coefficient. It should be noted that the correspondence of the CT values to the linear attenuation coefficient is not absolute, but depends on the reconstruction software. Two versions of the reconstruction code are available for use at ISU. The first version allows for the reconstruction of a single slice, which was written in Visual C++ by Yan (2000). To be able to reconstruct all the slices into a single volume file (.vol), software was developed by Zhang (2003) that runs on a 64-node

LINUX cluster located at the Center for Nondestructive Evaluation. Reconstruct using the 64-node cluster typically takes less than 5 minutes. Before the data are sent over to the cluster, a variety of image corrections are applied to produce the best CT images. The two main corrections are for individual pixel nonuniformity and beam hardening, which will be discussed in the next two subsections.

The system settings for this study were carefully selected. With a 1 mm copper filter placed in front of the source to filter out the lower energy X-rays, the voltage was set at 136 kV with a 5.7 mA current for a power output of 775.2 W. The camera exposure time was set at 1 sec. The temperature on the CCD chip was set to 0° C with the camera in 4×4 binning mode. These settings allowed for the highest intensity through the thickest parts of the tank.

In a preliminary data set of a scan taken with the tank filled with water and no impeller movement or gas sparging, it was noticed that the gray scale value of water varied with height. In a scan of uniform material, the gray scale CT value should be approximately constant. The variation was caused by Compton scattering of X-rays. To cut down on Compton scattering, two steps were taken. First, the detector was pulled back as far as possible from the source to a distance of 1.87 m. This prevented many of the scattered X-rays from hitting the detector screen. Secondly, lead shutters, which can be seen in Fig. 3.4, were used to stop X-rays that were not going through the area of interest. Due to the limitations of the X-ray system to image a region not much greater than the size of a bread loaf, a region corresponding to 1 impeller diameter in height was chosen to image. The region starts at the bottom of the impeller and goes vertically up one impeller diameter. The above imaging region was chosen due to the differences in flow regimes around the impeller for different

operating conditions. The imaging region chosen comprises a total of 200 slices and extends from slice 0 (at the top) to slice 200 (at the bottom) in Fig. 3.5.

The CT scan procedure was also important to provide accurate data. At the start of the day, the X-ray system is put through a warm up procedure with the lead shutters covering the X-ray source. Then, the shutters are opened to the desired height and the X-rays are turned on at 136 kV and 5.7 mA for 20 min. The 20 minute wait is due to residual memory in the cesium-iodide scintillator screen, which is activated by the presence of X-rays. After the gas flow rate and impeller speed are set to the desired condition, a 5 minute wait is allowed to ensure that the STR has reached a quasi-steady state. As discussed above, the time for the motor to rotate  $360^\circ$  and acquire an image at each angle takes approximately 43 min. After a scan is completed, the impeller and gas are turned off for a few minutes before resetting the impeller speed and gas flow rate to the next desired condition. Finally, another 5 minutes is allowed for the STR to again reach quasi-steady-state before starting the next scan. It should be noted that the X-ray controls are left at 136 kV and 5.7 mA until the last scan of the day is completed.

### **3.4.2 Pixel Normalization Correction**

When examining an image, pixel response uniformity must be considered. Ideally, when the detector is illuminated by X-rays, each pixel will respond in a similar fashion. Unfortunately, this is not the case, which leads to a need for a method to correct for this non uniform pixel response.

For this research project, a linear normalization method is used. This algorithm assumes a linear relationship between pixel intensity and X-ray power. The algorithm requires the use of a flat frame (X-rays intensity close to saturating) and a dark frame (no X-

rays). Then an average intensity value for the flat frame is determined. The intensity of each image taken during a CT scan is then adjusted by:

$$I_{\text{new}} = I_{\text{image}} + (I_{\text{image}} - I_{\text{dark}}) \left( \frac{I_{\text{ave}}}{I_{\text{flat}} - I_{\text{dark}}} \right) \quad (3.3)$$

where  $I$  represents pixel intensity, and the subscripts represent the pixel intensity for the linear calibrate value (new), image taken (image), average flat frame (ave), flat frame (flat), and dark frame (dark).

The acquisition of the flat frame is taken after the X-rays are on for 20 minutes at the desired setting. The dark frame is taken 5 minutes after the X-ray source is turned off. When the dark frame is acquired, the camera lens is shut. It should be noted that both the flat and dark frame are acquired by averaging 4 images. A linear normalization correction is applied to each image that is acquired during the CT scan, amounting to 360 individual corrections for an angular step of  $1^\circ$ .

### 3.4.3 Beam Hardening Correction

Beam hardening is an artifact frequently encountered in CT reconstruction which causes the outer surfaces of the object to appear denser compared to the rest of the object (Ketcham and Carlson, 2001). In a polychromatic X-ray beam, the lower energy X-rays are attenuated more readily than higher energy X-rays, which causes the thicker sections to lose more of the lower parts of the energy spectrum resulting in lower CT values for regions in the center of the tank. One method for dealing with beam hardening is to increase the X-ray power and add thicker copper or aluminum filters. This causes the lower energy X-rays to be attenuated by the filter while still providing a decent signal to the detector. Since there is a 900 W limit to the X-ray system in the lab, this method is not suitable. Therefore, another

method is needed. To correct for beam hardening, a wedge calibration is employed using the STR filled with water. The beam hardening correction works by applying a correction factor to all the sinogram files before reconstruction.

To find the correction factor, an image of the water filled STR is taken with no impeller movement or gas sparging at the same voltage and current as the CT scans. Then, the intensity  $I$  is recorded along with the corresponding thickness ( $L$ ) of material through which the X-ray beam must pass. The attenuation of X-rays in a material is governed by:

$$I = I_0 \exp(-\mu L) \quad (3.4)$$

where  $\mu$  is the linear attenuation coefficient and  $I_0$  is the intensity of the incident X-ray beam.  $I_0$  is found by taking an average of pixels in the air region near the tank edge at the given X-ray current and voltage. For this study,  $I_0$  is 64,150. From the above equation,  $\ln(I_0/I)$  must be directly proportional to thickness. Therefore, a plot of  $\ln(I_0/I)$  vs.  $L$  (Fig. 3.6) should produce a line with slope  $\mu$  if there is no beam hardening (or the thickness is small). Beam hardening produces a nonlinear slope. Because the measurements of  $\ln(I_0/I)$  must be proportional to thickness, the difference between the tangent line as  $L \rightarrow 0$  and the actual slope  $\mu$  at  $L$  is calculated. The difference between the two lines is then plotted as a function of  $\ln(I_0/I)$ , with a fifth degree polynomial being fit to the result (Fig. 3.7). The fifth degree polynomial is the correction equation which is applied to the sinogram files to properly account for beam hardening.

Beam hardening corrected data are shown in Fig. 3.8, which shows the CT values along a line through the tank center for a water only scan with and without the correction applied. In a water only scan, the CT values should be constant, but that is not the case as seen by the bottom plot of an uncorrected slice. The top plot shows values along the same

line after the beam hardening correction has been applied. As shown in Fig. 3.8, the top plot is fairly constant with a slight increase towards the center. By comparing the two plots, it can be seen that the beam hardening correction introduces more noise. The noise added by applying the beam hardening correction can be reduced by a technique discussed in section 3.4.4.2.

### 3.4.4 Determining Local Gas Holdup

This subsection is divided into 2 smaller subsections and describes a method for determining local gas holdup from CT data. The first section describes the derivation of an equation used to turn the CT data into gas holdup data. The second section describes how the values in the equation are determined.

#### 3.4.4.1 Gas Holdup Equation

Gas holdup, which is the volumetric gas fraction in a mixture, can be obtained from CT values by (Hammer et al., 2006) rearranging equation (3.4) to give:

$$\ln\left(\frac{I_o}{I}\right) = \mu L \quad (3.5)$$

Here  $\mu$  represents the mixture's effect on intensity attenuation which can be broken down into components by:

$$\mu L = (\mu_g L_g + \mu_l L_l) \quad (3.6)$$

where  $\mu_g$  is the linear attenuation coefficient for air,  $\mu_l$  is the linear attenuation coefficient for water,  $L_g$  is the length of air in the total length  $L$ , and  $L_l$  is the length of liquid in the total length  $L$ . Multiplying the right side of eq. (3.6) by  $L/L$  gives:

$$\mu L = \left( \mu_g \frac{L_g}{L} + \mu_l \frac{L_l}{L} \right) L \quad (3.7)$$

Since  $L_g/L$  represents the volumetric fraction of air (gas holdup,  $\varepsilon_g$ ) along the beam path, eq.

(3.7) can be reduced to:

$$\mu L = (\mu_g \varepsilon_g + \mu_l \varepsilon_l) L \quad (3.8)$$

where  $\varepsilon_l$  represents the volumetric fraction of liquid. The volumetric fractions of the components must sum to one:

$$\varepsilon_g + \varepsilon_l = 1 \quad (3.9)$$

Combining eq. (3.8) and (3.9) yields:

$$\mu L = \mu_g \varepsilon_g L + \mu_l (1 - \varepsilon_g) L \quad (3.10)$$

and solving for  $\varepsilon_g$  gives:

$$\varepsilon_g = \frac{\frac{\mu}{\mu_l} - 1}{\frac{\mu_g}{\mu_l} - 1} \quad (3.11)$$

When CT values are used, eq. (3.11) becomes:

$$\varepsilon_g = \frac{\frac{GS}{GS_l} - 1}{\frac{GS_g}{GS_l} - 1} \quad (3.12)$$

where GS represents the gray scale CT value from the CT slice images. It should be noted that eq. (3.12) assumes a monochromatic radiation source. Because a copper filter has been utilized, most of the energy passing through the column is of high energy, which has effective attenuation coefficients that are very close to constant (Ketcham and Carlson, 2001).

#### 3.4.4.2 Determination of Gray Scale Values

The value for  $GS_g$  is determined by taking a CT scan with no water in the tank and a stationary impeller. Beam hardening is not a problem for the air scan since there is not that much material through which the X-rays travel. Therefore, the value of air is assumed to be constant. To get an accurate value for  $GS_g$ , the values of 5 vertical lines (i.e., 5 points in each of the 200 slices) comprising 1000 values are averaged to yield a value of  $GS_g = 23.12$ .

The value for  $GS_l$  is determined by taking a CT scan with water in the tank and no impeller movement or gas sparging. The impeller is left stationary to prevent air surface entrainment. From Fig. 3.8, it can be seen that even after the CT values are corrected for beam hardening, the CT value for water is not exactly constant. To combat this problem and reduce the noise in the data, a computer program was written in Microsoft Visual C++ .Net that averages the data. A new .vol file is created by completing a  $3 \times 3 \times 3$  pixel average for each pixel in the original .vol file; this average includes 9 pixel values from the slice above, 9 values from the slice including the pixel, and 9 values from the slice below. The averaging technique is applied to every pixel in the original .vol file with the exception of the outer pixels of each slice, and the top and bottom slices. Therefore, the top and bottom slices are not included in the analysis of data in Chap. 4. The same averaging technique is also applied to the CT scans during STR operation.

With the values for eq. (3.12) determined, a slightly different version of the code was written to apply eq. (3.12) to each pixel. First, the program opened the 2 newly created .vol files. To determine the value  $GS/GS_l$ , the average pixel values for  $GS$  are divided by the corresponding average pixel values for  $GS_l$ . The value  $GS_g/GS_l$  is determined by taking the constant value for  $GS_g$  divided by the average pixel values for  $GS_l$ . After applying eq. (3.12),

the data is then written to a new .vol file that contains local gas holdup data. By not holding the value of  $GS_1$  fixed, the features of the tank are clearly visible in the newly created .vol file (to be shown in Chap. 4). Also, the slight increase of  $GS_1$  towards the center is minimized by dividing pixel by pixel.

Before the .vol file is opened in the 3-D visualization software package, which allows slices to be made on all 3 axes, some adjustments are made to the .vol file to make the images easier to view. The noise is limited by assigning ranges of gas holdup values to a certain gray scale value. If the gas holdup value turned out to be less than zero, which happened near solid regions, the gas holdup value was set to 0. The gas holdup values were mapped to 8-bit grayscale values. It should be noted that the mapping of gas holdup values is only applied for qualitative analysis. All quantitative analyses are done using the unmapped gas holdup data, which is obtained in 16-bit grayscale.

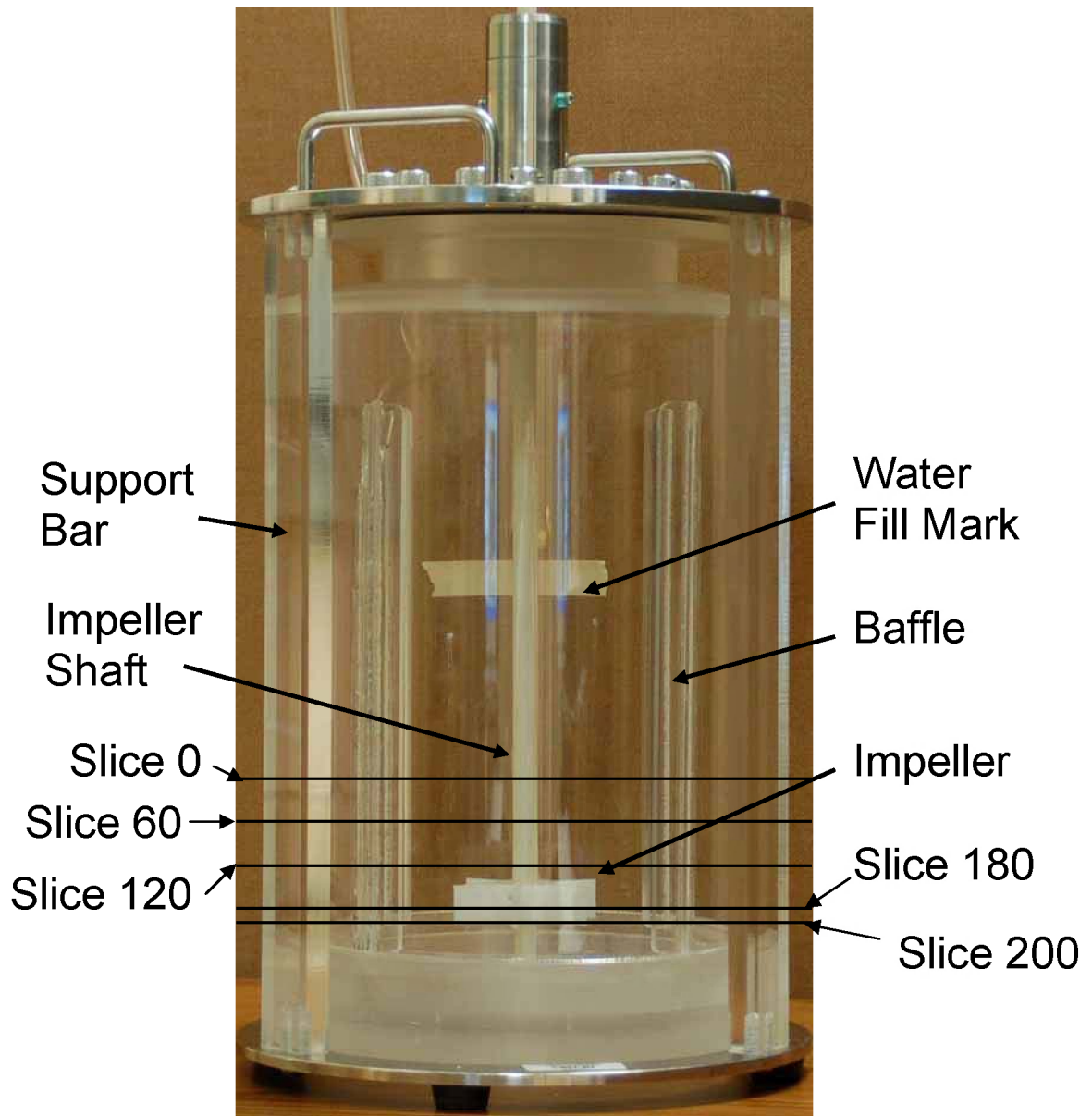


**Figure 3.1:** Stirred tank reactor used in this study.

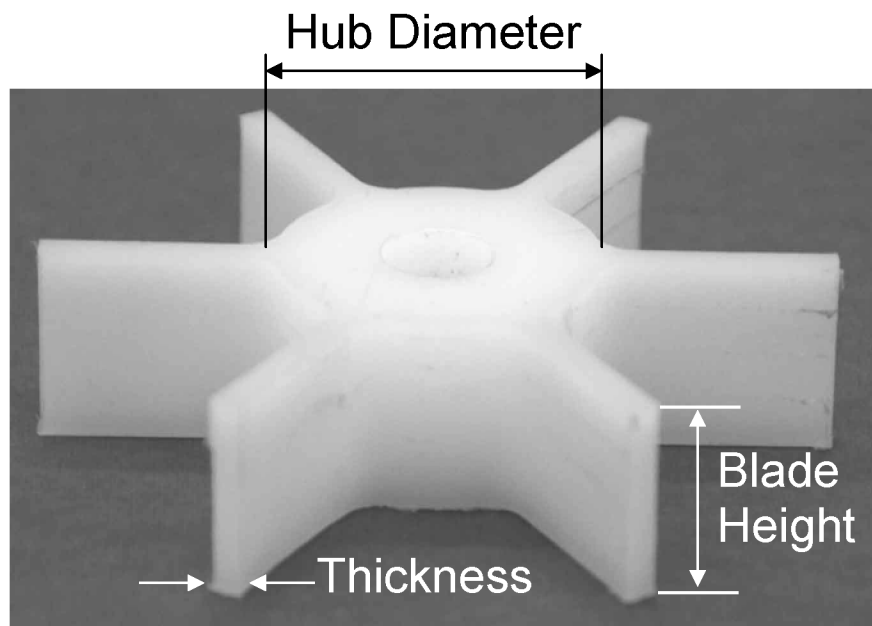


**Figure 3.2:** Impeller.

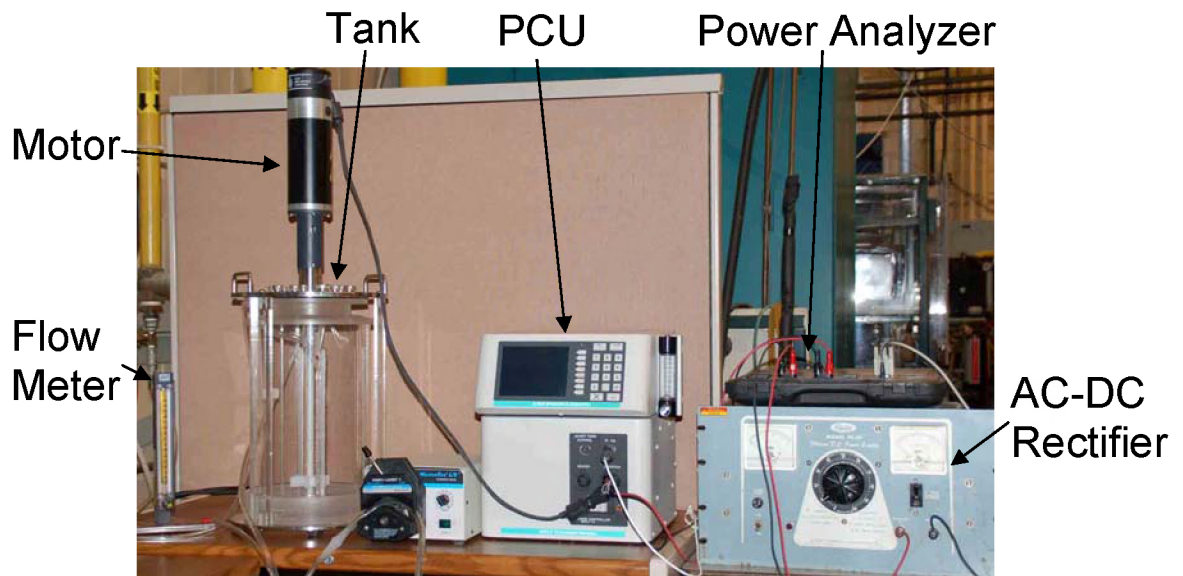


**Figure 3.3:** Power measurement setup.

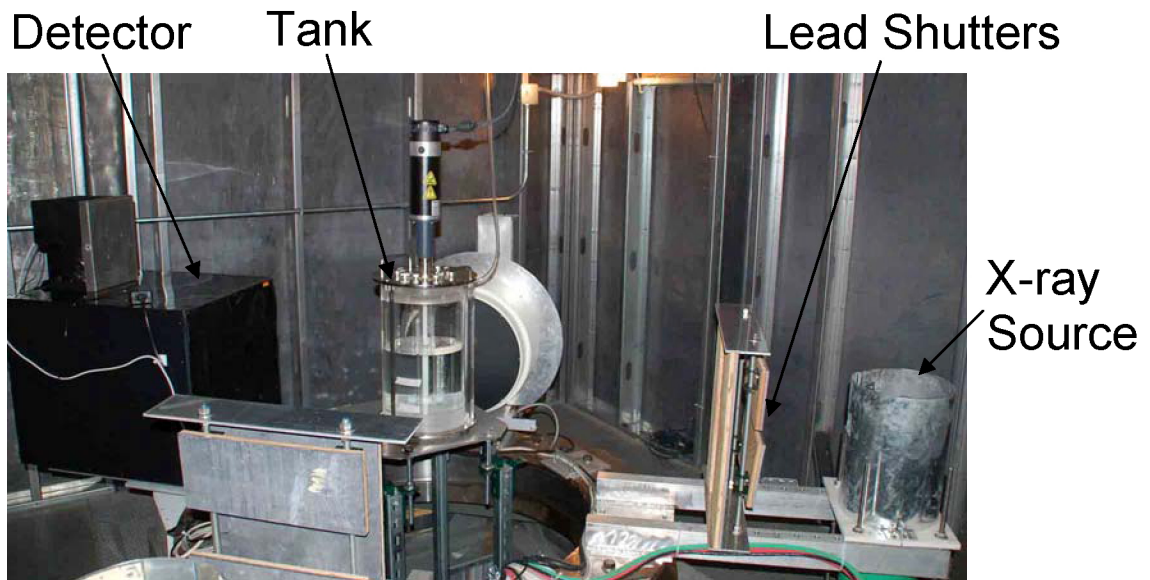


**Figure 3.4:** X-ray system setup.

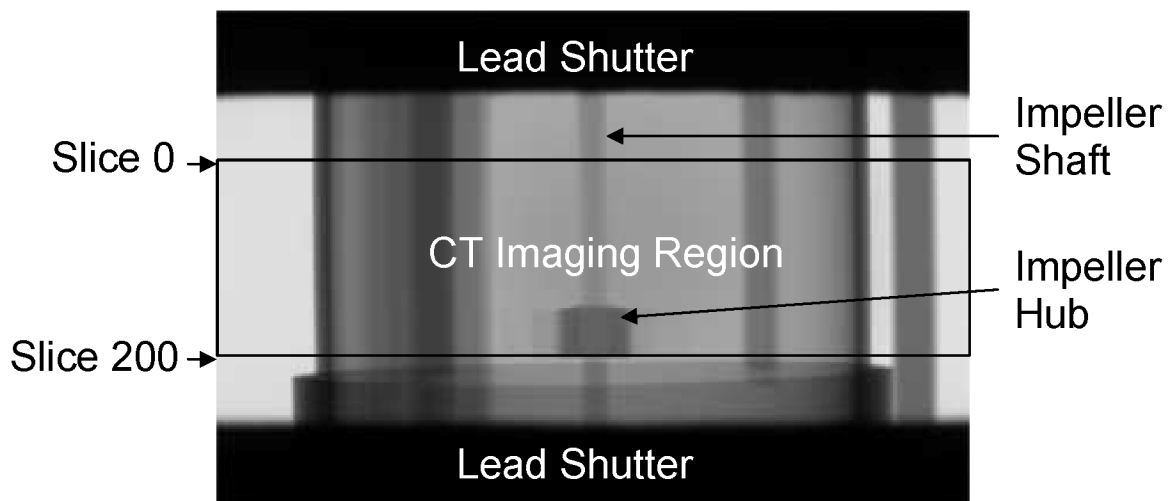


**Figure 3.5:** X-ray image of empty STR.

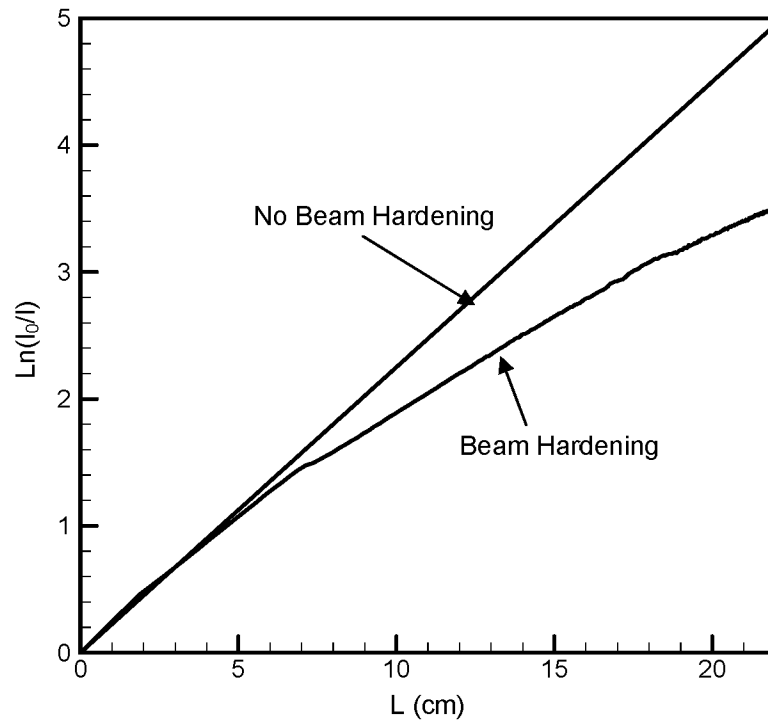


**Figure 3.6:** Plot of  $\ln(I_0/I)$  vs.  $L$ .

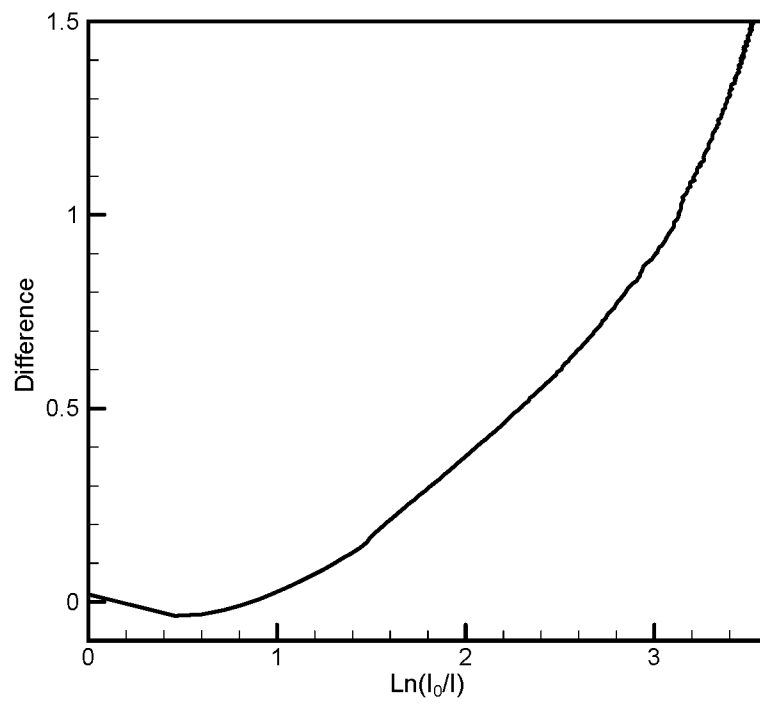


**Figure 3.7:** Plot of difference vs.  $\ln(I_0/I)$ .

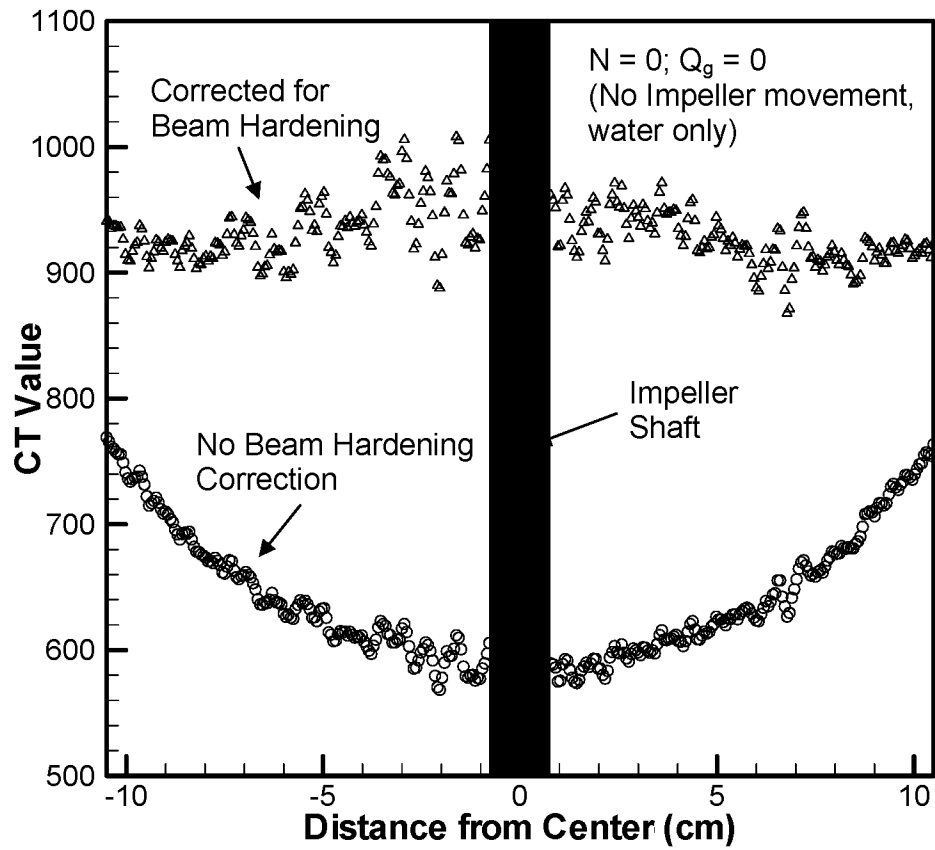


**Figure 3.8:** Plot showing line with and without beam hardening correction.

## CHAPTER 4: RESULTS AND DISCUSSION

This chapter summarizes the results of this study and is divided into 2 sections. The first section presents the results from the power measurements. The second section provides qualitative and quantitative results for local gas holdup from CT measurements and error quantification.

### 4.1 Power Measurement

Power measurements were taken in the  $T = 0.21$  m STR filled with tap water to a height  $H = T$ . The impeller speed ranged  $200 \leq N \leq 800$  rpm while the air flow rate ranged  $1 \leq Q_g \leq 15$  LPM. For all the measurements, air was sparged through a ring sparger located on the tank bottom. Power measurements were taken with constant  $N$  values of 400, 600, and 800 rpm or constant  $Q_g$  values of 3, 6, 9, and 12 LPM. These values were chosen to study the hydrodynamics for a wide range of operating conditions. To confirm the power measurements could be used to predict the various flow regimes (Nienow et al., 1985), the transitions between regimes were determined visually and photographed with a Nikon D50 digital camera using a shutter speed of 1/4000 sec and an aperture of F16.

Figure 4.1 shows the mechanical power for unaerated ( $Q_g = 0$  LPM) and aerated conditions at constant  $Q_g$  as a function of impeller speed  $N$  in rev/s. The gassed power increases with increasing impeller speed and generally decreases with increasing air flow rate because the added gas increases the cavity size behind each impeller blade; this lowers the effective viscosity of the air-water pseudo-liquid and decreases the mechanical power.

Figure 4.2 shows the ungasged power number  $N_{po}$  as a function of Reynolds number. Generally,  $N_{po}$  is not constant and varies with the Reynolds number. However, for a stirred tank reactor operating in the turbulent regime ( $Re > 2 \times 10^4$ ), the ungasged power number is essentially constant. This observation has been reported by others (Nienow, 1998; Kapic, 2005). The average power number over the given Reynolds number range is 4.9, which is close to 4.8, the number determined by Kapic (2005) for a similar STR.

#### 4.1.1 Constant Gas Flow Rate

A common way of taking power measurements is to hold the gas flow rate constant while varying the impeller speed  $N$ , which gives a family of curves like those in Fig. 4.3 when the gas power number  $N_{pg}$  is plotted as a function of flow number  $Fl_g$ . The bulk flow patterns shown in Fig. 2.6 are covered while holding  $Q_g$  constant, by starting at  $N = 200$  rpm and increasing the impeller speed in increments of 25 rpm. It should be noted that not all transitions ( $N_f$ ,  $N_{cd}$ ,  $N_r$ ) are recorded for all gas flow rates because they did not all occur in the impeller speed range of 200-800 rpm chosen for this study. When looking at the graph, it should be noted that the impeller speed increases from right to left.

At low impeller speeds and high gas flow rates, flooding occurs, which is characterized by a bubble column flow where the bubbles rise vertically and are virtually unaffected by the rotating impeller. Flooding is the least desired operating regime due to the lack of dispersion, which leads to a low gas holdup and low mass transfer rate. The local max labeled  $N_f$  in Fig. 4.3 corresponds to the flooding/loading transition. To the right of  $N_f$ , the impeller is flooded, while to the left of  $N_f$  the tank is said to be loaded and the impeller acts to disperse the bubbles radially outward in the upper part of the vessel. The progression from flooding to loading for  $Q_g = 9$  LPM can be seen in Fig. 4.4, where these pictures correspond

to the identified locations (1)-(3) in Fig. 4.3. Figure 4.4a shows the tank when the impeller is not moving and no gas is being sparged. Figure 4.4b corresponds to location (1) in Fig. 4.3 where  $N = 200$  rpm; here bubbles mainly rise along the shaft and the impeller is flooded and looks like Fig. 2.6a. The impeller is actually moving but the high shutter speed of the camera provides stop-motion images. Figure 4.4c (location (2) in Fig. 4.3) resembles Fig. 2.6b, where at  $N = 225$  rpm the impeller is still flooded and the bubbles are radially dispersed in the upper regions of the tank. At  $N = 250$  rpm (Fig. 4.4d; location (3) in Fig. 4.3), the bubbles are dispersed radially in all regions above the impeller and the impeller is loaded. Therefore, by visual observations it can be concluded that for  $Q_g = 9$  LPM, the flooding/loading transition occurs between  $225 < N_f < 250$  rpm, which is exactly the same as shown from the power measurement data. For the other flow rates of this study, the flooding/loading transition found by power measurements was confirmed visually and found to be in good comparison.

As the impeller speed increases, the transition to complete dispersion occurs at the local minimum labeled  $N_{cd}$  in Fig. 4.3 (Nienow et al., 1977). Complete dispersion corresponds to the point at which bubbles are dispersed throughout the tank, including the area below the impeller as indicated in Fig. 2.6d. For efficient operation, which corresponds to high gas holdup and high mass transfer rates, the impeller speed should be greater than or equal to  $N_{cd}$ ; this is a desirable impeller operating speed because bubbles are dispersed throughout the tank at the lowest possible power input. The progression from loading to complete dispersion for  $Q_g = 3$  LPM is shown in Fig. 4.5. When  $N = 275$  rpm (Fig. 4.5a; location (4) in Fig. 4.3), the region below the impeller has very few bubbles indicating  $N_{cd}$  has not yet been reached. When the impeller speed is increased to 300 rpm as shown in Fig.

4.5b (location (5) in Fig. 4.3), bubbles are present beneath the impeller, but not in all regions. After increasing the impeller speed to  $N = 325$  rpm (Fig. 4.5c; location (6) in Fig. 4.3), the bubbles are dispersed throughout the tank and complete dispersion has been reached. By visual observation, it can be concluded that  $N_{cd}$  occurs between  $300 < N_{cd} < 325$  rpm, which corresponds well with  $N_{cd} \approx 300$  rpm found by the power measurements (Fig. 4.3). For the other flow rates,  $N_{cd}$  determined by the power measurements was within 25 rpm of the visual determination of  $N_{cd}$ .

Further increases in impeller speed reveal another local maximum labeled  $N_r$  in Fig. 4.3. When the impeller has reached  $N_r$ , secondary circulation loops form and gross gas recirculation occurs (Nienow et al., 1977). The visual determination of  $N_r$  is extremely difficult and subjective and therefore was not done in this study.

For a STR operated at a constant gas flow rate, increasing the impeller speed causes smaller bubbles to form, which results in a larger interfacial area and promotes higher gas-liquid mass transfer rates. Conversely, decreasing the impeller speed causes larger bubbles to form resulting in a smaller interfacial area, suppressing gas-liquid mass transfer. These observations are shown in Fig. 4.6 for  $Q_g = 7$  LPM where the impeller speed increases from  $N = 400$  rpm (Fig. 4.6a) to  $N = 800$  rpm (Fig. 4.6c). The bubble size has a noticeable decrease and the number of bubbles has a significant increase over this range of impeller speeds while  $Q_g$  remains constant.

#### **4.1.2 Constant Impeller Speed**

Another common way of recording STR power measurements is to hold the impeller speed constant while varying the gas flow rate. Figure 4.7 shows the gassed to ungassed power demand ( $P_g/P_o$ ) plotted as a function of gas flow rate. As the gas flow rate increases,

the ratio  $P_g/P_o$  drops due to the increase in cavity size on the trailing edge of the impeller blades, which lowers the effective viscosity of the gas-liquid mixture. The minimum value of  $P_g/P_o$  for the ranges of this study is 0.4, which is similar to the 0.38 found by Kapic (2005) and with the expected range of  $0.3 \leq P_g/P_o \leq 0.5$  for a Rushton turbine (Chapman et al., 1983).

It is more common in the literature to see the gassed to ungassed power demand ( $P_g/P_o$ ) plotted as a function of the flow number  $Fl_g$  as shown in Fig. 4.8. In this figure, the gassed to ungassed power ratio drops as the gas flow rate increases because the flow number is proportional to  $Q_g$ . The curves are typically divided into two regions, an initial convex part at low gas flow rates and a concave part at high flow rates (Warmoeskerken and Smith, 1982). The inflection point on the diagram corresponds to the transition from 6 clinging cavities to the 3-3 structure of clinging and large cavities as described by Warmoeskerken et al. (1985).

## 4.2 Gas Holdup Measurements

CT scans were taken in the  $T = 0.21$  m STR filled with tap water to a height  $H = T$ . The chosen conditions are summarized in Table 4.1 and shown on the power measurement curve in Fig. 4.9. These conditions were selected to examine how time-averaged local gas holdup changes with operating regime. Section 4.2.1 provides a qualitative description of local gas holdup by presenting slices in all 3 axes. Section 4.2.2 provides a quantitative description of local and spatial-averaged gas holdup variations. Error quantification of the gas holdup measurements is then presented in section 4.2.3.

## 4.2.1 Qualitative Gas Holdup Results

The 3D visualization program described in Chap. 3 is a great tool to visually understand the gas holdup data. The program allows slices to be taken along all 3 major axes. The z-slice, which is the view seen from looking straight down onto the tank, provides great knowledge of how the local gas holdup varies radially and azimuthally. The x- and y-slices, which are the views taken from looking at the side of the tank, show the difference in vertical gas dispersion for different operating conditions.

### 4.2.1.1 z-Slice

Slices taken in the z-plane have the view shown in Fig. 4.10, which is looking down on the tank and in the same orientation as the reconstructed CT images (note the baffle location identifiers and the location of the air inlet that runs along the SW baffle). On closer inspection, the sparger does not completely wrap around the tank bottom due to manufacturing constraints (Fig. 4.10). The z-slices shown in this thesis correspond to heights of  $z = 0.8$  cm (slice 180),  $z = 3.0$  cm (slice 120), and  $z = 5.3$  cm (slice 60), where  $z = 0$  cm is the bottom of the impeller and corresponds to slice 200 in Fig. 3.1. Other locations between  $z = 0$  (slice 200) and  $z = 7.6$  cm (slice 0) could also be easily shown but the three selected show general trends. The slices could also be stacked together and viewed as a short video clip between  $z = 7.6$  cm and  $z = 0$ .

Figure 4.11 shows an enlarged image of a z-slice along with the gas holdup gray scale mapping. Even though the impeller shaft and hub are solid regions, these regions are not dark with 0% gas holdup, but it is extremely small in these regions. This is due to noise and image bleeding, which is common in X-rays. Therefore, for all images presented in this study, the impeller shaft and hub regions are forced to 0% gas holdup. The black circle in the center of

the  $z = 3.0$  and  $5.3$  cm images is the impeller shaft. For the  $z = 0.8$  cm image, the black circle in the center is the impeller hub. The impeller region (Fig. 4.11) has a larger diameter than the actual impeller, with the extent depending upon  $Q_g$  and  $N$ . The images are cropped so that the edge corresponds to the inner edge of the tank wall with ID = 21 cm. The lighter regions in the image represent higher gas concentrations. The white spot in the bottom left of all the images (SW baffle) is the air inlet (Fig. 4.11). The 4 black marks, which can be seen in the images taken while operating in the completely dispersed regime, are the 4 baffles located in the corners. For the rest of the images, the gas holdup mapping chart will be placed horizontal as shown on the bottom of Fig. 4.11. The impeller blades can be seen for the images with lower gas flow rates at  $z = 0.8$  cm and is an image artifact; the water-only reference scan taken to determine  $GS_I$  had a stationary impeller to prevent surface air entrainment as previously noted in section 3.4.4.2.

Figure 4.12 shows z-slices at 3 different heights for  $Q_g = 6$  LPM with  $N = 350$  and  $N = 700$  rpm. From the power measurements, it was determined that the  $N = 350$  rpm condition is in the loading regime and the  $N = 700$  rpm condition is in the completely dispersed regime (locations (1) and (2), respectively, in Fig. 4.9). The  $N = 350$  rpm slice at  $z = 5.3$  cm shows gas throughout most of the slice. The darker region in the center of the  $N = 350$  rpm slice  $z = 3.0$  cm is due to the gas passing around the impeller disk (to be discussed later). The  $N = 350$  rpm bottom slice at  $z = 0.8$  cm clearly shows that the tank is not in the completely dispersed regime due to the lack of gas away from the impeller region. There is a vast difference between the slices with  $N = 350$  rpm compared to  $N = 700$  rpm due to the change in flow regime where, at  $N = 700$  rpm, gas is dispersed almost uniformly throughout the entire slice. The  $N = 700$  rpm  $z = 0.8$  cm slice shows that the gas is dispersed away from the impeller and

in all tank regions, indicating the STR is operating in the completely dispersed regime whereas the  $N = 350$  rpm has dark regions representing very low or zero gas holdup away from the impeller. The baffles show up in the  $N = 700$  rpm  $z = 0.8$  cm slice as regions of low gas holdup. Again, the bright spot near the SW baffle in all  $z$ -slices is the air inlet hose.

STR flow regimes were compared by taking CT scans at 4 different impeller speeds while holding  $Q_g$  constant at 9 LPM (Fig. 4.13). As determined from the power consumption,  $N = 200$  (location (3) in Fig. 4.9) corresponds to the flooding regime which is clearly seen in the slice  $z = 0.8$  cm where very little gas is located outside the impeller region. As the vertical distance increases from the impeller ( $z = 3.0$  cm,  $z = 5.3$  cm), the central region of high gas holdup expands radially due to the decreased pressure head acting on the bubbles and the decreased bubble velocity which was also seen by Khopkar et al. (2005). As the bubbles spread out, there is an increase in drag which causes a lower bubble velocity thereby increasing the local gas holdup. When the impeller speed is increased to  $N = 350$  rpm (loading regime), the gas is dispersed slightly. In the slice  $z = 0.8$  cm, the gas is still located mainly around the impeller. The  $z = 3.0$  cm slice at  $N = 350$  rpm (location (4) in Fig. 4.9) has a distinct dark region of low gas holdup near the center and is the result of gas passing around the impeller hub and “thrown” radially outward.

Increasing the impeller speed to  $N = 525$  rpm (location (5) in Fig. 4.9), which is close to  $N_{cd}$  as determined by the power consumption curve, the slices show a different picture than the lower impeller speeds. Now, the gas is dispersed around the impeller region ( $z = 0.8$  cm slice), as characterized by the gray scale variation throughout the slice; this qualitatively shows the completely dispersed regime. Also, the nearly white region adjacent to the impeller hub has a very high gas content ( $\epsilon_g > 40\%$ ) due to the large amount of gas entrained

along the trailing edge of each impeller. Moving vertically up the STR ( $z = 3.0$  cm,  $5.3$  cm), the gas is uniformly dispersed with lower gas holdup regions extending from the trailing edges of the baffles. After the impeller speed is increased to  $N = 700$  rpm (location (6) in Fig. 4.9), which is clearly in the completely dispersed regime, the images look similar to  $N = 525$  rpm with a couple of differences. First, the images with  $N = 700$  rpm show higher gas holdups than the  $N = 525$  rpm images. Second, recirculation cells are clearly visible in the lower 2 slices on the trailing edges of the NE and SE baffles. The recirculation zones are only appearing on the right side of the image due to the asymmetric gas entry caused by the sparger (Fig. 4.10).

Figure 4.14 shows slices taken at  $Q_g = 12$  LPM with  $N = 325$  and  $700$  rpm corresponding to locations (7) and (8) in Fig. 4.9, respectively. The slices with  $N = 325$  rpm are clearly in the loading regime as determined by the power measurements and slice  $z = 0.8$ . Slice  $z = 3.0$  cm has a darker region in the center with a ring of higher gas holdup due to the gas being radially expelled from the edges of the impeller. When the impeller speed is increased to  $N = 700$  rpm, the tank is now in the completely dispersed regime as gas is distributed throughout the STR by the impeller. Recirculation regions are found by the trailing edges of the NE and SE baffles for all 3 slices. In the  $z = 0.8$  cm slice at  $N = 700$  rpm, a recirculation region is also starting to develop at the trailing edge of the NW baffle.

#### **4.2.1.2 x- and y-Slice**

Slices taken in the x- and y-plane provide a view of how gas holdup varies vertically. The x-slice is the view obtained from standing on the right of Fig. 4.10 and looking towards the tank. The y-slice view corresponds to standing below the picture and looking up towards

the tank. In each case the x- and y-slices shown here go directly through the STR center, although other locations could be viewed.

Figure 4.15 shows the x-slice for  $Q_g = 6$  LPM with impeller speeds of  $N = 350$  rpm and  $N = 700$  rpm (locations (1) and (2) in Fig. 4.9, respectively). The  $N = 350$  image clearly shows the STR operating in the loading region with very little gas near the bottom outside of the impeller region. High regions of gas holdup are observed emanating from the impeller tips; this was previously shown in the  $z = 3.0$  cm slice. When  $N$  is increased to 700 rpm, the gas is distributed throughout the tank.

Figure 4.16 shows an x- and y-slice for  $Q_g = 9$  LPM and  $N = 200$  rpm (location (3) in Fig. 4.9). The STR has an axial flow of gas through the impeller plane up to the free liquid surface, which is defined by Warmoeskerken and Smith (1985) as flooding. For both images, there is very little gas near the impeller region. The images look very similar, except that the right side of the y-slice has a slightly higher gas holdup than the x-slice. This is due to the design of the sparger (Fig. 4.10), which releases most of the gas between the NE and SE baffle.

With  $Q_g$  held constant at 9 LPM, increasing the impeller speed to 350 rpm causes the STR to enter the loading regime (Fig. 4.17; location (4) in Fig. 4.9). The start of the impeller dispersing the gas results in higher gas holdups near the impeller tips. Due to the start of the impeller dispersing the gas, there is a region of low gas holdup directly above the impeller hub. Upon increasing the impeller speed to  $N = 525$  rpm which is close to  $N_{cd}$ , the STR is operating in the completely dispersed regime (location (5) in Fig. 4.9). Gas is uniformly distributed throughout the imaging region. Higher gas holdups are still located near the impeller tips.

Upon further increases in impeller speed to  $N = 700$  rpm, the tank continues to operate in the complete dispersion regime with higher local gas holdup (Fig. 4.18; location (6) in Fig. 4.9). The x- and y-slice again look very similar with a few minor differences due to the sparger design. In the top right corner of the x-slice, there is a region of lower gas holdup which is not seen in the y-slice. Also, the top left corner of the x-slice has a slightly higher local gas holdup than the y-slice. The small differences noted above were common for all the images due to the unequal gas entrance caused by the manufacturing constraints on the sparger design required to reduce CT artifacts.

Figure 4.19 shows an x-slice for  $Q_g = 12$  LPM with  $N = 325$  and  $N = 700$  rpm (locations (7) and (8) in Fig. 4.9). For the  $N = 325$  rpm slice, the tank is loaded with high gas holdup off the impeller tip and low gas holdup at the bottom outside the impeller region. At  $N = 700$  rpm, the flow is completely dispersed and the images look similar to those for  $Q_g = 9$  LPM with  $N = 700$  rpm due to identical flow regimes.

#### 4.2.2 Quantitative Gas Holdup Results

Using a modified version of the gas holdup program, gas holdup values along the x-axis are plotted for  $Q_g = 9$  LPM with impeller speeds  $N = 200$  rpm (flooded),  $N = 350$  rpm (loaded), and  $N = 700$  rpm (completely dispersed). For all plots, the negative distance corresponds to the southern portion of the tank (Fig. 4.10). Figure 4.20 shows the local gas holdup values at  $z = 0.8$  cm. The impeller hub is solid since the gas holdup there should be 0. For all 3 impeller speeds, the gas holdup rises dramatically in the impeller region due to the presence of cavities behind the stirrer blades (Van't Riet and Smith, 1975). A maximum time-averaged gas holdup in this region is less than 55% for these conditions. For  $N = 700$  rpm (completely dispersed), the holdup is higher outside the impeller region than the other

two impeller speeds. For the other two impeller speeds, the impeller is not able to disperse the gas effectively, resulting in low gas holdups outside the impeller region.

Figure 4.21 is a plot of the same three conditions at height  $z = 3.0$  cm. There is some noise in the data due to the beam hardening correction, but the overall trends are clearly seen. The completely dispersed regime ( $N = 700$  rpm) has a fairly uniform gas holdup which is, on average, higher than the other two impeller speeds. The flooded regime ( $N = 200$  rpm) has high local gas holdup along the impeller shaft and a parabolic shape due to the bubble column type flow characteristic of flooding. The loaded regime ( $N = 350$  rpm) has very low local gas holdup near the impeller shaft caused by the impeller dispersing the gas off the blade tips. The low gas holdup in the center for the  $N = 350$  rpm can be seen in the  $z$ -slice (Fig. 4.13) and  $x$ -slice (Fig. 4.17) figure.

Figure 4.22 shows the local gas holdup values at a height  $z = 5.3$  cm. The flooded regime ( $N = 200$  rpm) again shows a parabolic shape with high local gas holdups along the impeller shaft. The completely dispersed regime ( $N = 700$  rpm) has a fairly uniform local gas holdup values which are higher than the loading regime ( $N = 350$  rpm).

A computer program was written to average all the local gas holdup values in a  $z$ -slice. It should be noted that the holdup values for a slice were determined by summing all the values in the slice including solid regions. Since the total imaging volume is  $2620 \text{ cm}^3$  with only  $65 \text{ cm}^3$  being solid, an error less than 2.5% is introduced. Figure 4.23 shows the slice holdup for the 4 different impeller speeds chosen for  $Q_g = 9$  LPM. The flooded condition ( $N = 200$  rpm) has a completely different trend than the other 3 conditions. Instead of gas holdup decreasing with increasing height, the gas holdup increases with height. Because the impeller has very little effect dispersing the gas, the decrease in pressure head

with height has a big effect on the flooded regime. The decrease in pressure causes the bubbles to increase in size thereby increasing gas holdup. Also, as the bubbles expand and spread out, there is an increase in drag causing the bubble velocity to decrease which leads to higher gas holdup. For the other 3 conditions, the gas holdup decreases with height and has a parabolic shape in the impeller zone. The parabolic shape in the impeller zone is due to the impeller capturing the gas (Van't Riet and Smith, 1975). Another trend can be seen from the graph when excluding the flooded condition, the gas holdup increases with increasing impeller speed at all heights above the impeller zone.

Figure 4.24 shows the average slice holdup for a constant impeller speed of  $N = 700$  rpm for 3 gas flow rates. From the power measurements, it is determined that all 3 conditions are in the completely dispersed regime. As the gas flow rate increases, the gas holdup tends to increase. It is speculated that recirculation may be occurring at the higher heights for  $Q_g = 9$  LPM leading to the gas holdup being slightly higher than  $Q_g = 12$  LPM. The parabolic trend in the impeller region is again seen as was the case for most of the conditions in Fig. 4.23.

By averaging the slice-average holdup values, an overall gas holdup for the imaging region is obtained. The values for overall gas holdup obtained using CT values and the visual technique (Saravanan and Joshi, 1996; Yalwalkar et al., 2001) are presented in Table 4.2. As the impeller speed increases while holding  $Q_g$  constant, gas holdup increases, which has also been recorded by many authors (Yalwalkar et al., 2001; Thatte et al., 2004). The CT gas holdup is highest for the condition  $Q_g = 12$  LPM and  $N = 700$  rpm. The values of CT and global gas holdup differ slightly. This is because the CT holdup only takes into account the imaging region, which typically has more gas than the rest of the tank.

### 4.2.3 Error Quantification

Three CT scans were taken at  $Q_g = 9$  LPM and  $N = 700$  rpm to determine the repeatability of the results. For the 3 scans, CT overall gas holdup had a standard error value of  $0.4 \epsilon_g$  with percent standard error of 6.5%. To determine how accurate the gas holdup measurements are, a 7.2 cm ID empty nalgene bottle was placed in the tank filled with water, which gives a holdup of 11.0 % in the imaging region. One problem introduced by doing this test is the bleeding of a high intensity region into nearby regions (Ketcham and Carlson, 2001). This problem was solved by setting gas holdup values lower than 10% to 0. The CT determined value for holdup is 11.8%, which agrees closely to the calculated value.

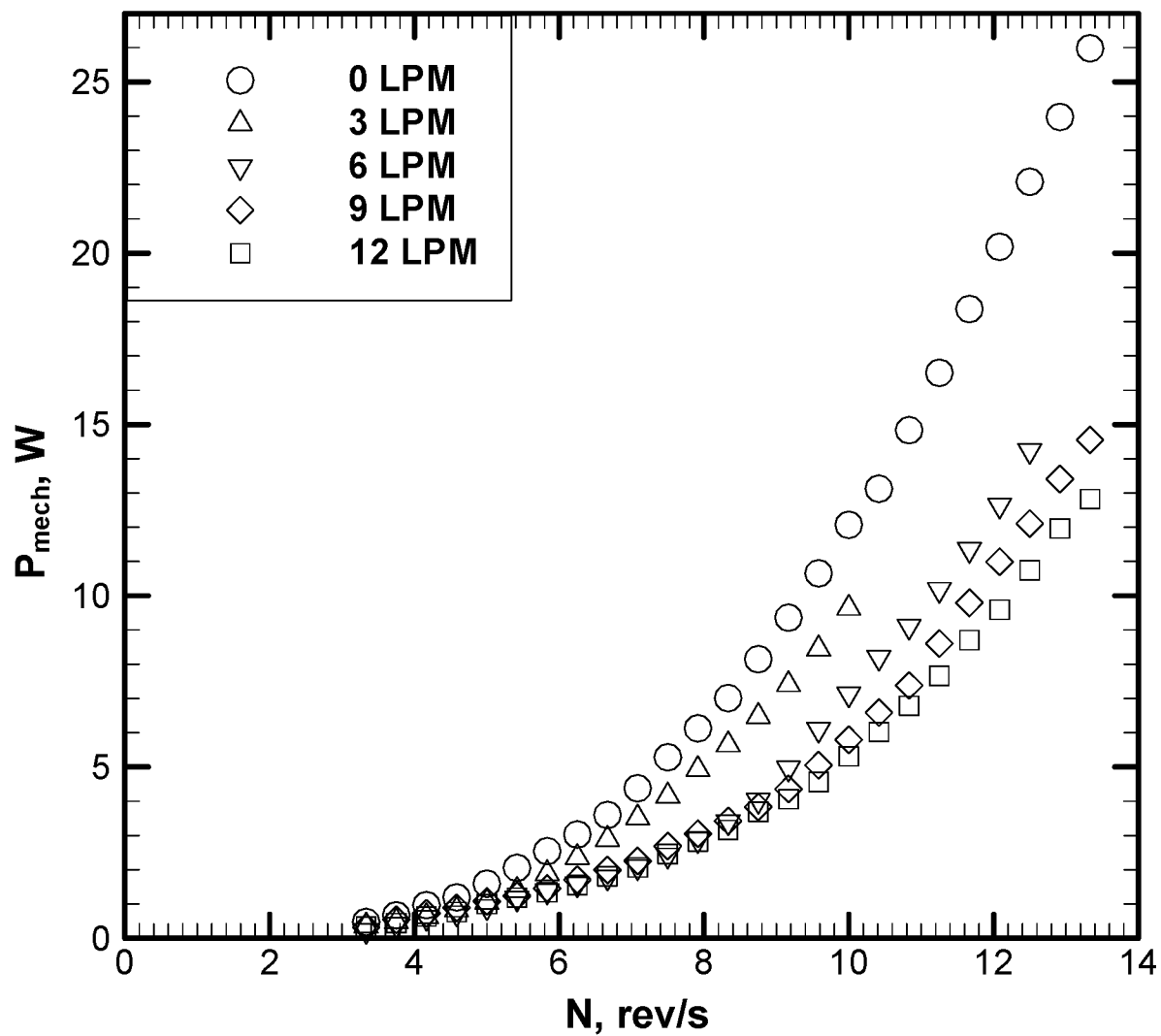
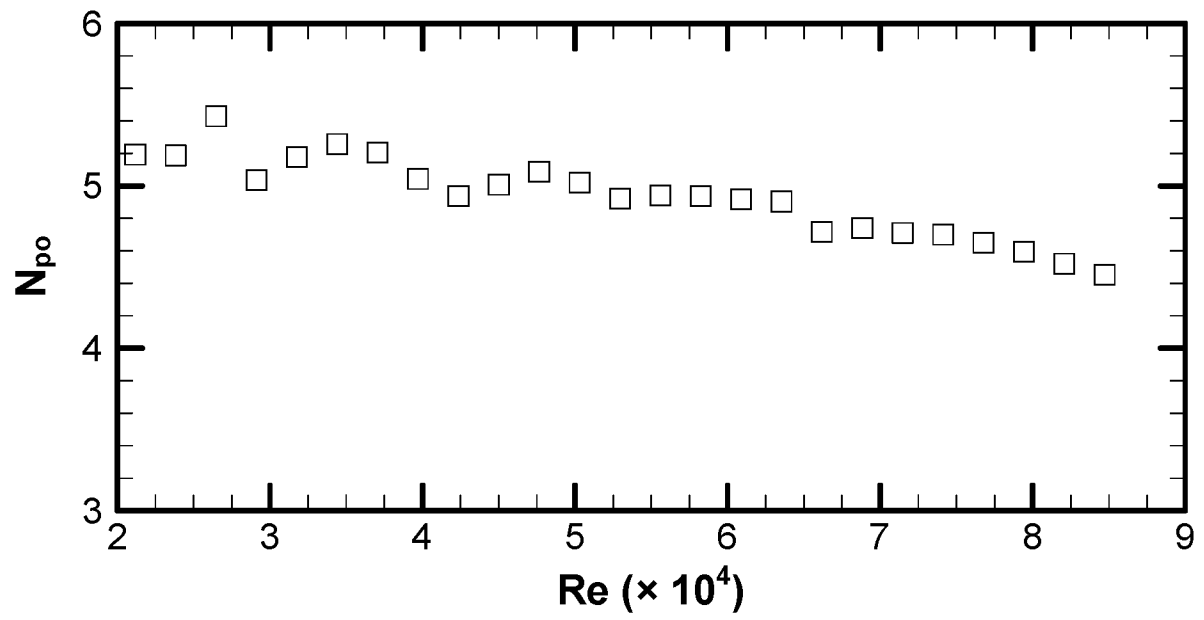


Figure 4.1: Mechanical power as a function of impeller speed.



**Figure 4.2:** Ungassed power number vs. Reynolds number.

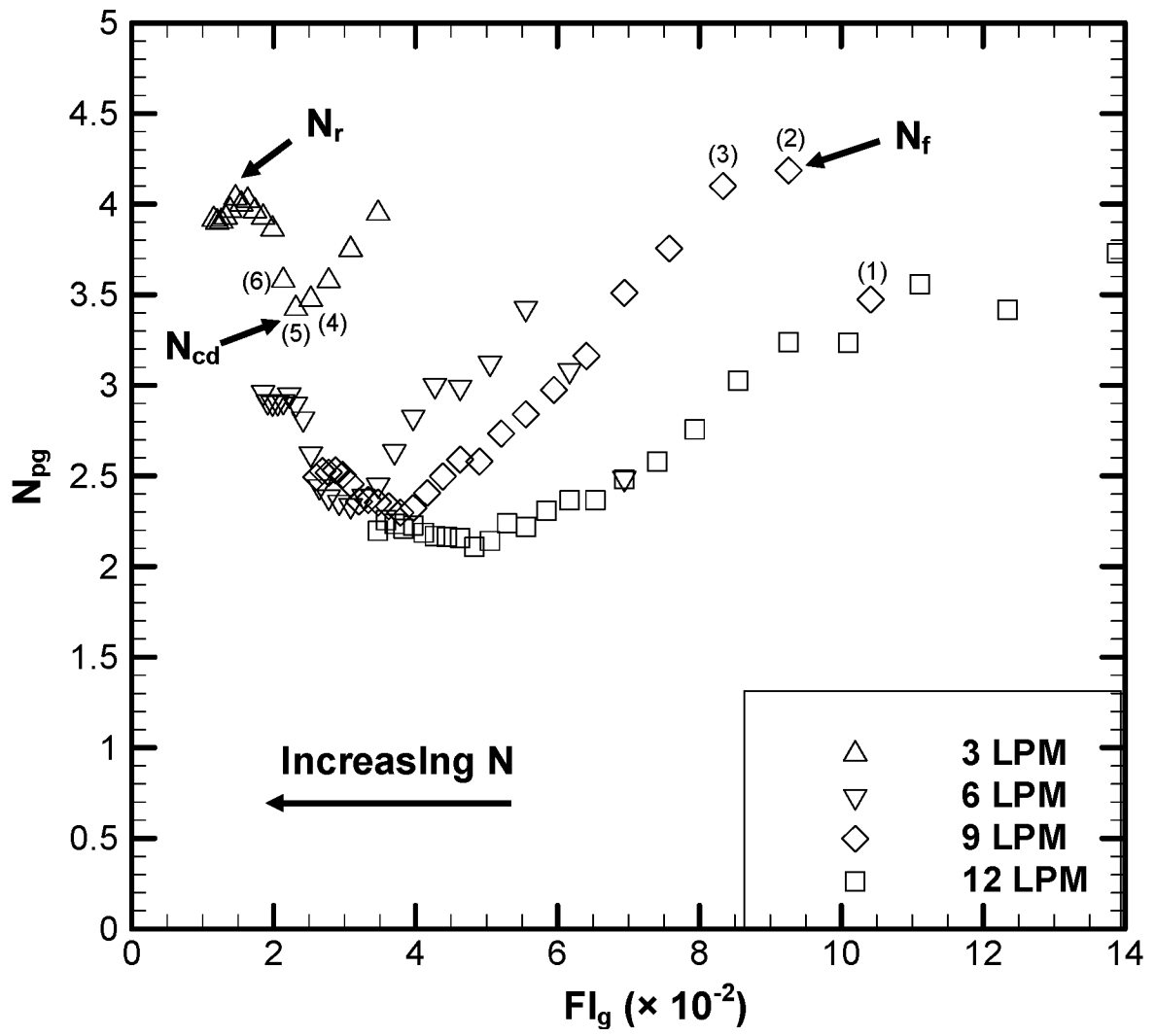
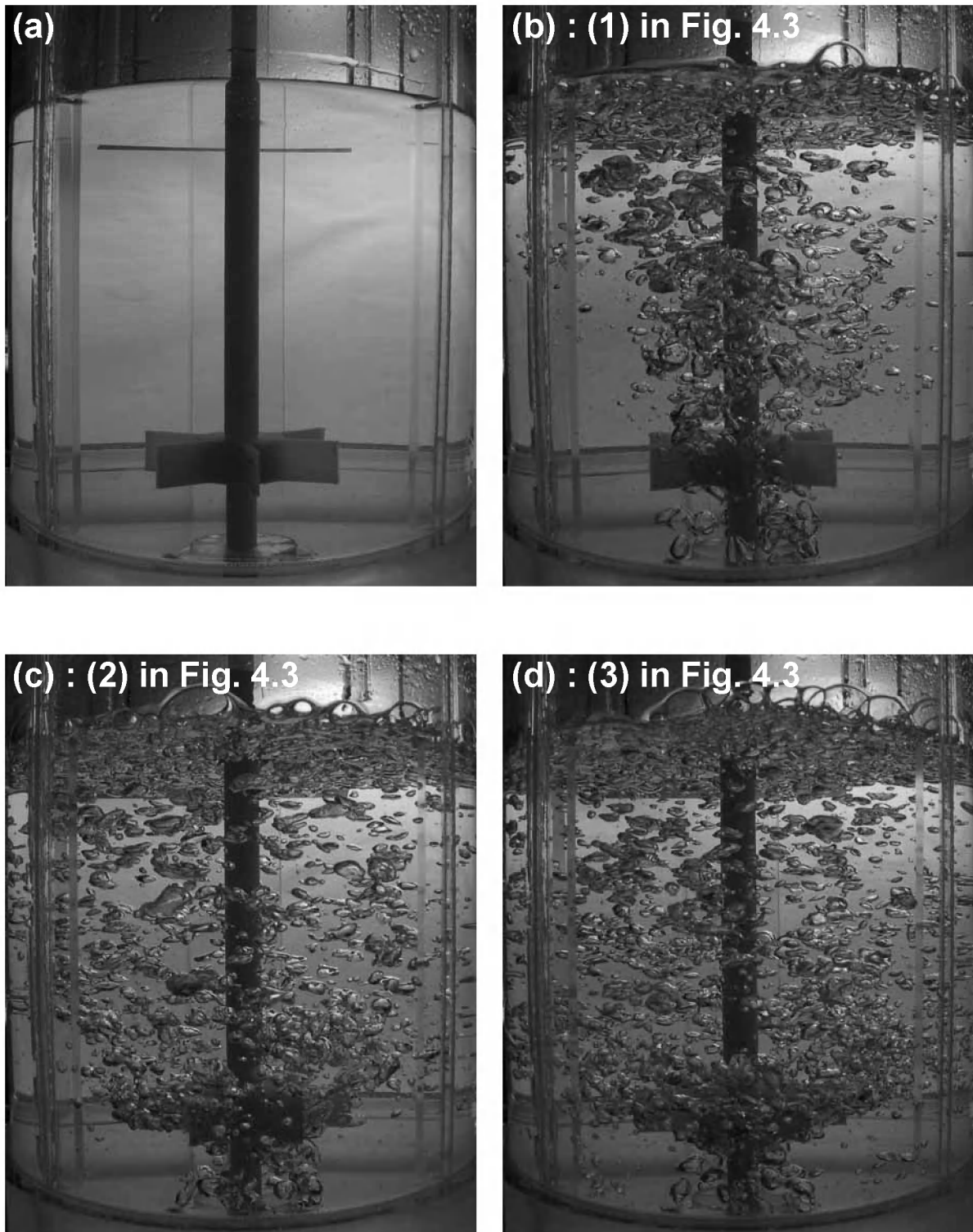
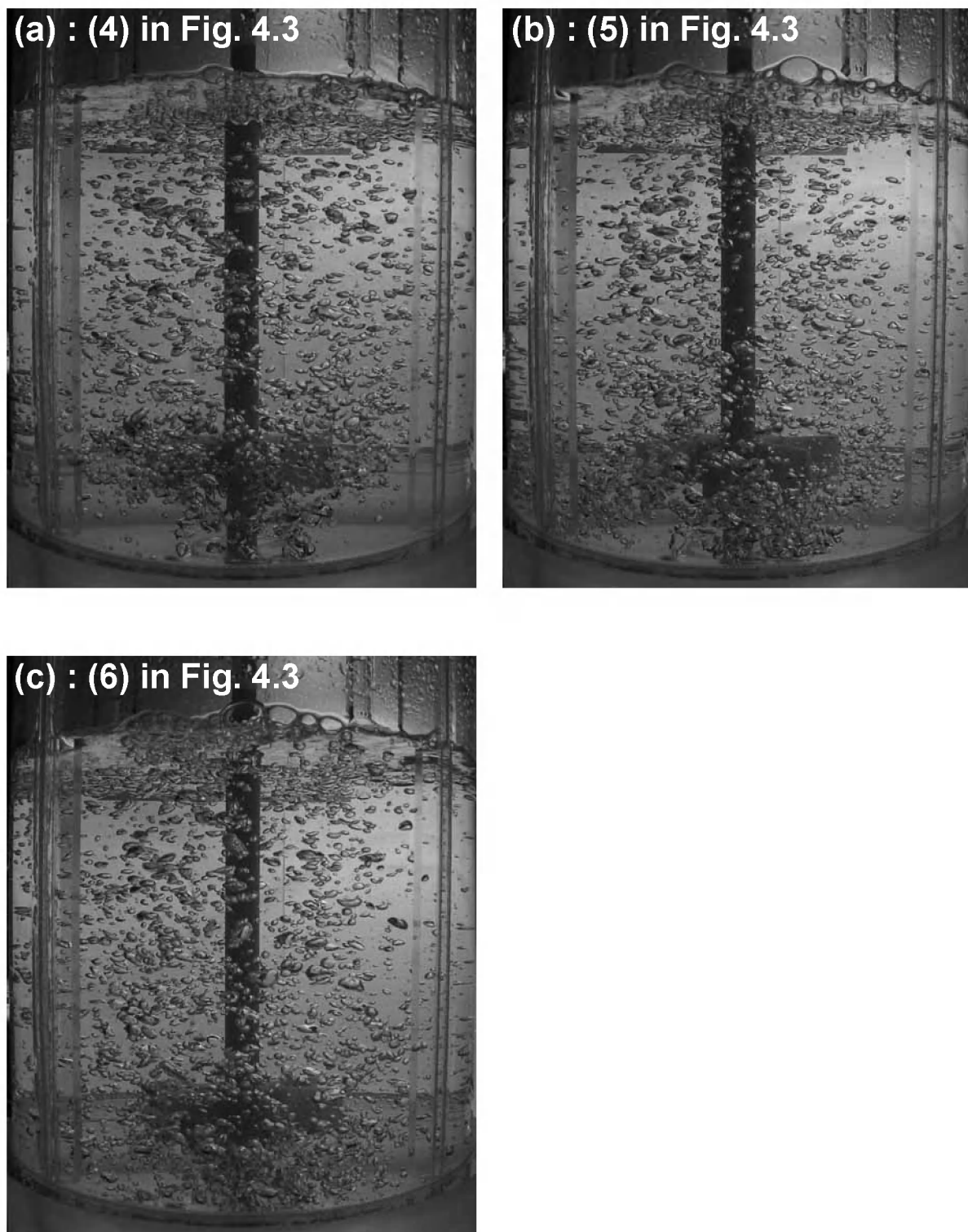


Figure 4.3: Gassed power number vs. flow number at constant  $Q_g$ .



**Figure 4.4:** Flooding/loading progression for  $Q_g = 9$  LPM; (a)  $N = 0$ ,  $Q_g = 0$ , (b)  $N = 200$  rpm, (c)  $N = 225$  rpm, and (d)  $N = 250$  rpm.



**Figure 4.5:** Loading/complete dispersion progression for  $Q_g = 3$  LPM; (a)  $N = 275$  rpm, (b)  $N = 300$  rpm, and (c)  $N = 325$  rpm.

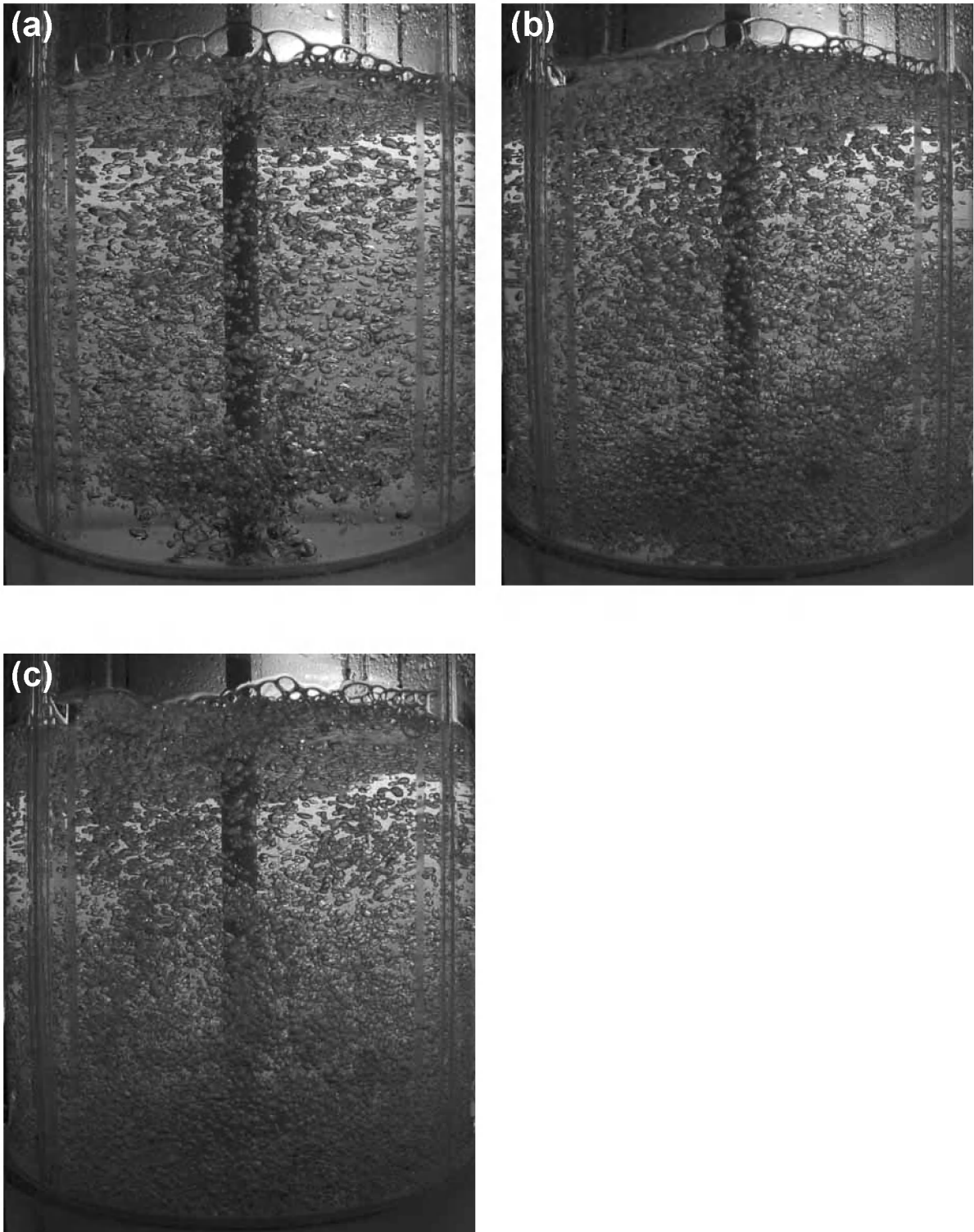


**Figure 4.6:** Bubble size decreasing at constant  $Q_g = 7$  LPM; (a)  $N = 400$  rpm, (b)  $N = 600$  rpm, and (c)  $N = 800$  rpm.

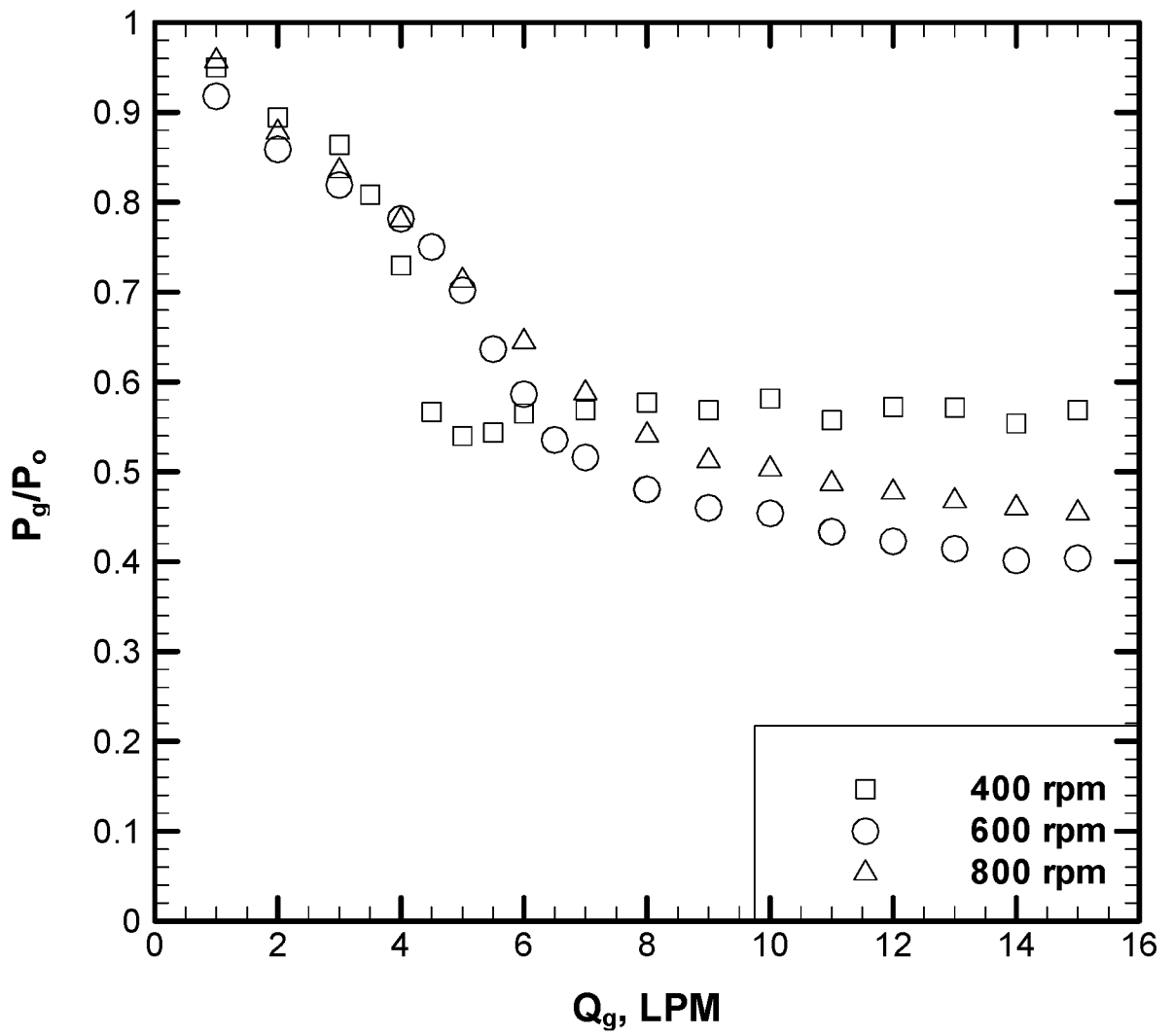


Figure 4.7: Gassed to ungassed power vs.  $Q_g$  at constant N.

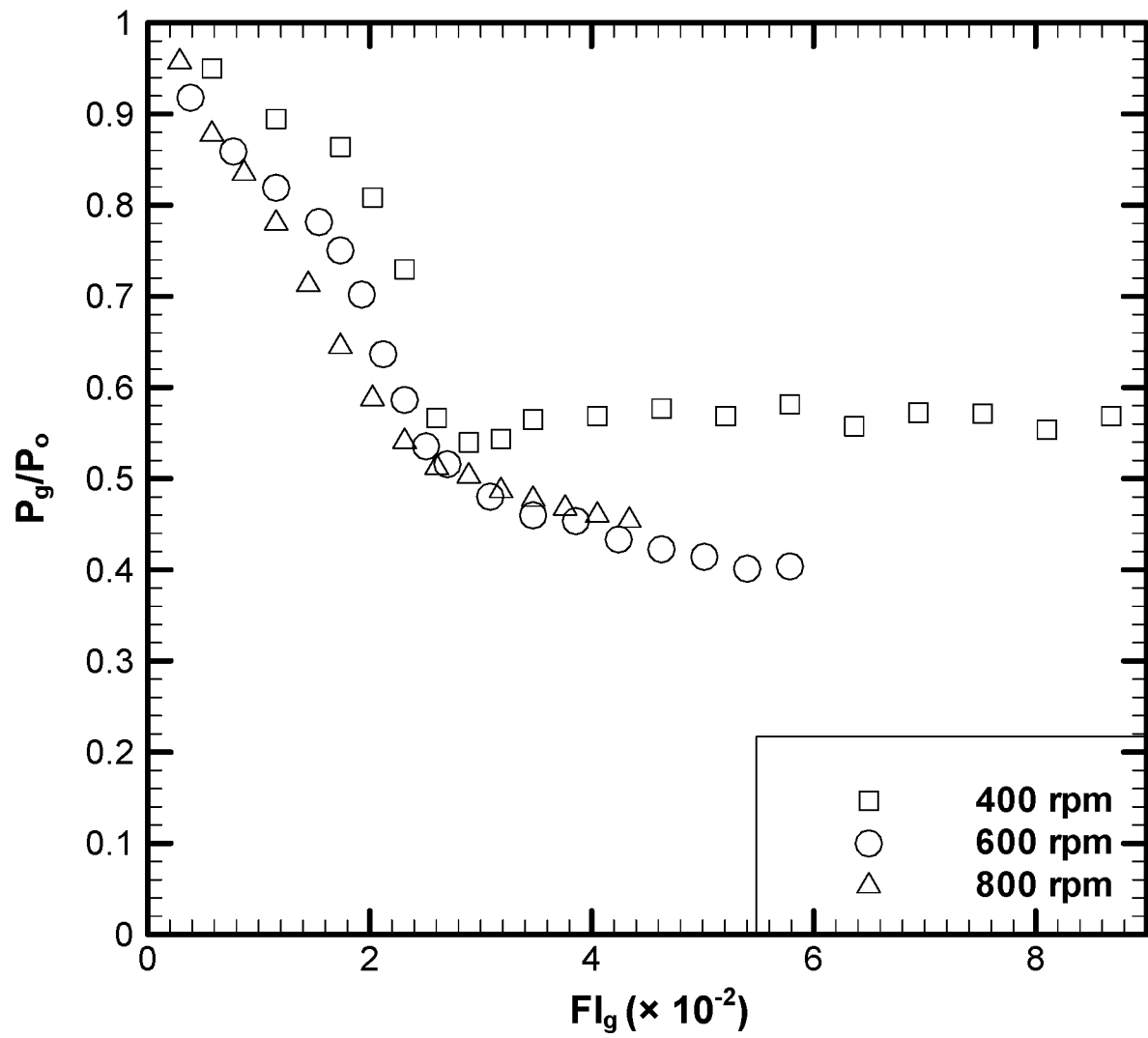
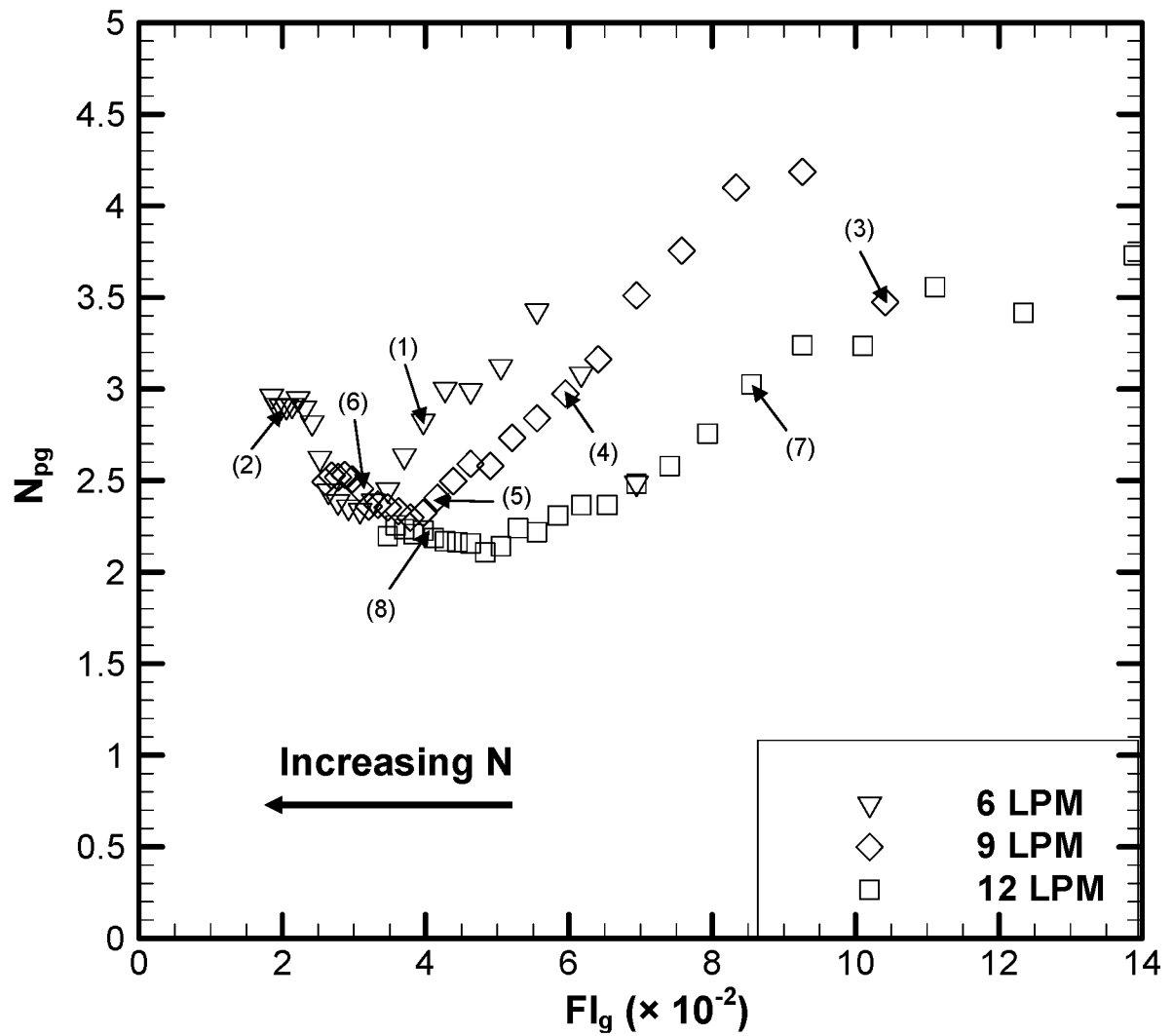
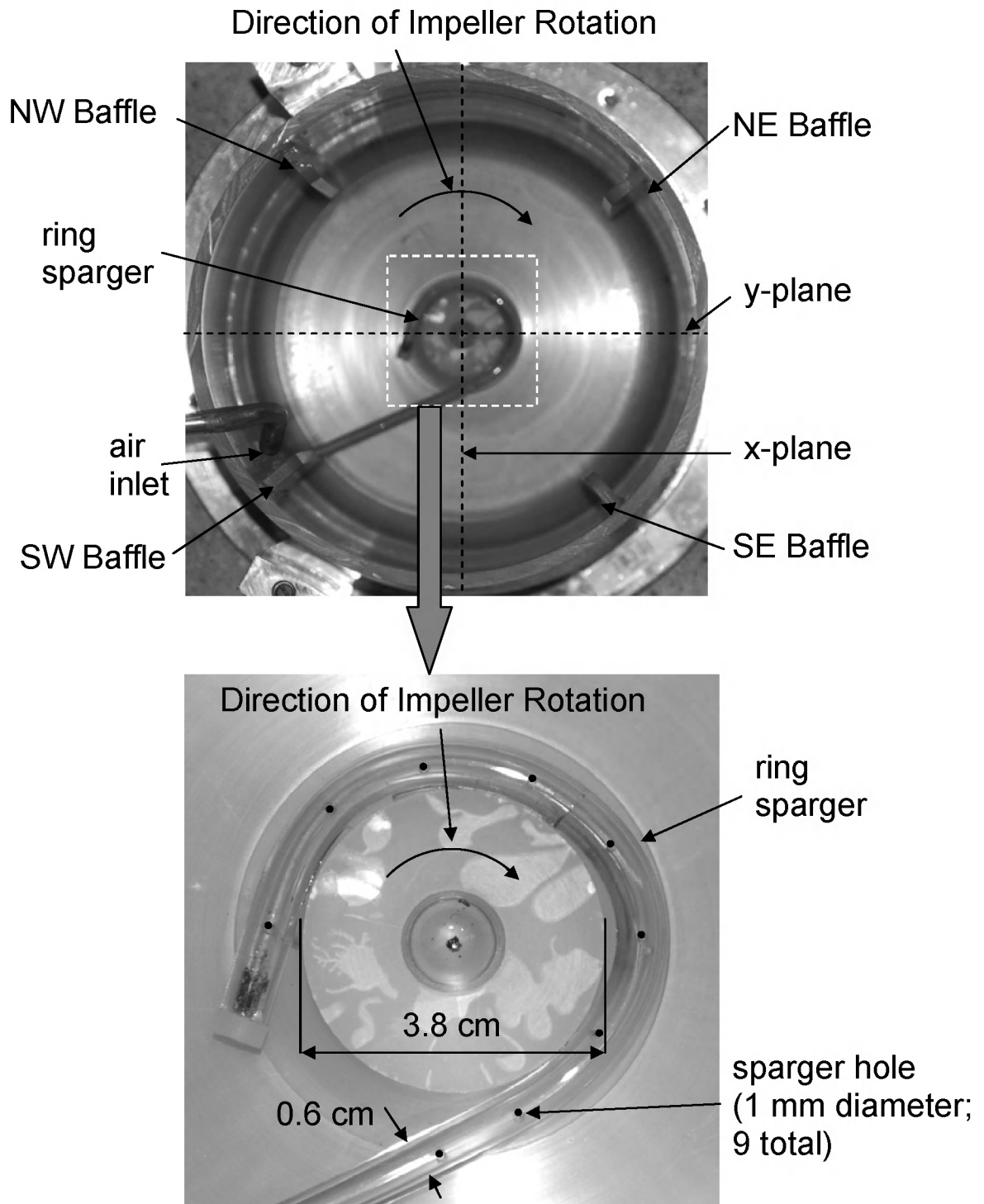


Figure 4.8: Gassed to ungassed power vs. flow number at constant N.



**Figure 4.9:** Gassed power number vs. flow number at constant  $Q_g$  with CT scan conditions labeled.



**Figure 4.10:** STR bottom and ring sparger.

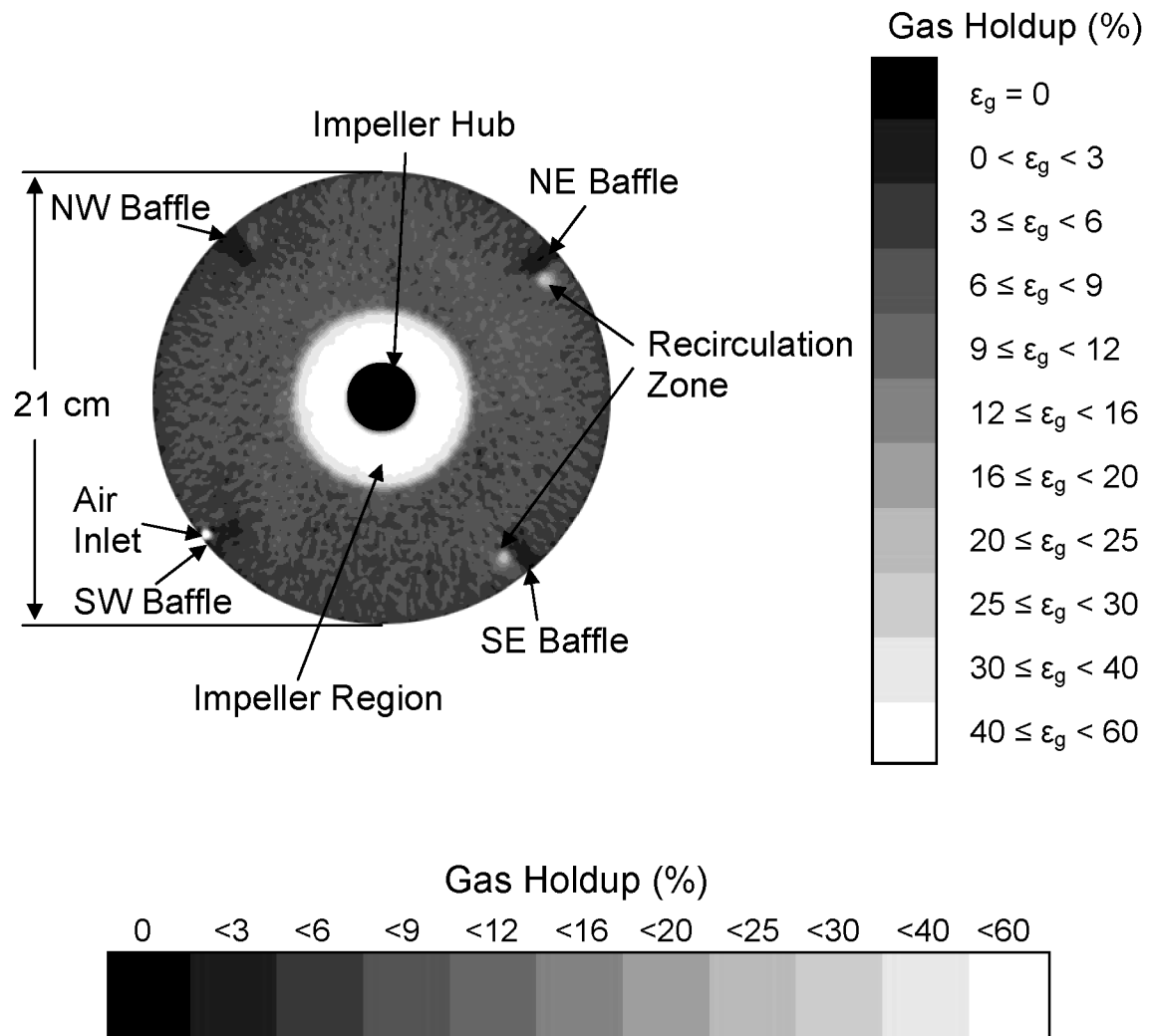


**Figure 4.11:** A sample z-slice with gas holdup mapping diagram ( $z = 0.8$  cm).

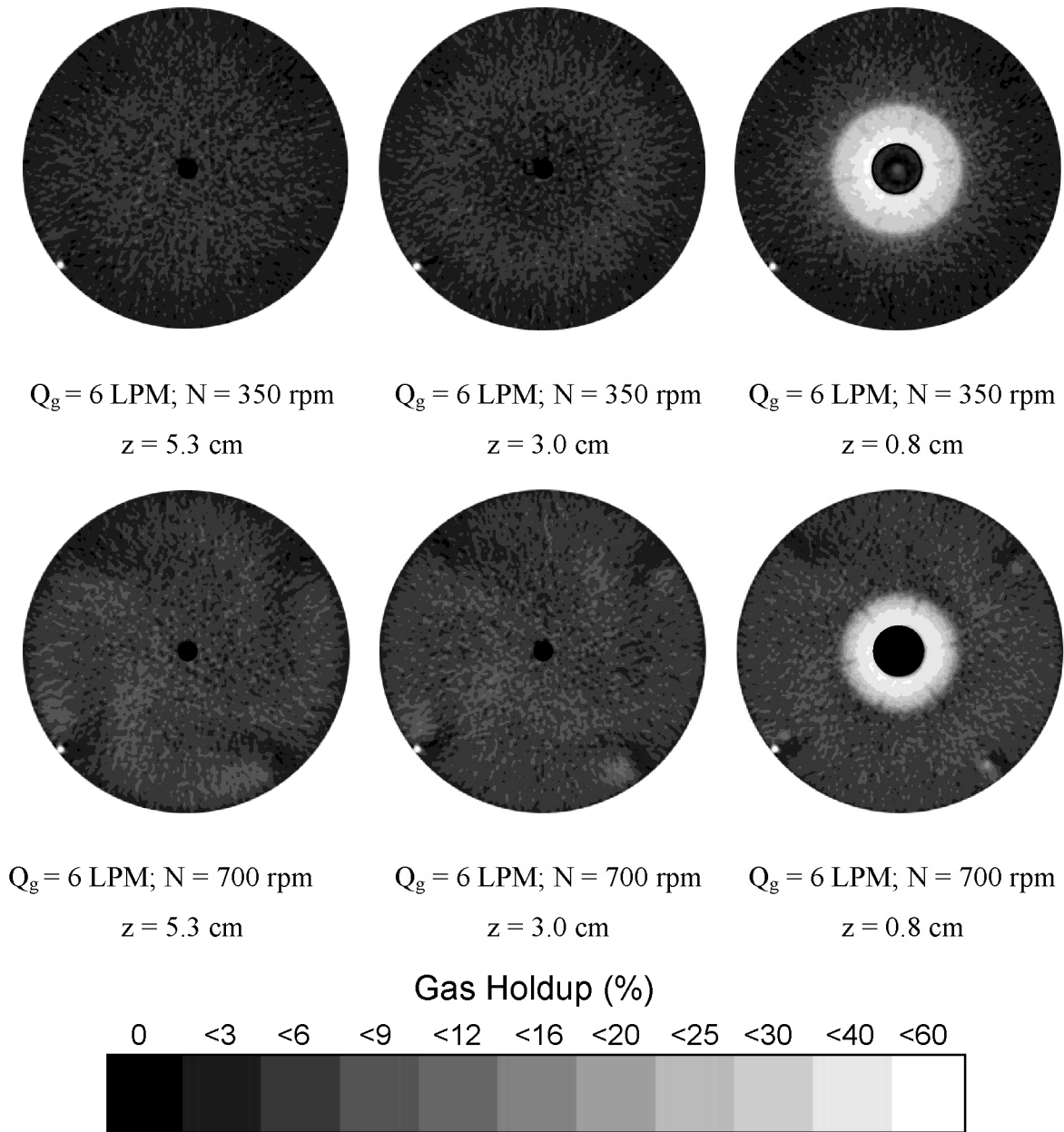


**Figure 4.12:** Slices taken at 3 different heights for  $Q_g = 6 \text{ LPM}$ .

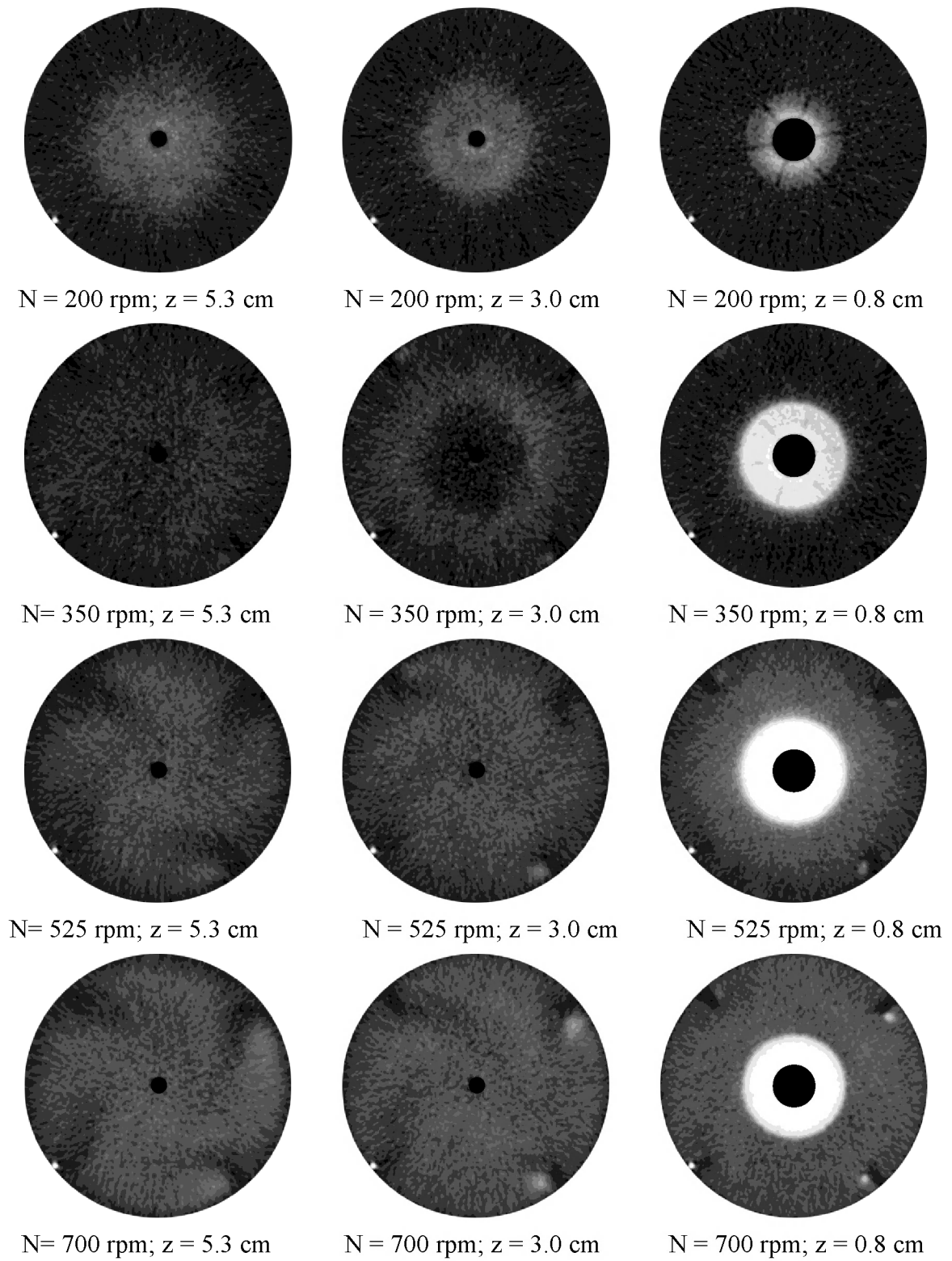


**Figure 4.13:** Slices taken at 3 different heights for various impeller speeds with  $Q_g = 9$  LPM.

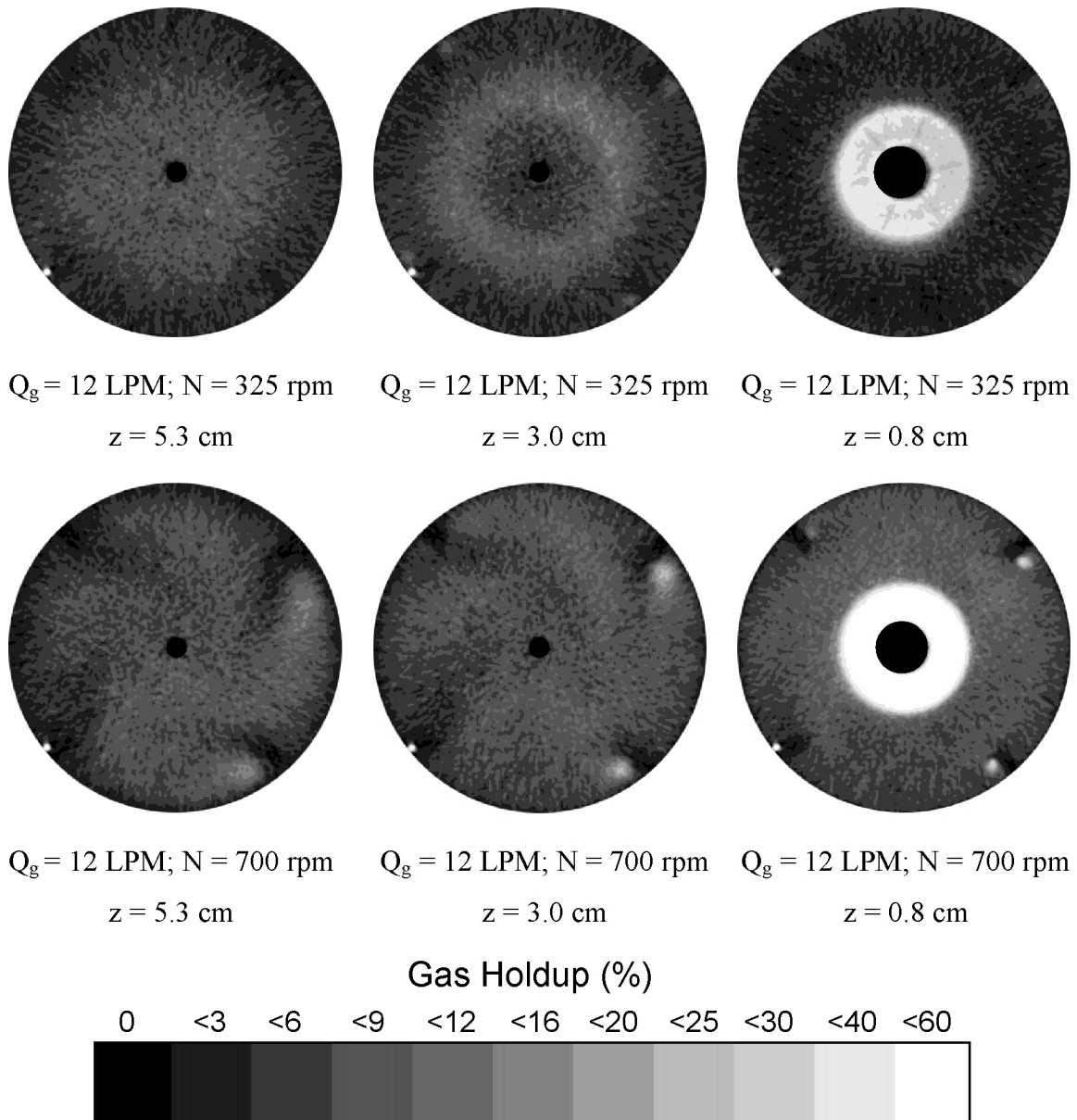
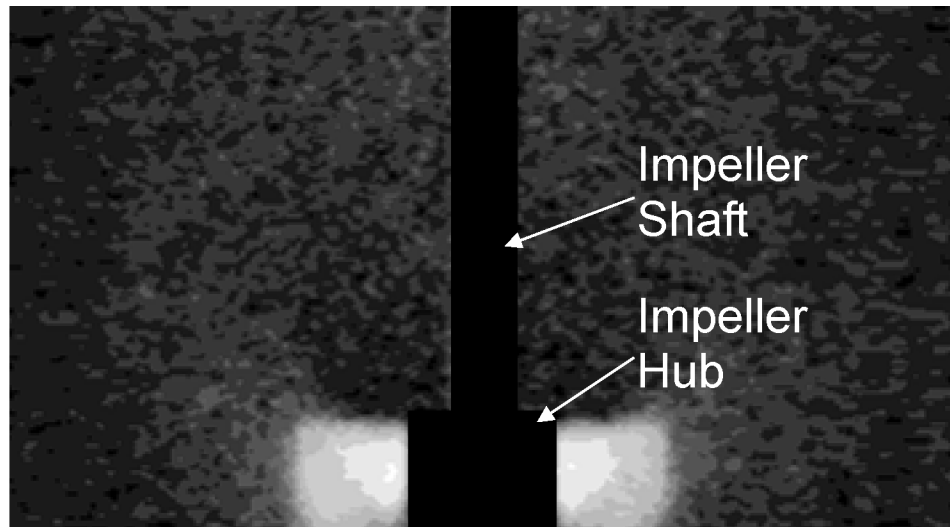
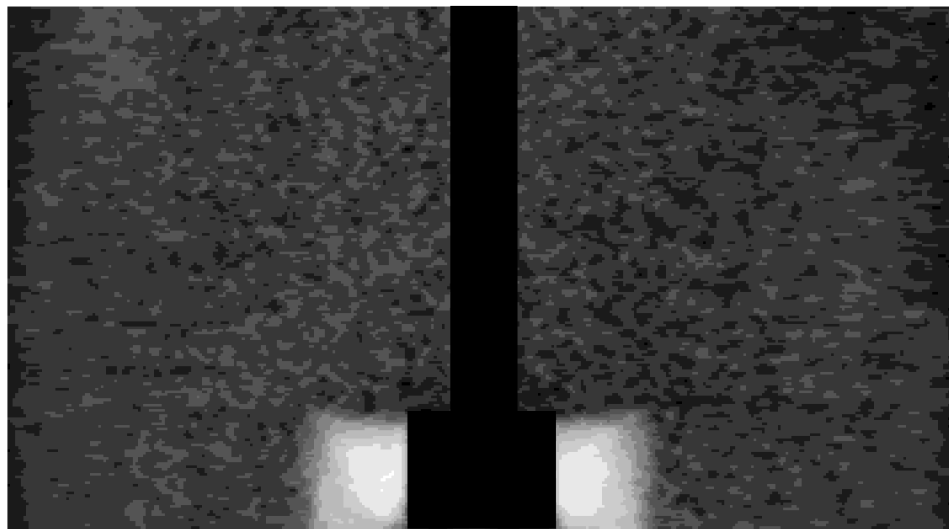


**Figure 4.14:** Slices taken at 3 different heights for  $Q_g = 12$  LPM.



(a)  $Q_g = 6$  LPM;  $N = 350$  rpm; x-Slice



(b)  $Q_g = 6$  LPM;  $N = 700$  rpm; x-Slice

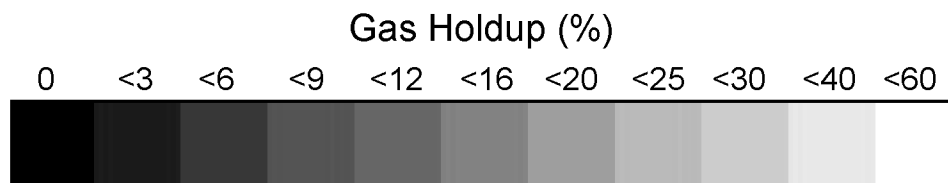
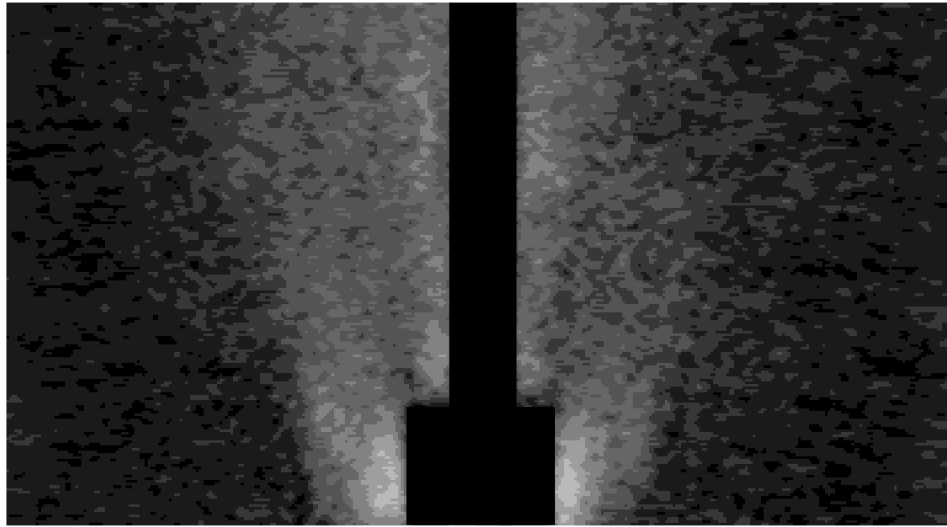
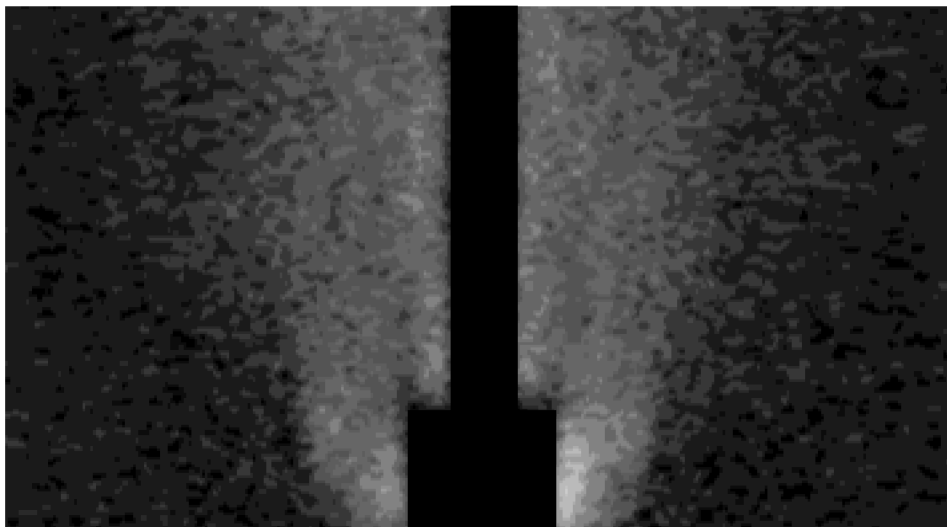


**Figure 4.15:** CT x-slices for (a) loaded ( $N = 350$  rpm) and (b) completely dispersed ( $N = 700$  rpm) for  $Q_g = 6$  LPM.



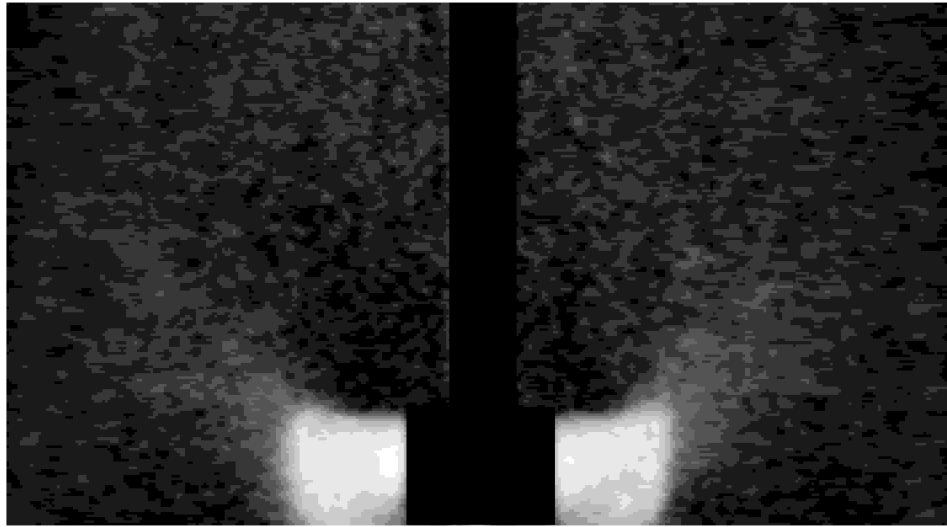
(a)  $Q_g = 9$  LPM;  $N = 200$  rpm; x-Slice



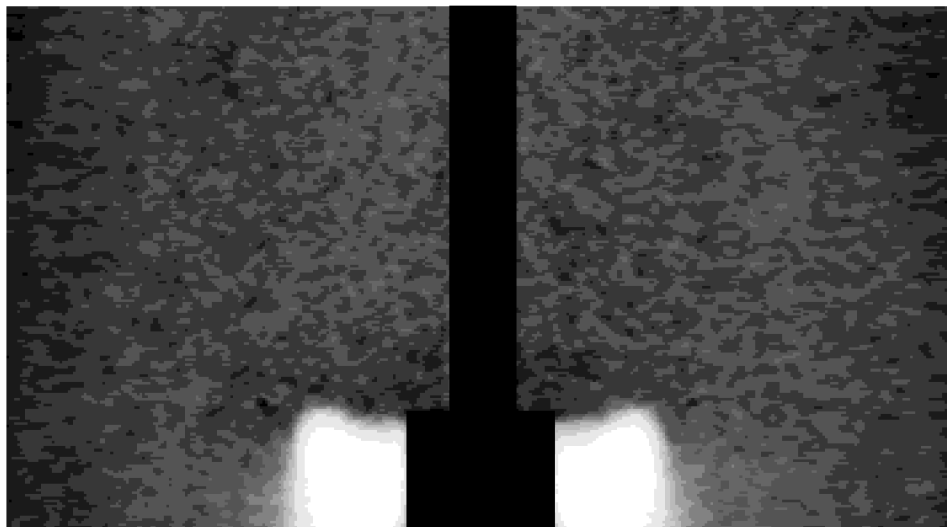
(b)  $Q_g = 9$  LPM;  $N = 200$  rpm; y-Slice



**Figure 4.16:** Flooded at  $Q_g = 9$  LPM and  $N = 200$  rpm for (a) x- and (b) y-slice.



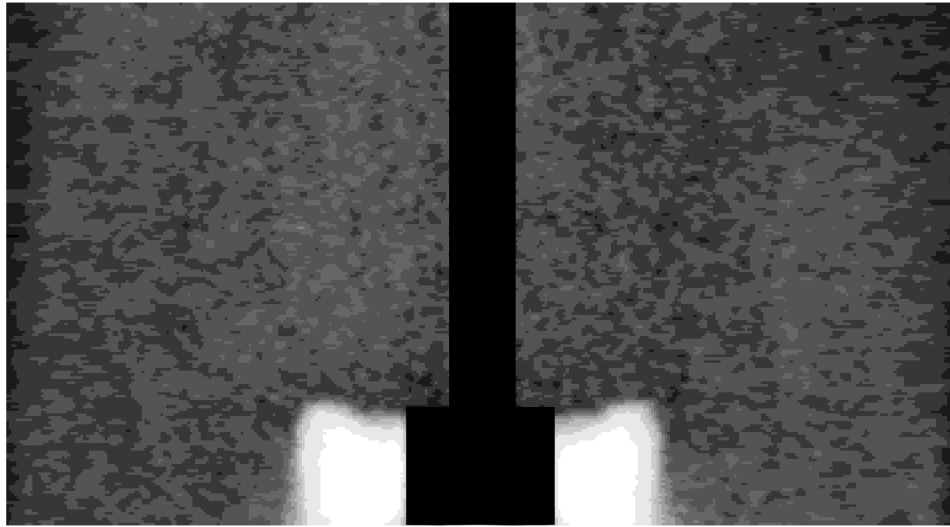
(a)  $Q_g = 9$  LPM;  $N = 350$  rpm; x-Slice



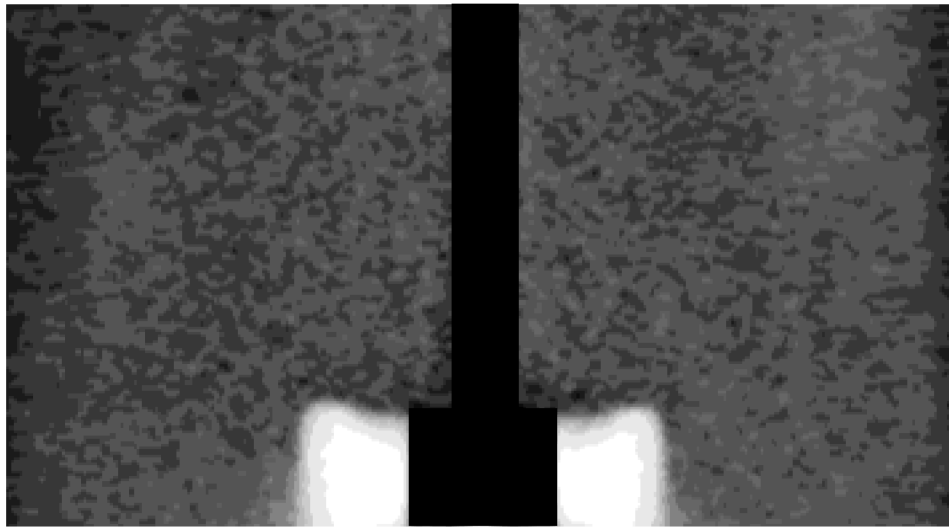
(b)  $Q_g = 9$  LPM;  $N = 525$  rpm; x-Slice



**Figure 4.17:** CT x-slices for (a) loaded ( $N = 350$  rpm) and (b) completely dispersed ( $N = 700$  rpm) for  $Q_g = 9$  LPM.



(a)  $Q_g = 9$  LPM;  $N = 700$  rpm; x-Slice



(b)  $Q_g = 9$  LPM;  $N = 700$  rpm; y-Slice

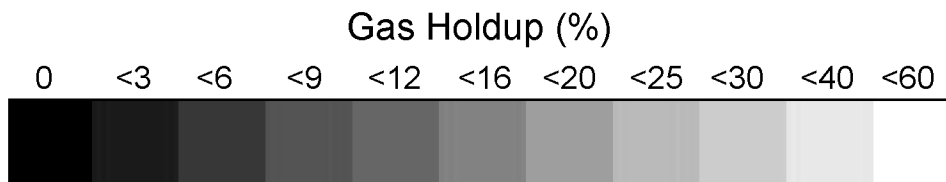
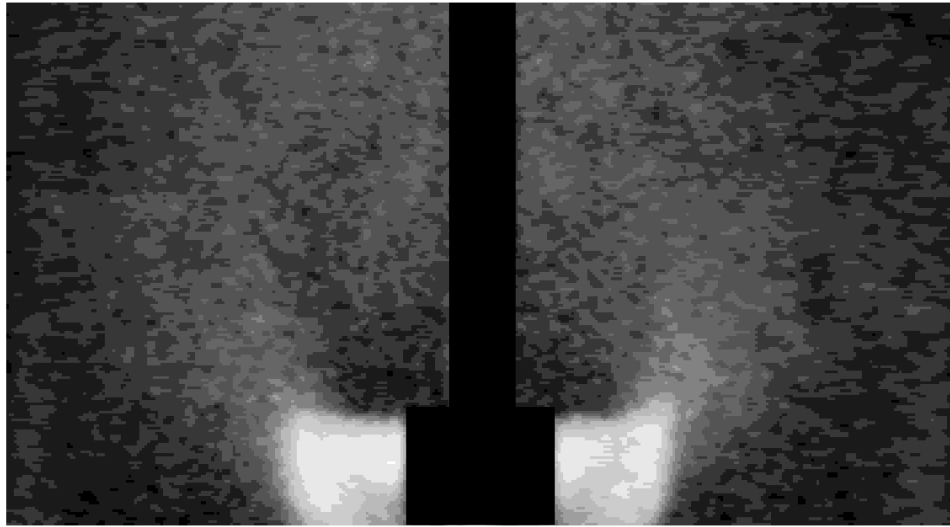
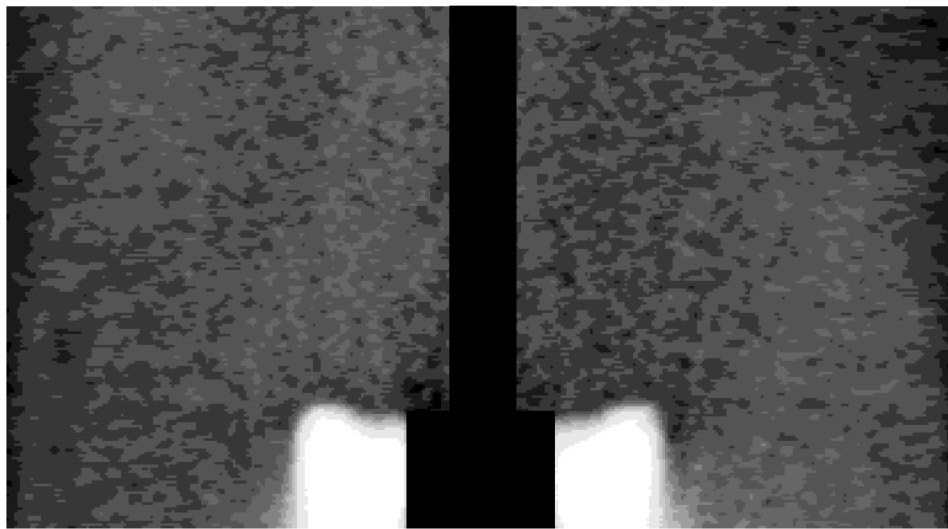


**Figure 4.18:** Completely dispersed at  $Q_g = 9$  LPM and  $N = 700$  rpm for (a) x- and (b) y-slice.



(a)  $Q_g = 12$  LPM;  $N = 325$  rpm; x-Slice



(b)  $Q_g = 12$  LPM;  $N = 700$  rpm; x-Slice

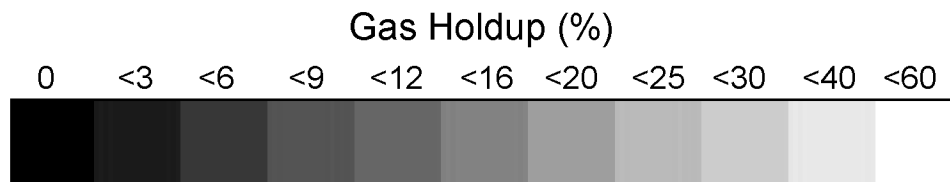


**Figure 4.19:** CT x-slices for (a) loaded ( $N = 325$  rpm) and (b) completely dispersed ( $N = 700$  rpm) for  $Q_g = 12$  LPM.

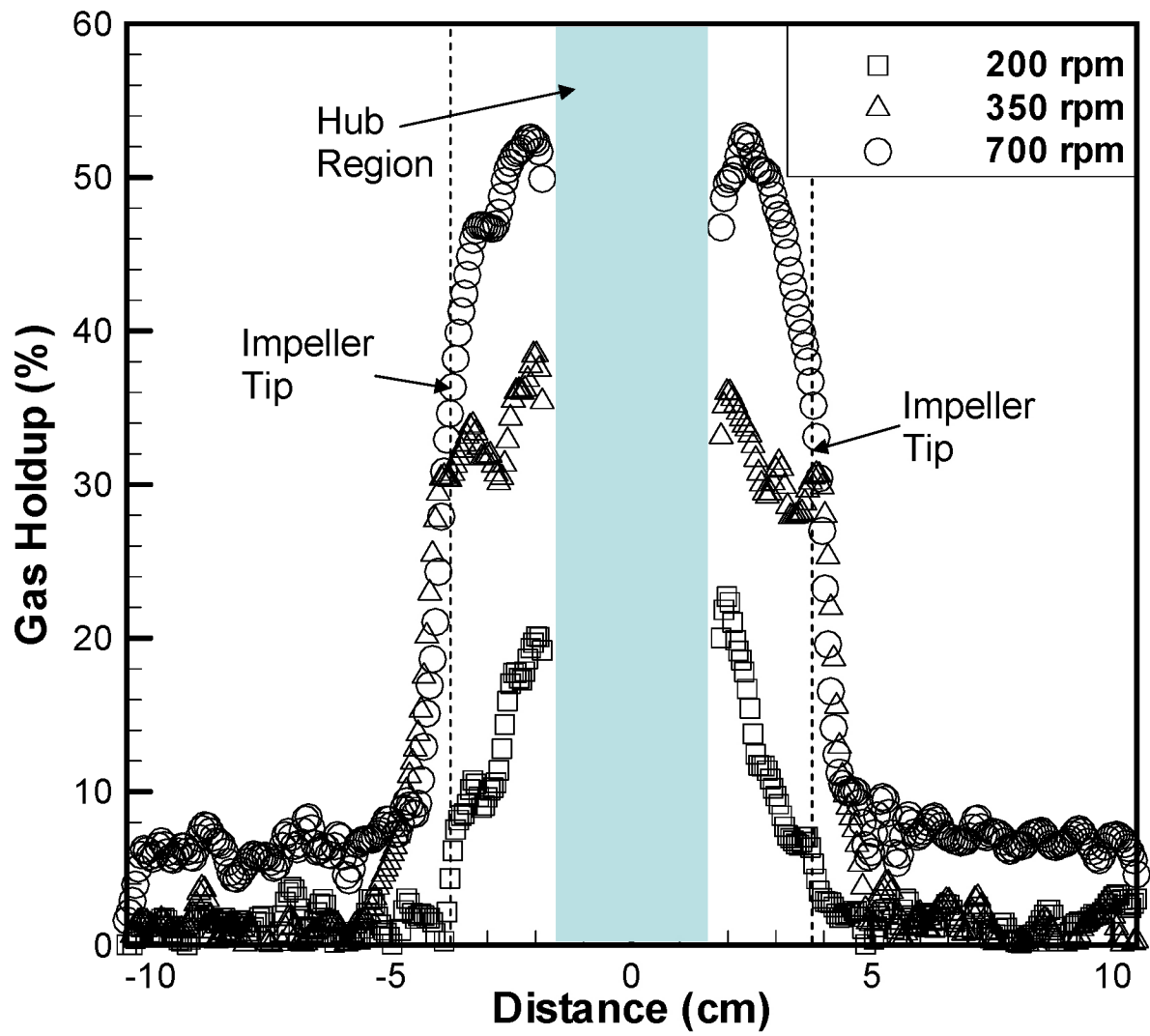


Figure 4.20: Local gas holdup values along x-slice at height  $z = 0.8$  cm for  $Q_g = 9$  LPM.

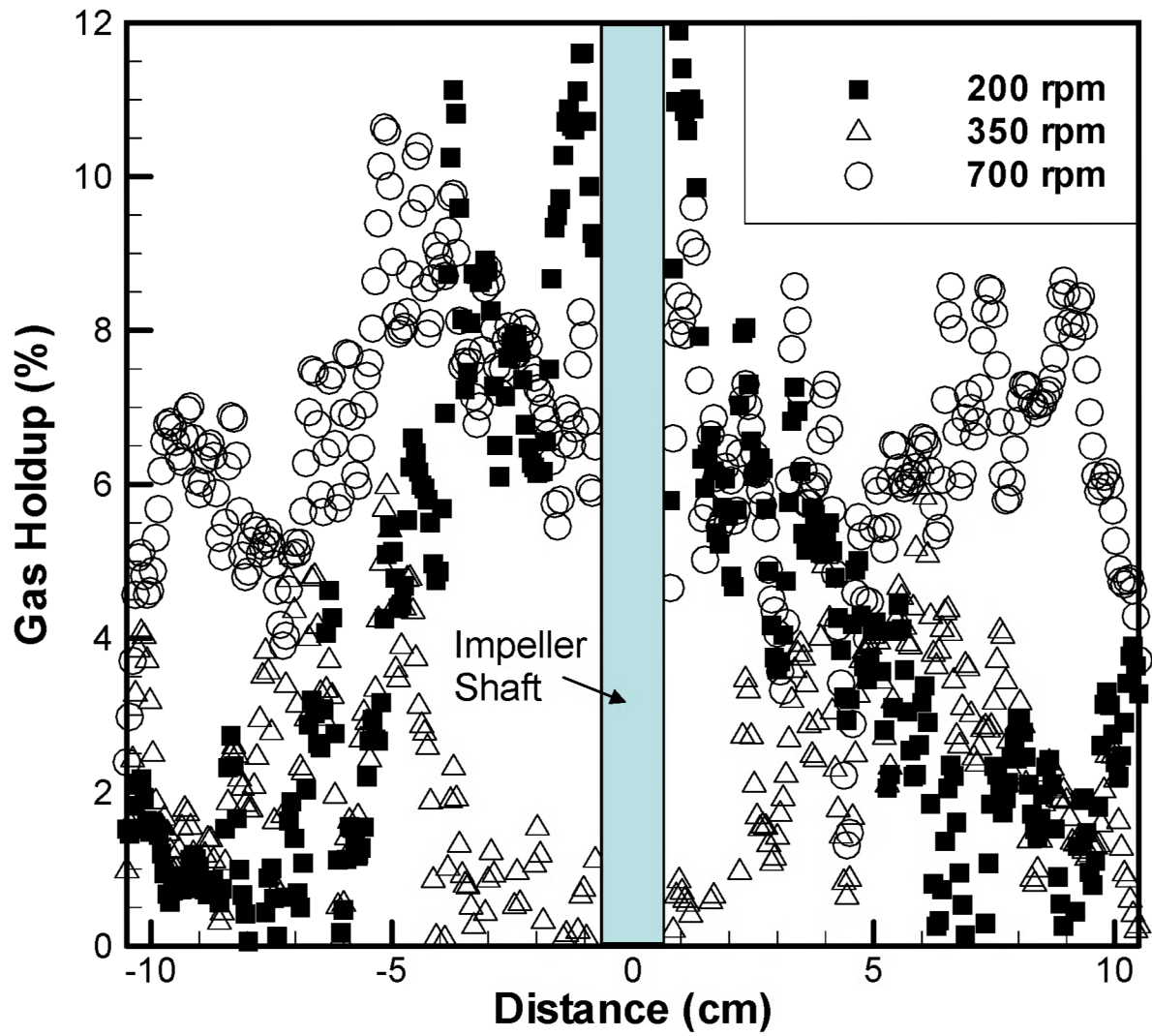


Figure 4.21: Local gas holdup values along x-slice at height  $z = 3.0$  cm for  $Q_g = 9$  LPM.

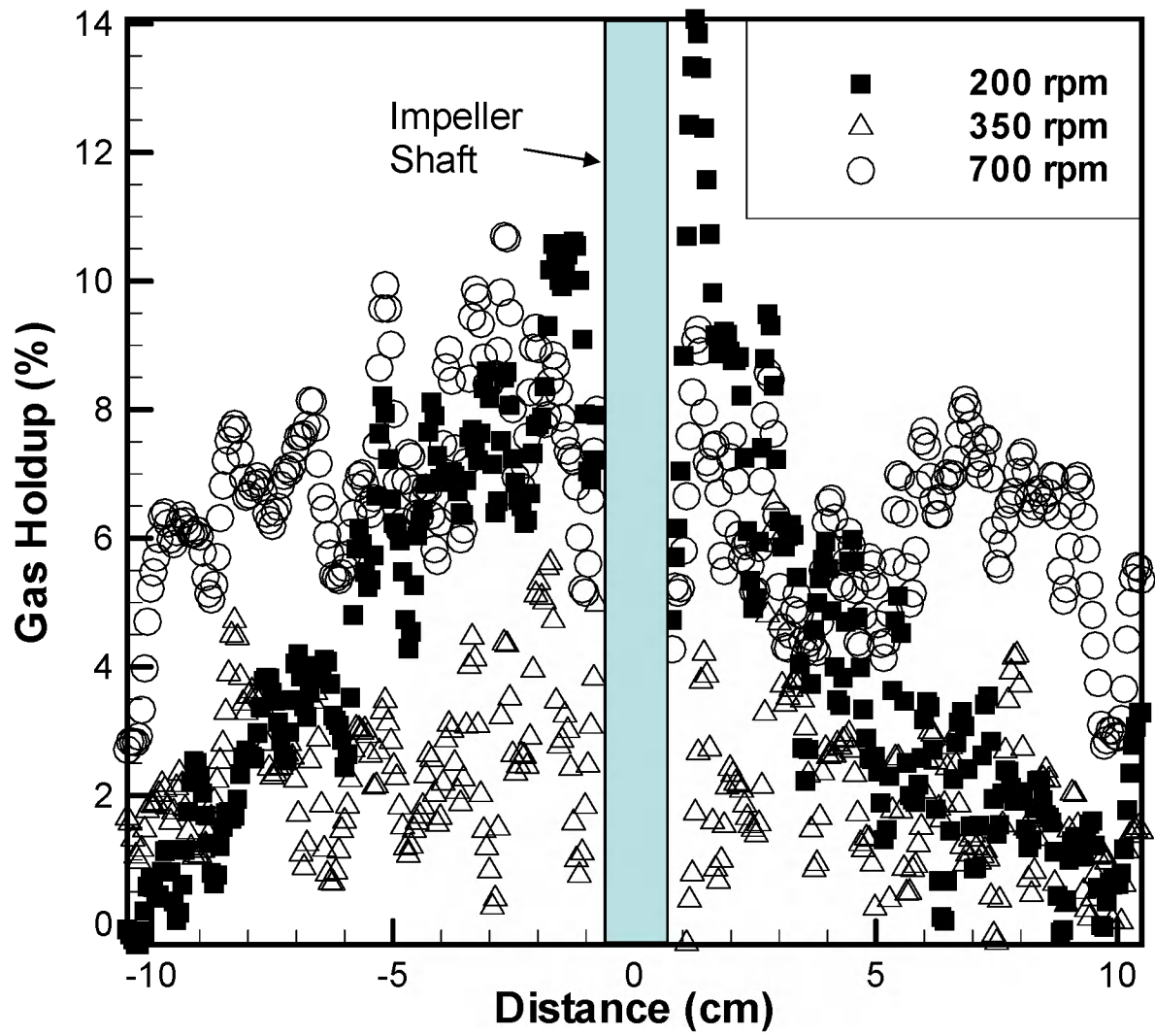


Figure 4.22: Local gas holdup values along x-slice at height  $z = 5.3$  cm for  $Q_g = 9$  LPM.

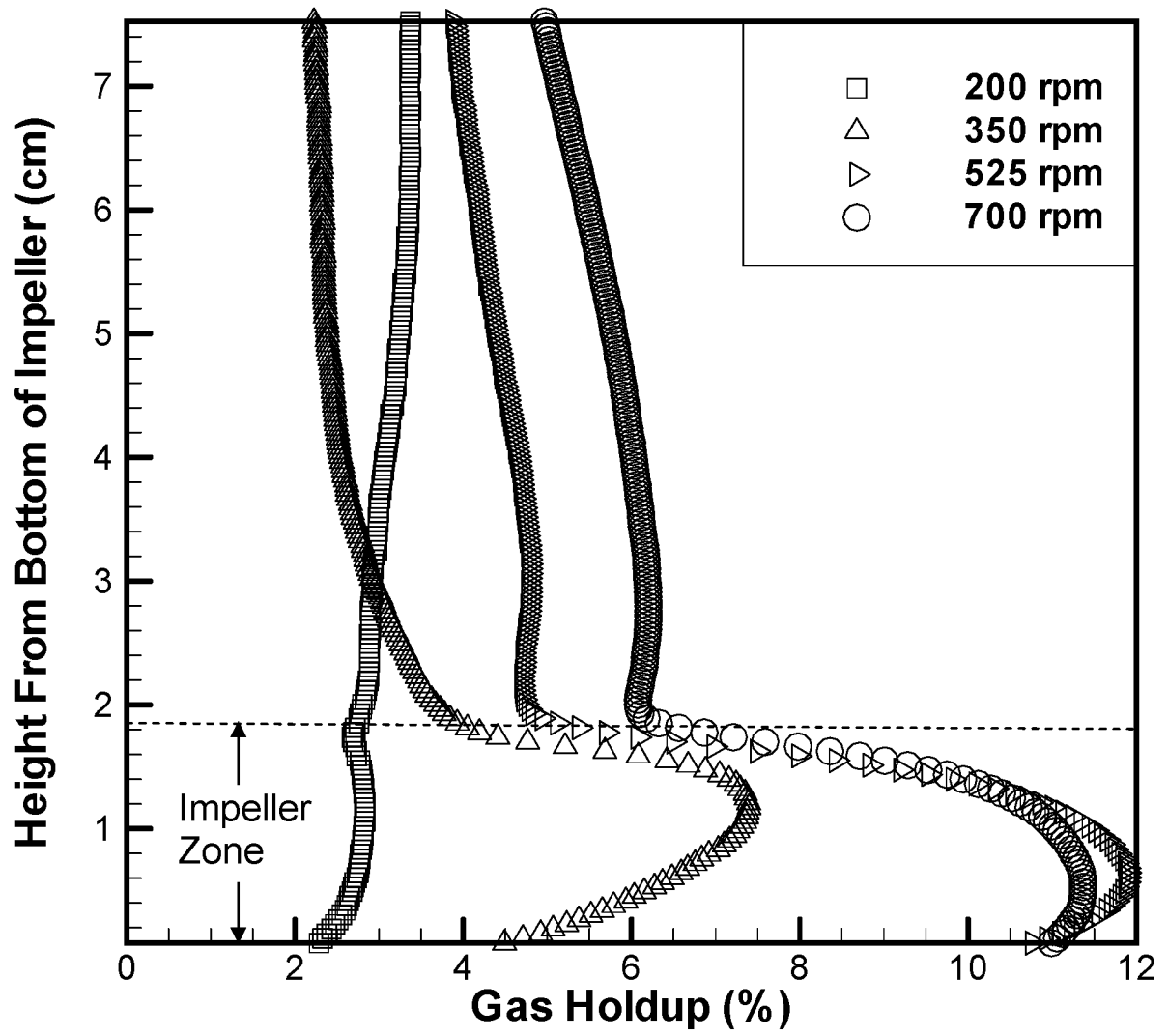


Figure 4.23: Average slice holdup for  $Q_g = 9$  LPM.

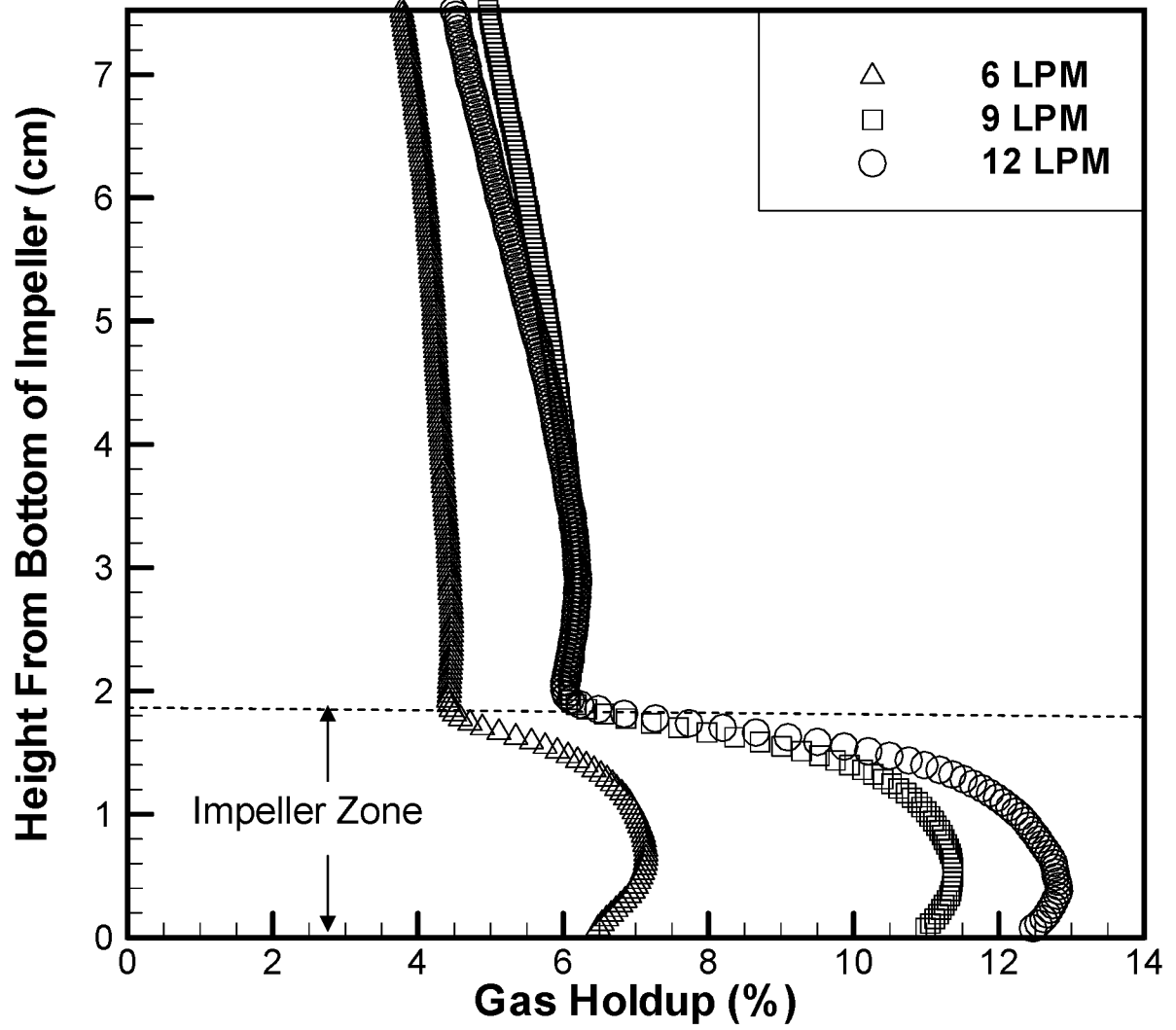


Figure 4.24: Average slice holdup for  $N = 700$  rpm.

**Table 4.1:** Conditions for CT scans.

$Q_g$ (LPM)	N (rpm)	Flow Regime	Label in Fig. 4.9
6	350	Loaded	1
6	700	Complete Dispersion	2
9	200	Flooded	3
9	350	Loaded	4
9	525	Complete Dispersion	5
9	700	Complete Dispersion	6
12	325	Loaded	7
12	700	Complete Dispersion	8

**Table 4.2:** Table for overall gas holdup of imaging region (CT) and tank (Global).

	N = 200 rpm		N = 325 rpm		N = 350 rpm		N = 525 rpm		N = 700 rpm	
	CT	Global								
6 LPM					3.4	2.9			4.8	5
9 LPM	3.0	2.9			3.5	3.3	5.9	4.5	6.9	6.0
12 LPM			5.4	4.8					7.0	6.4

## CHAPTER 5: CONCLUSIONS AND RECOMMENDATIONS

### 5.1 Conclusions

Gas holdup measurement techniques and hydrodynamics of STRs have been reviewed in this thesis. This review has shown that many people have tried to measure overall gas holdup in a STR, but very few have measured local gas holdup. To my knowledge, no local gas holdup measurements in a stirred tank reactor have been reported in the open literature using X-ray computed tomography.

In this research, local gas holdup measurements in a stirred tank reactor were obtained using X-ray computed tomography for various operating conditions. Power consumption for different operating conditions was determined to identify various STR flow regimes. The power consumption measurements were verified through digital pictures. The CT slices show that there were dramatic differences in gas dispersion depending on the operating regime. There was very little difference visually for scans taken in the same operating regime even though there were differences in impeller speed and gas flow rates. The high resolution of the X-ray system allowed minor details such as recirculation cells behind the baffles to be visualized. Local gas holdup conditions were sensitive to tank design, which was shown by the regions of higher gas holdup on one side of the x- and y-slices, and were attributed to an asymmetric ring sparger.

The gas holdup measurements were also quantitatively analyzed showing the differences between operating regimes. Flooded conditions showed a parabolic shape for local gas holdup while completely dispersed conditions had a relatively constant holdup

value. Average holdup values for the z-slice were obtained showing how the holdup changes with height. The efficient capture of gas by the impeller leads to increased holdup in the impeller region. For the flooded condition, average gas holdup increased with height while the opposite occurred for the loaded and completely dispersed conditions. From the average z-slice holdup values, an overall average holdup value for the imaging region was determined showing that the holdup increased as the impeller speed increased while holding  $Q_g$  constant.

Finally, the results in this study were verified through two different tests showing that the results were repeatable and accurate. Hence, X-ray computed tomography is an effective way to measure local gas holdup in a stirred tank reactor.

## **5.2 Recommendations for Further Study**

### **5.2.1 Software Improvements**

Future systems should incorporate a modified version of the beam hardening software which could be included in the PS\_CT software. The software would automatically apply the beam hardening correction instead of having to enter the intensity values into an excel file to determine a correction equation which is utilized in another program. Other beam hardening correction algorithms should be looked at that reduce the noise in the corrected data files.

The speed of the CT scan should be improved upon. Currently a scan with  $4 \times 4$  binning and a  $1^\circ$  degree step takes 43 minutes. At the CNDE, a similar scan takes approximately 30 minutes. The PS\_CT program should be thoroughly debugged to find why the scan is taking an extra 10-15 minutes.

### 5.2.2 Future Work

Now that a method has been developed for determining gas holdup using X-ray computed tomography, many doors have been opened for future research. Instead of using radial flow impellers, axial flow impellers could be used to see the different flow patterns created. Different regions of the tank could be imaged to produce profiles of the entire tank. The geometry of the tank could be slightly changed (baffles, sparger, tank diameter) to see how the flow patterns change. Other fluids could be used to determine how the change in viscosity of the working fluid affects gas holdup. CT scans could be taken at every 25 rpm while holding  $Q_g$  constant to determine regime transition speeds (e.g.,  $N_f$ ,  $N_{cd}$ ).

Finally, gas holdup profiles could be determined for bubble columns, airlift reactors, and fluidized beds under different operating conditions. Tracer particles could be developed that show up in high contrast with the fluid allowing for X-ray Particle Tracking Velocimetry. The X-ray system located in Black Engineering has many possibilities for further testing of multiphase flows.

## REFERENCES

- Barrett, H.H., and Swindell, W., 1981. *Radiological Imaging: The Theory of Image Formation, Detection, and Processing*. Academic Press, New York.
- Barona, N. (1979). Design CSTR reactors this way. *Hydrocarbon Processing*, 58 (7), pp 179-194.
- Bombac, A., Zun, I., Filipic, B., and Zumer, M. (1997). Gas-filled cavity structures and local void fraction distribution in an aerated stirred vessel. *AIChE Journal*, 43 (11), pp 2921-2931.
- Boyer, C., Duquenne, A.M., and Wild, G. (2002). Measuring techniques in gas-liquid and gas-liquid-solid reactors. *Chemical Engineering Science*, 57 (16), pp 3185-3215.
- Chapman, C.M., Nienow, A.W., Cooke, M., and Middleton, J.C. (1983). Particle-gas-liquid mixing in stirred vessels. Part II: Gas-liquid mixing. *Chemical Engineering Research and Design*, 61, pp 82-95.
- Chaouki, J., Larachi, F., and Dudukovic, M.P. (1997). Noninvasive tomographic and velocimetric monitoring of multiphase flows. *Industrial and Engineering Chemistry Research*, 36 (11), pp 4476-4503.
- Favre, E., Voumard, P., von Stockar, U., and Peringer, P. (1993). A capacitance probe to characterize gas bubbles in stirred tank reactors. *Chemical Engineering Journal*, 52, pp 1-7.
- Fischer, J., Broring, S., and Lubbert, A. (1992). Gas-phase properties in stirred tank bioreactors. *Chemical Engineering & Technology*, 15 (6), pp 390-394.
- Fogler, H.S. (1999). *Elements of Chemical Reaction Engineering*, Prentice Hall PTR: Upper Saddle River, New Jersey.
- Greaves, M., and Barigou, M. (1988). Estimation of gas hold-up and impeller power in a stirred vessel reactor. *Fluid Mixing III, Institute of Chemical Engineers Symposium Series*, No. 108, pp 235-255.
- Halow, J.S. (1997). Electrical capacitance imaging of fluidized beds. In *Non-Invasive Monitoring of Multiphase Flows*; Chaouki, J., Larachi, F., and Dudukovic, M.P., Elsevier: Amsterdam, The Netherlands, Chapter 9, p 263.
- Hammer, E.A., Johansen, G.A., Dyakowski, T., Roberts, E.P.L., Cullivan, J.C., Williams, R.A., Hassan, Y.A., and Claiborn, C.S. (2006). Experimental techniques. *Multiphase Flow Handbook*, 14, pp 1-125.

- Harvel, G.D., Hori, K., Kawanishi, K., and Chang, J.S. (1999). Cross-sectional void fraction distribution measurements in a vertical annulus two-phase flow by high speed X-ray computed tomography and real-time neutron radiography techniques. *Flow Measurement and Instrumentation*, 10, pp 259-266.
- Heindel, T.J., Hubers, J.L., Jensen, T.C., Gray, J.N., and Striegel, A.C. (2005). Using X-rays for multiphase flow visualization. *Proceedings of ASME Fluids Engineering Division Summer Conference*, Paper Number FEDSM2005-77359.
- Holden, P.J., Wang, M., Mann, R., Dickin, F.J., and Edwards, R.B. (1998). Imaging stirred-vessel macromixing using electrical resistance tomography. *AIChE Journal*, 44 (4), pp 780-790.
- Hsieh, J., (2003). *Computed tomography: principles, design, artifacts, and recent advances*. Bellingham, WA: SPIE Press.
- Hubers, J. (2005). An X-ray visualization facility for large-scale multiphase flows. M.S. Thesis, Iowa State University, Ames, IA.
- Hubers, J.L., Striegel, A.C., Heindel, T.J., Gray, J.N., and Jensen, T.C. (2005). X-ray computed tomography in large bubble columns. *Chemical Engineering Science*, 60 (22), pp 6124-6133.
- Kapic, A. (2005). Mass transfer measurements for syngas fermentation. M.S. Thesis, Iowa State University, Ames, IA.
- Ketcham, R., and Carlson, W. (2001). Acquisition, optimization and interpretation of X-ray computed tomographic imagery: applications to the geosciences. *Computers & Geosciences*, 27, pp 381-400.
- Khopkar, A.R., Rammohan, A.R., Ranade, V.V., and Dudukovic, M.P. (2005). Gas-liquid flow generated by a Rushton turbine in stirred vessel: CARPT/CT measurements and CFD simulations. *Chemical Engineering Science*, 60 (8-9), pp 2215-2229.
- Kumar, S.B., Dudukovic, M.P., and Toseland, B.A. (1997). Measurement techniques for local and global fluid dynamic quantities in two and three phase systems. In *Non-Invasive Monitoring of Multiphase Flows*; Chaouki, J., Larachi, F., and Dudukovic, M.P., Elsevier: Amsterdam, The Netherlands, Chapter 1, p 1.
- Lu, W.M., and Ju, S.J. (1987). Local gas holdup, mean liquid velocity, and turbulence in an aerated stirred tank using hot-film anemometry. *Chemical Engineering Journal*, 35 (1), pp 9-17.
- Nagase, Y., and Yasui, H. (1983). Fluid motion and mixing in a gas-liquid contactor with turbine agitators. *Chemical Engineering Journal*, 27 (1), pp 37-47.

Nienow, A.W., Wisdom, D.J., and Middleton, J.C. (1977). The effect of scale and geometry on flooding, recirculation, and power in gassed stirred vessels. *Second European Conference on Mixing*, Cambridge, England, pp F1 1-16.

Nienow, A.W., Warmoeskerken, M.M.C.G., Smith, J.M., and Konno, M. (1985). On the flooding/loading transition and the complete dispersal condition in aerated vessels agitated by a Rushton-turbine. *Proceedings of the Fifth European Conference on Mixing*, Wurtsburg, Germany, pp 143-154.

Nienow, A.W. (1998). Hydrodynamics of stirred bioreactors. *Applied Mechanics Reviews*, 51 (1), pp 3-32.

Ranade, V.V., and Deshpande, V.R. (1999). Gas-liquid flow in stirred reactors: trailing vortices and gas accumulation behind impeller blades. *Chemical Engineering Science*, 54 (13-14), pp 2305-2315.

Rushton, J.H., and Bimbinet, J.J. (1968), Holdup and flooding in air liquid mixing. *The Canadian Journal of Chemical Engineering*, 46, pp 16-21.

Saravanan, K., and Joshi, J.B. (1996). Fractional gas hold-up in gas inducing type of mechanically agitated contactors. *The Canadian Journal of Chemical Engineering*, 74 (1), pp 16-30.

Smith, J.M., and Warmoeskerken, M.M.C.G. (1985). The dispersion of gases in liquids with turbines. *Proceedings of the Fifth European Conference on Mixing*, Wurtsburg, Germany, pp 115-126.

Striegel, A. (2005). Development of data acquisition software for X-ray radiography, computed tomography, and stereography of multiphase flow. M.S. Thesis, Iowa State University, Ames, IA.

Supardan, M.D., Masuda, Y., Maezawa, A., and Uchida, S. (2004). Local gas holdup and mass transfer in a bubble column using an ultrasonic technique and a neural network. *Journal of Chemical Engineering of Japan*, 37 (8), pp 927-932.

Takenaka, K., and Takahashi, K. (1996). Local gas holdup and gas recirculation rate in an aerated vessel equipped with a Rushton turbine impeller. *Journal of Chemical Engineering Japan*, 29 (5), pp 799-804.

Tatterson, G. B. (1991). *Fluid Mixing and Gas Dispersion in Agitated Tanks*, McGraw-Hill: New York.

Thatte, A.R., Ghadge, R.S., Patwardhan, A.W., Joshi, J.B., and Singh, J.B. (2004). Local gas holdup measurement in sparged and aerated tanks by  $\gamma$ -ray attenuation technique. *Industrial and Engineering Chemistry Research*, 43 (17), pp 5389-5399.

Ungerman, A.J. (2006). Mass transfer enhancement for syngas fermentation. M.S. Thesis, Iowa State University, Ames, IA.

Utomo, M.B., Sakai, T., Uchida, S., and Maezawa, A. (2001). Simultaneous measurement of mean bubble diameter and local gas holdup using ultrasonic method with neural network. *Chemical Engineering & Technology*, 24 (5), pp 493-500.

Van't Riet, K. (1975). Turbine agitator hydrodynamics and dispersion performance. PhD Thesis, Delft University of Technology, The Netherlands.

Van't Riet, K., and Smith, J.M. (1975). Trailing vortex system produced by Rushton turbine agitators. *Chemical Engineering Science*, 30 (9), pp 1093-1105.

Veera, U.P., Patwardhan, A.W., and Joshi, J.B. (2001). Measurement of gas hold-up profiles in stirred tank reactors by gamma ray attenuation technique. *Institution of Chemical Engineers*, 79 (6), pp 684-688.

Wang, M., Dorward, A., Vlaev, D., and Mann, R. (2000). Measurements of gas-liquid mixing in a stirred vessel using electrical resistance tomography (ERT). *Chemical Engineering Journal*, 77 (1), pp 93-98.

Wang, W., Mao, Z.S., and Yang, C. (2006). Experimental and numerical investigation of gas holdup and flooding in an aerated stirred tank with Rushton impeller. *Industrial and Engineering Chemistry Research*, 45 (3), pp 1141-1151.

Warmoeskerken, M.M.C.G., Feijen, J., and Smith, J.M. (1981.) Hydrodynamics and power consumption in stirred gas-liquid dispersion. *Fluid Mixing, Institute of Chemical Engineers Symposium*, 64, pp J1-14.

Warmoeskerken, M.M.C.G., and Smith, J.M. (1982). Description of the power curves of turbine stirred gas-liquid dispersions. *Proceedings of the Fourth European Conference on Mixing*, Noordwijkerhout, Netherlands, pp 237-246.

Warmoeskerken, M.M.C.G., and Smith, J.M. (1985). Flooding of disc turbines in gas-liquid dispersions: a new description of the phenomenon. *Chemical Engineering Science*, 40 (11), pp 2063-2071.

Warsito, W., and Fan, L.S. (2001). Measurement of real-time flow structures in gas-liquid and gas-liquid-solid flow systems using electrical capacitance tomography (ECT). *Chemical Engineering Science*, 56 (21-22), pp 6455-6462.

Yan, W. (2000). 3D CT Visualization. Creative Component, Iowa State University, Ames, IA.

Yawalkar, A.A., Pangarkar, V.G., and Beenackers, A. (2002). Gas hold-up in stirred tank reactors. *The Canadian Journal of Chemical Engineering*, 80 (1), pp 158-166.

Yung, C.N., Wong, C.W., and Chang, C.L. (1979). Gas holdup and aerated power consumption in mechanically stirred tanks. *The Canadian Journal of Chemical Engineering*, 57 (6), pp 672-676.

Zhang, J. (2003). Development of high resolution 3D computed tomography. M.S. Thesis, Iowa State University, Ames, IA.